

**Magneto-resistive Anisotropy of Electronically Phase
Separated $\text{La}_{0.7-x}\text{Pr}_x\text{Ca}_{0.3}\text{MnO}_3$ Manganite Thin Films**

by

Hüseyin Serhat Alagöz

A thesis submitted in partial fulfillment of the requirements for the degree of

Doctor of Philosophy

Department of Physics

University of Alberta

© Hüseyin Serhat Alagöz, 2014

Abstract

This thesis studies the anisotropic magneto-resistance (AMR) in electronically phase separated $\text{La}_{0.7-x}\text{Pr}_x\text{Ca}_{0.3}\text{MnO}_3$ (LPCMO) epitaxial thin films. Different Pr doping levels, epitaxial strain, magnetic fields, temperature and two dimensional confinement effects have been used to understand this fundamental spintronics property in such strongly correlated manganite systems. We investigated four major problems associated with the AMR in phase separated manganites, including: carrier localization, crossover phenomena, metastability and spatial confinement effects.

First, we studied the correlations between the small polaron activation energy and the anisotropic magneto-resistance (AMR) of $\text{La}_{0.7-x}\text{Pr}_x\text{Ca}_{0.3}\text{MnO}_3$ with ($0.00 \leq x \leq 0.35$) epitaxial films grown on the SrTiO_3 and LaAlO_3 substrates. The analysis of the small polaron activation energy in the paramagnetic insulating state revealed that an increasing activation energy can be correlated with the gradual exponential-like increase of AMR, independent of the thickness of the film, the substrate and the doping concentration x .

We continued to investigate the AMR characteristics at low temperatures. LPCMO films subjected to only compressive epitaxial strain have shown a

sign change at certain temperatures, called cross-over temperature whose value have been found to be directly related to the doping driven epitaxial strain. Strain-driven easy axis magnetization elongation has been used to explain the AMR sign difference between compressive and tensile strained LPCMO films.

We investigated the AMR in LPCMO thin films deposited on various substrates near the metal-insulator transition temperature, where the electronic phase separation is dynamic (metastable), such that ferromagnetic metallic (FMM) and charge ordered insulating (COI) regions evolve in shape and size with changing temperature. It was found that the non-monotonic angular dependence of the resistance is recovered during repetitive sweeping of θ (the angle between the magnetic field and the current) between 0° and 180° .

Finally, we studied the AMR for LPCMO micro-bridges fabricated on STO and LAO substrates. When the width of the films approaches the size of the intrinsic metallic and insulating domains, AMR deviates from its typical small and oscillatory behavior into sharp-rectangular and very high values. The mechanism of this unusual change in the AMR is discussed.

The experimental results obtained for the AMR of phase separated LPCMO films provide new information about the nature and dynamics of the AMR in strongly correlated manganite systems, and may lead to new investigations of the resistive-switching phenomena in magnetic storage devices and spintronics.

Preface

The research presented in this dissertation was carried out in the Department of Physics at the University of Alberta under the supervision of Professor Jan Alexander Jung, from September 2009 to March 2014. Unless otherwise stated, the original work presented in this thesis is based on my own work.

Chapter 4 of this thesis has been published as **H. S. Alagoz**, M. Khan, M. M. Saber, S. T. Mahmud, K. H. Chow, and J. Jung, “*Influence of A-site doping and strain on the relationship between the anisotropic magnetoresistance and charge localization in films of $La_{0.3}Pr_{0.4}Ca_{0.3}MnO_3$ manganites,*” Appl. Phys. Lett. 102, 242406. I conceived the experiments and responsible for the data collection and analysis as well as the manuscript composition. M. Khan, M. M. Saber and S. T. Mahmud were involved in preparing thin film samples. K. H. Chow and J. Jung supervised the research project and discussed the results.

Chapter 6 of this thesis has been published as **H. S. Alagoz**, J. Jeon, S. T. Mahmud, M. M. Saber, B. Prasad, M. Egilmez, K. H. Chow, and J. Jung, “*Recovery of oscillatory magneto-resistance in phase separated $La_{0.3}Pr_{0.4}Ca_{0.3}MnO_3$ epitaxial thin films,*” Appl. Phys. Lett. 103, 232402. I designed the experi-

ments, grew the samples and analyzed the data. J. Jeon participated in conducting the transport measurements. S. T. Mahmud, M. M. Saber involved in sample preparations. Both B. Prasad and M. Egilmez conducted X-Ray measurements. K. H. Chow and J. Jung were the supervisory authors and involved in manuscript composition.

Appendix sections (A1-A4) of this thesis have been published as **H. S. Alagoz**, I. Zivkovic, S. T. Mahmud, M. M. Saber, G. Perrin, J. Shandro, Mahmud Khan, Y. Zhang, M. Egilmez, J. Jung, and K. H. Chow, “*Competing A-site and B-site doping effects on magneto-transport of $RE_{0.55}Sr_{0.45}MnO_3$ manganites in the vicinity of SGI and FMM border*,” Phys. Stat. Sol. B. 250, 2158-2162. I was responsible for the sample preparation, data collection and analysis and contributed to the manuscript composition. I. Zivkovic participated in magnetic measurements of samples. S. T. Mahmud, M. M. Saber, G. Perrin, J. Shandro, Mahmud Khan and Y. Zhang were involved in sample preparations. M. Egilmez contributed interpreting the experimental results. J. Jung and K. H. Chow supervised the project and were involved with the concept formation and manuscript composition.

The manuscripts containing original material in chapter 5, chapter 7 and appendix sections (A5-A9) of this thesis were prepared for submission to Applied Physics Letter.

To my parents...

Acknowledgments

First and foremost, I would like to thank my supervisor Prof. Jan Alexander Jung for giving me the opportunity to work with such a great group. His valuable guidance, insightful suggestions on my manuscripts as well as the patience throughout my PhD studies were indispensable. I am also indebted to my other supervisor, Prof. Kim H. Chow for his scientific discussions and constant encouragement, which were of great value.

I would like to also thank my thesis committee members for their time, interest and insightful assessments for my dissertation. I am grateful to my colleagues: Dr. Mehmet Egilmez, Dr. Mohamed Elsayed, Shaikh Tawhid Mahmud, Jaechun Jeon and Mary Alvean Narreto with whom I enjoyed many discussions and fruitful suggestions.

Special thanks go to the great technicians: Mr. Don Mullin, Mr. Greg Popowich, Mr. Tony Paget, Mr. Tony Walford and Mr. Dave Fortin. None of this would have been possible without their great help and support. Away from the lab, I would like to express my thanks to Ms. Sarah Derr for helping me with all administrative issues. Finally, I would like to thank my loving and supporting wife Leslie Anne Weigl, my family, and Zirca, the flying cute bird.

Abbreviations

1. AMR: Anisotropic magnetoresistance
2. CMR: Colossal magnetoresistance
3. EPS: Electronic phase separation
4. FMM: Ferromagnetic metallic
5. COI: Charge ordered insulating
6. DE: Double-exchange
7. SO: Spin-orbit
8. JT: Jahn-Teller

Contents

1	Introduction	1
1.1	Motivation	1
1.2	Organization of the thesis	7
1.3	List of Publications	9
2	Theory	11
2.1	Introduction	11
2.2	Manganite Physics	12
2.2.1	The perovskite structure	12
2.2.2	Crystal field theory and Jahn-Teller distortions	15
2.2.3	Double-exchange mechanism	20
2.3	Electronic Phase Separation Phenomena	24
2.3.1	Multi-phase coexistence	24
2.3.2	An interesting example: $\text{La}_{1-x}\text{Pr}_x\text{Ca}_{0.3}\text{MnO}_3$	25
2.3.3	Electron transport in manganites of reduced dimensions	27
2.4	Theory of anisotropic magneto-resistance (AMR)	32

3	Experimental Aspects	43
3.1	Introduction	43
3.1.1	Polycrystalline (Bulk) LPCMO samples	44
3.1.2	Thin film growth and device fabrication	44
3.2	Sample characterization	50
3.2.1	Structural characterization	50
3.2.2	Magneto-transport measurements	52
4	Correlation between charge localization and anisotropic magneto-resistance in $\text{La}_{1-x}\text{Pr}_x\text{Ca}_{0.3}\text{MnO}_3$ films	60
4.1	Introduction	60
4.2	Experimental details	63
4.3	Results and discussion	64
4.4	Conclusions	73
5	Crossover of anisotropic magneto-resistance in phase separated $\text{La}_{1-x}\text{Pr}_x\text{Ca}_{0.3}\text{MnO}_3$ thin films	75
5.1	Introduction	75
5.2	Experimental details	77
5.3	Results and discussion	80
5.4	Conclusions	90
6	Recovery of oscillatory magneto-resistance in $\text{La}_{0.3}\text{Pr}_{0.4}\text{Ca}_{0.3}\text{MnO}_3$ epitaxial thin films	91
6.1	Introduction	91

6.2	Experimental details	93
6.3	Results and discussion	95
6.4	Conclusion	104
7	Anisotropic magneto-resistance in spatially-confined phase separated manganite structures	105
7.1	Introduction	105
7.2	Anisotropic magneto-resistance of spatially confined LPCMO/SrTiO ₃ epitaxial films	108
7.2.1	Experimental details	108
7.2.2	Results and discussion	111
7.2.3	Conclusions	123
7.3	Anisotropic magneto-resistance of spatially confined LPCMO/LaAlO ₃ epitaxial films	124
7.3.1	Introduction	124
7.3.2	Experimental procedure	125
7.3.3	Experimental Results	127
7.3.4	Discussion	134
7.3.5	Conclusions	135
8	Summary and Conclusions	137
8.1	Overview	137
8.2	Relationship between the charge localization and anisotropic magneto-resistance in La _{1-x} Pr _x Ca _{0.3} MnO ₃ manganites	139
8.3	Crossover of anisotropic magneto-resistance in phase separated La _{1-x} Pr _x Ca _{0.3} MnO ₃ thin films	140

8.4	Recovery of oscillatory magneto-resistance in $\text{La}_{0.3}\text{Pr}_{0.4}\text{Ca}_{0.3}\text{MnO}_3$ epitaxial thin films	141
8.5	Anisotropic magneto-resistance in spatially-confined phase separated manganite structures	141
8.6	Future Research	143

Appendices

A	Competing doping effects in manganites	161
A.1	Introduction	161
A.2	Experimental details	163
A.3	Experimental results and discussion	165
A.4	Conclusions	175
A.5	Unusual double-peak magneto-resistance in ruthenium doped ferromagnetic oxides	176
A.6	Introduction	176
A.7	Experimental details	178
A.8	Experimental results and discussion	179
A.9	Conclusions	185

List of Figures

1.1	<p>(a) The dependence of AMR on the activation energy (E_a) and metal to insulator transition temperature, T_{MI} for compressively strained $\text{Nd}_{0.55-x}\text{Sm}_x\text{Sr}_{0.45}\text{MnO}_3/\text{LAO}$ thin films. (b) The dependence of AMR on temperature for $\text{La}_{0.65}\text{Ca}_{0.35}\text{MnO}_3$ (LCMO)/LAO films showing crossover (in red circle) in the sign. (c) AMR exhibits exponential-like behavior as a function of θ at 6 T for $\text{Pr}_{0.7}\text{Ca}_{0.3}\text{MnO}_3$ (PCMO)/SLGO thin film. Figures (a)-(c) are reproduced from the references of [7], [6] and [9], respectively.</p>	3
1.2	<p>(a)-(d) Evolution of domain structure during the temperature drop from 41.9 K to 36.7 K in electronically phase separated manganite films. The pictures (a)-(d) are taken from [10] (e) Schematic picture of spatially confined EPS systems. LPCMO wire (rectangular box) is comparable to the FMM and COI domain size. (taken from [11])</p>	6

2.1	Ideal cubic perovskite structure with AMnO_3 (A=Rare earth ions). The anions (oxygens) are at the vertices of the octahedron. Mn cation sits in the center of the cube and rare earth ions at the corners of the cube.	13
2.2	Temperature dependent resistivity for LaMnO_3 (LMO) (a) and $\text{La}_{0.7}\text{Ca}_{0.3}\text{MnO}_3$ (LCMO) (b) manganite films, showing insulating and metal-to-insulator transition, respectively.	14
2.3	(a) d -orbital splitting by the crystal field in ABO_3 with perovskite structure in cubic (undistorted) and tetragonal (distorted) configurations. (figure taken from Tokura (1999)[18]) (b) Schematic representation of atomic orbitals.	18
2.4	Double exchange process: Two electrons are simultaneously transferred, one from a bridging O^{2-} anion to the Mn^{4+} center and other from a Mn^{3+} center to the O^{2-} anion. Note that spins of t_{2g} electrons for Mn^{3+} and Mn^{4+} are ferromagnetically coupled. (Figure is reproduced from [25])	21
2.5	Representation of the hopping exchange integral in double exchange mechanism.	23

2.6 (a) Mixed-phase state near the percolation threshold where arrows indicate the conduction either through the metallic or the insulating regions, depending on temperature. (b) Two-resistance model for Mn-oxides. The schematic plot of the effective resistance R_{eff} vs. temperature for the parallel connection of metallic (percolative) $R^{per.M}$ and insulating R_I resistances. (c) Effective resistivity ρ_{dc} vs. temperature produced for 100 x 100 random resistor network cluster. The $p=1$ (fully metallic) and 0 (fully insulating) are the limits taken from Ref.[27]. Figures adapted from Ref.[33]. 26

2.7 (a) Temperature dependence of the MFM image sequence for cooling. (b) The temperature dependence of the resistivity of the $\text{La}_{0.33}\text{Pr}_{0.34}\text{Ca}_{0.33}\text{MnO}_3$ manganite thin film over a thermal cycle. The blue curve corresponds to cooling and the red curve to the warming. (c) Temperature dependence of the MFM image sequence during warming cycle. Figure is reproduced from Ref.[32] 28

2.8 (a) Resistivity versus temperature for the LPCMO wires under magnetic field of 3.75 T. Arrows indicate the warming or cooling cycles. The 1.6 μm wire whose size is comparable to those of the FMM and COI domains, exhibits giant ultra-sharp peak in the temperature dependence of resistivity. (b) When the magnetic field increases from 3.75 T to 14 T, the jumps are reduced. Figure is adapted from Ref.[11] 30

2.9	Transition time from a metal to insulator or insulator to a metal of a single electronic domain on each of the three background states in $10\ \mu\text{m} \times 50\ \mu\text{m} \times 70\ \text{nm}$ LPCMO wire. The lifetimes are averages of those of thousands of individual transitions on each of the three background resistive states. In each case, it takes more time for the domain to transition from the disordered FMM phase to the ordered COI phase. Figure is adapted from Ref.[37]	31
2.10	Resistance of the ferromagnet depends on the angle, θ between the current, \mathbf{J} direction and the magnetization, \mathbf{M}	35
2.11	Density plot of the argument of the integral defined in equation 2.31 for H, M in the x direction, and $k_z = \pi/2$. Figure is adapted from Ref.[46]	40
2.12	Numerical results for the normalized conductivity. Solid line shows the $\cos(2\beta)$ dependence behavior of the conductivity. Figure is adapted from Ref.[46]	42
3.1	Physics of magnetron sputtering. Neutral Argon atoms are ionized when a strong potential difference (DC) is applied between the anode and cathode. The ions are then accelerated to a target. After the collisions with the surface of target, atoms are released (sputtered) and travel to the substrate and form layers of atoms in the thin film.	46

3.2	Magnetron sputtering systems. The picture on the right taken during LPCMO epitaxial thin film deposition.	47
3.3	(a) Step by step photo-lithography process for manganite film based device fabrication. (b) A picture taken during inspecting the 50 micro- meter wide $\text{La}_{0.3}\text{Pr}_{0.4}\text{Ca}_{0.3}\text{MnO}_3$ bridge patterned on (001) oriented LaAlO_3 single crystal substrate.	49
3.4	(a) Room-temperature X-ray diffraction (XRD) pattern for polycrystalline $\text{La}_{0.35}\text{Pr}_{0.35}\text{Ca}_{0.3}\text{MnO}_3$ (LPCMO) obtained using Rietveld refinement. (b) and (c) 45 nm thick LPCMO (Pr=0.35) films deposited on LaAlO_3 and SrTiO_3 single crystal substrates.	51
3.5	Diagram of AMR measurement circuitry.	53
3.6	A view of the magneto-transport measurement set-up. Left inset shows the electrical connections to thin film sample. . . .	54
3.7	Schematic representation of the out-of plane and the in-plane anisotropic magnetoresistance measurements of a thin film sample. The angle, θ between the magnetic field \mathbf{H} and transport current \mathbf{I} is indicated in the figures.	59
4.1	(a) Typical temperature dependence of resistivity of selected LCMO/STO ($x = 0$) films, and (b) the corresponding temperature dependence of the AMR.	65

4.2	(a) Dependence of the activation energy E_a on the concentration x of Pr in $\text{La}_{0.7-x}\text{Pr}_x\text{Ca}_{0.3}\text{MnO}_3$ ($0.00 \leq x \leq 0.35$) films (44 nm thick) deposited on LAO and STO substrates. (b) and (c) Thickness dependence of E_a for LCMO ($x = 0$) and LPCMO ($x = 0.35$) films deposited on LAO and STO substrates.	66
4.3	(a) Dependence of the AMR_{max} (AMR at the maximum) on the concentration x of Pr in $\text{La}_{0.7-x}\text{Pr}_x\text{Ca}_{0.3}\text{MnO}_3$ ($0.00 \leq x \leq 0.35$) films (44 nm thick) deposited on LAO and STO substrates. (b) and (c) Thickness dependence of the AMR_{max} for LCMO ($x = 0$) and LPCMO ($x = 0.35$) films deposited on LAO and STO substrates. (d) and (e) Dependence of the AMR_{max} on strain ϵ_z for all films studied.	68
4.4	(a) Dependence of the AMR_{max} on the activation energy E_a for 44 nm thick films of LPCMO (where the concentration of Pr x varies between 0 and 0.35) deposited on STO and LAO substrates. These data are compared with those obtained for 300 nm thick films NSSMO deposited on LAO substrates. For the NSSMO films the data are plotted versus x , the concentration of Sm on the A-site. (b) and (c) Dependence of the AMR_{max} on E_a for all LPCMO films studied. The data were obtained for LCMO ($x = 0$) and LPCMO ($x = 0.35$) films of thickness t between 10 and 300 nm, and for 44 nm thick films of LPCMO (of compositions $x = 0 - 0.35$).	71

5.1	Normalized resistivity, $\rho(T)/\rho_{max}$ at a zero field, plotted for selected $\text{La}_{0.7-x}\text{Pr}_x\text{Ca}_{0.3}\text{MnO}_3$ films for $0 \leq x \leq 0.40$ deposited on (a) STO and (b) LAO substrates, respectively. The data shown were taken during warming. (c) The maximum resistivity (ρ_{max}) and corresponding metal-insulator transition temperatures, T_{MI} as a function of doping concentration, x	78
5.2	Temperature dependence of the out-of-plane magnetoresistive anisotropy, AMR measured in a field of 1.1 T at doping levels between $x=0$, and $x=0.40$ for films grown on (a) SrTiO_3 and (b) LaAlO_3 substrates. Dashed curves in both figures show the expected dependence of the AMR_{max} on doping. The change of sign of the AMR with an increasing doping is shown in the rectangular yellow area. Insets in (a) and (b) show the direction of magnetic field \mathbf{H} and the direction of the current \mathbf{J} , and the expanded view of the AMR at low temperatures for LPCMO/LAO doped films, respectively. (c) The normalized angular dependent resistivity measured at 155 K (i.e., where the AMR has a peak) and at 100 K (i.e., yellow region). The solid lines are the fits to the data (see text). (d) The crossover temperature, T^* at which the AMR sign changes from positive to negative is shown for $x=0.40$ doped film.	81
5.3	The dependence of the crossover temperature, T^* and c -axis epitaxial strain ε_z on doping concentration x for LPCMO/LAO thin films.	83

5.4	The influence of temperature and doping x on the AMR sign evolution for tensile LPCMO/STO (a - b), and compressive strained LPCMO/LAO films (c -d) collected at temperatures between 10 K - 200 K for ($0.0 \leq x \leq 0.40$).	84
5.5	(a) The dependence of AMR on doping concentration x at 50 K for LPCMO/STO and LPCMO/LAO films. The Jahn-Teller distortion of MnO_6 octahedron under tensile and compressive strain are shown in (b) and (c) respectively. The black arrows show the stress axis and the blue arrow shows the corresponding direction of the easy-axis magnetization.	87
5.6	The dependence of magnetization on temperature measured in a magnetic field of 1.1 T applied parallel and perpendicular to the (100) crystallographic direction of the LPCMO ($x=0.40$) films on (a) LAO and (b) STO substrates, respectively.	89
6.1	(a) Temperature dependence of resistivity of LPCMO film deposited on NGO, STO and LAO substrates in a zero magnetic field; (b) Schematic showing the direction of magnetic field \mathbf{H} and direction of the current \mathbf{J} both located in the plane of the film.	96

6.2	[(a), (c) and (e)]	Dependence of the normalized resistivity on magnetic field measured at selected temperatures between 100 and 170 K. Magnetic field is parallel to J ($\theta = 0$). The hysteresis loop is the largest at 125 K, 140 K and 155 K for the film deposited on NGO, STO and LAO substrates, respectively. The arrows inside the loop in (a) indicate the sweeping directions of the applied magnetic field. [(b), (d) and (f)] Dependence of the normalized resistivity on the angle θ between \mathbf{H} and \mathbf{J} at a field of 1.1 T, measured at temperatures between 100 K and 170 K for films deposited on NGO, STO and LAO substrates.	97
6.3	[(a), (b) and (c)]	The angular repetitive sweeps of the resistivity at 125 K, 140 K and 155 K in a field of 1.1 T for films grown on NGO, STO and LAO respectively. The inset shows the expanded view of $\rho(\theta)$. Arrows indicate an increase/decrease of θ	99
6.4	[(a), (b) and (c)]	Dependence of the resistivity on time for the magnetic field of 1.1 T, parallel to J ($\theta = 0$) at a temperature of 125 K, 140 K and 155 K for LPCMO films grown on NGO, STO and LAO substrates, respectively. The measurement of ρ for times larger than 100 min was performed during the angular repetitive sweeps of θ between 0° and 180°	101

6.5	Dependence of the normalized resistivity, ρ and $\rho(\theta)$ on time for the magnetic field of 1.1 T, recorded during cooling and warming cycles at a temperature of 125 K for LPCMO/NGO film. The inset shows the normalized $\rho(\theta)$ obtained during the first angular sweep of the magnetic field. It corresponds to the time period marked by the shaded rectangular region in the main figure.	103
7.1	The device geometry showing LPCMO films fabricated on the STO single crystal substrates. $1 \mu\text{A}$ current \mathbf{I} is applied in the x direction. Magnetic field \mathbf{H} is applied in the xy plane of the film. Upper inset shows the image of the $2 \mu\text{m}$ wide bridge. . .	109
7.2	(a) R - T curve for the $2 \mu\text{m}$ bridge, which shows several discrete jumps in the vicinity of the T_{MIT} , as a consequence of the reduction of conducting channels down to a single pathway.[11] (b) The R - T curve for the $25 \mu\text{m}$ wide bridge showing no discrete steps. (c), $2 \mu\text{m}$ bridge shows large and sharp (see the inset) in-plane AMR at the same temperature range where these step-like features are observed. (d) AMR for wider, $25 \mu\text{m}$ bridge is negligible.	112

7.3	<p>(a) Angular dependence of resistance $R(\theta)$ for the $2\ \mu\text{m}$ wire reveals dramatic rectangular-like feature at the AMR peak temperature of 118.5 K. The inset shows the expanded view of the normalized $R(\theta)$ at 118.5 K compared with those at 100 K and 150 K. (b) $R(\theta)$ for the $25\ \mu\text{m}$ bridge shows regular oscillatory behavior at all selected temperatures (see the inset). (c) and (d) The histogram of the resistance collected at 118.5 K for the $2\ \mu\text{m}$ and $25\ \mu\text{m}$ bridges during the measurement of $R(\theta)$ in the plane of the films. The angle θ between the H and I directions is 0° for H perpendicular to I, and 90° for H parallel to I. . .</p>	114
7.4	<p>Temperature evolution of the angular dependence of resistance around the AMR peak for the $2\text{-}\mu\text{m}$ wide bridge shows ultra-sharp resistance jumps of a various height and width. The difference between the switching angles, indicated as white dots increases with an increase of temperature from 118.5 K to 120 K with a 0.5 K steps.</p>	116

7.5	<p>The dependence of the resistance on time in a field of 1.1 T perpendicular to current direction ($\theta=0^\circ$) at 118.5 K for the 2-μm wide bridge. The measurements of the resistance for waiting times larger than (a), (t=1000 s) (b), (t=2000 s) and (c), (t=3000 s) (i.e., after dashed lines) were performed during the angular repetitive sweeps of θ between 0° and 180° (see the inset of Fig. 7.4 (b)) The amplitude of the resistive switching was only slightly affected after various decay-time measurements (shown in the inset of Fig. 7.4 (a)). Black arrows in (b) show the direction of the current I.</p>	119
7.6	<p>(a) Schematic of the switching phenomena for intrinsic FMM-COI-FMM domains in 2 μm bridge. Magnetization of FMM-1 domain rotates freely with the rotation of applied magnetic field. (b) Switching results in a completely anti-parallel or parallel state whereas intermediate states represent the small change of the resistance on the angle (represented by the orange colored double sided arrows).</p>	122

- 7.7 (a) The device geometry of LPCMO film fabricated on the (001) oriented LaAlO_3 substrates. A constant $1 \mu\text{A}$ current \mathbf{I} , flows in the x direction while the magnetic field \mathbf{H} is applied in the xy plane of the film. (b) The scanning electron micrograph (SEM) of the $5 \mu\text{m} \times 5 \mu\text{m}$ bridge (δ indicates the width of the bridge). (c)-(e) Resistance versus temperature for the $50 \mu\text{m}$, $25 \mu\text{m}$ and $5 \mu\text{m}$ wide $\text{La}_{0.3}\text{Pr}_{0.4}\text{Ca}_{0.3}\text{MnO}_3$ bridges in a zero-field and a magnetic field of 1.1 T, measured during cooling cycle. The inset in (e) shows the expanded view of sharp jumps detected on the $R(T)$ curve of the $5 \mu\text{m}$ -bridge. 126
- 7.8 The dependence of the resistance on the angle θ between the transport current \mathbf{I} and magnetic field \mathbf{H} for $5 \mu\text{m}$ wide LPCMO bridge. $R(\theta)$ was collected at 85 K (a), 90 K (b) and 140 K (c). Note that $\theta = 0^\circ$ for \mathbf{H} perpendicular to \mathbf{I} , and 90° for \mathbf{H} parallel to \mathbf{I} . The width, W of the rectangle in $R(\theta)$ is indicated by a double-sided arrow. (d) and (e) show the dependence of the resistance on time obtained during the in-plane rotation of the magnetic field at 85 K and 90 K. Each cycle of measurements was obtained after the same warming and cooling procedures (see text). The blue and violet dots in (d) and (e) indicate the maximum resistance obtained for $\mathbf{H} \perp \mathbf{I}$ and $\mathbf{H} \parallel \mathbf{I}$, respectively. (f) W as a function of temperature. The sign of the AMR suddenly changes at 89 K. 128

7.9	Dependence of the normalized resistance ($R/R(\theta=0^\circ)$) on the applied magnetic fields between 0.2 T and 1.1 T measured at (a) 85 K and (b) 90 K temperatures for the 5 μm -wide LPCMO/LAO bridge.	131
7.10	Dependence of the anisotropic magneto-resistance (AMR) on temperature in 1.1 T, recorded during cooling cycle for the 5 μm -wide LPCMO bridge. The inset shows temperature dependence of the AMR obtained for the 25 μm and 50 μm -wide LPCMO bridges.	132
7.11	Dependence of the anisotropic magneto-resistance (AMR) on temperature in 1.1 T, recorded during cooling cycle for the 5 μm -wide LPCMO bridge. The inset shows temperature dependence of the AMR obtained during warming cycle for the same LPCMO bridge.	133
8.1	Studying AMR under various spatially confined structures and excitations: (a) geometry effects (i.e., zig-zag and anti-dots), (b) lattice-strain control under biasing PMNT-film and (c) photo-excitations of a micro-bridge.	144
A.1	Home built alternating current (AC) susceptibility system with a sample attached to a sapphire rod.	164

A.2	Temperature dependence of resistivity (ρ) and normalized ac susceptibility (χ') of $x = 0\%$, 10% and 25% Ru doped $y = 0.00$, 0.75 and 1.00 compositions.	166
A.3	Magnetic phase diagram of $\text{RE}_{0.55}\text{Sr}_{0.45}\text{Mn}_{1-x}\text{Ru}_x\text{O}_3$ with $\text{RE} = \text{Gd}_y\text{Sm}_{1-y}$ ($0 \leq y \leq 1$) and Ru doping level x between 0 and 25% . Red and blue areas are used as visual aids for identifying ferromagnetic metallic (FMM) and ferromagnetic insulating (FMI) regimes, respectively. Green dashed areas indicate the presence of spin glass insulators (SGI).	169
A.4	Dependence of x_{po} and x_{pl} , the Ru doping level at which the percolation onset and loss occur, on $\langle r_A \rangle$. Inset: An example of the dependence of T_{MIT} on x in $\text{Gd}_{0.55}\text{Sr}_{0.45}\text{Mn}_{1-x}\text{Ru}_x\text{O}_3$ ($y = 1$) system ($\langle r_A \rangle = 1.1984 \text{ \AA}$), showing both the percolation onset and loss. SGI, FMM and FMI mark spin-glass insulator, ferromagnetic metal, and ferromagnetic insulator, respectively.	171
A.5	(a) Temperature dependence of resistivity $\rho(T)$ in Ru doped $\text{Eu}_{0.55}\text{Sr}_{0.45}\text{Mn}_{1-x}\text{Ru}_x\text{O}_3$ (ESMRO) obtained during warming in zero magnetic field for doping ranges (a) ($0 \leq x \leq 0.10$) and (b) ($0.12 \leq x \leq 0.25$). The arrows indicate a decreasing trend of residual resistivity at (ρ_{10K}) with an increasing Ru doping level.	180

- A.6 (a) Typical temperature dependence of resistivity for low ($x=0.005$) and high ($x=0.25$) Ru doping levels in ESMO manganites. Dashed rectangle indicates the anomaly in the resistance. (b) Signature of a spin-disorder temperature (T_{SD}) extracted by plotting $d\ln(\rho)/dT^{-1}$ vs temperature. (c) Magneto-resistance as a function of temperature for $x=0.005$ and 0.25 . The solid lines are guides to the eye. 181
- A.7 Figures; (a) to (c) show magnetic phase diagrams of Ru doped $RE_{0.55}Sr_{0.45}Mn_{1-x}Ru_xO_3$ with $RE = Sm, Eu$ and Gd plotted as a function of Ru doping level x between 0 and 25%. Red and light blue areas mark ferromagnetic metallic (FMM) and ferromagnetic insulating (FMI) regimes, respectively. Green dashed areas mark spin glass insulating (SGI) regimes. Figures; (d) to (f) shows corresponding magneto-resistance values obtained at low temperatures (black points) and high temperatures (blue points) plotted as a function of Ru doping. 182
- A.8 Schematic of spin disorder effect near the Curie temperature for highly Ru doped manganite samples. Ru inclusion create spatially spin disordered regions (shown by red area) in the domain. Some randomly oriented spins in this domain tend to align with the application of magnetic field increasing the volume fraction of ferromagnetic metallic (FMM) region. This results in an increase of magneto-resistance in the sample. . . 184

CHAPTER 1

Introduction

1.1 Motivation

Anisotropic magneto-resistance (AMR), a response of the resistivity to the angular rotation of an applied magnetic field (or magnetization) with respect to the electric current, is one of the spintronics functionality of ferromagnetic materials and alloys that has been implemented in early microelectronic devices, such as magneto-resistive random access memories.[1, 2]

The microscopic origin of AMR in these materials is based on quantum mechanical principles and a consequence of spin-orbit scattering of the spin-polarized charge carriers, resulting in an anisotropic angular dependence of the current density \mathbf{J} with respect to the magnetization direction \mathbf{M} . [3, 4] However, compared to the exchange interaction, spin-orbit coupling is relatively weak, which renders AMR a small effect, reaching a few percent in certain Ni-based

alloys. [5] From the point of technological interest, the relatively small effect in the AMR magnitude is certainly a disadvantage.

In a sharp contrast to ferromagnetic metals and alloys, however, in strongly correlated ferromagnetic oxides such as the colossal magneto-resistive (CMR) rare-earth perovskite manganites $\text{RE}_{1-x}\text{AE}_x\text{MnO}_3$ (where RE and AE are the rare earth and alkaline elements, respectively), the AMR could reach much higher values (i.e., close to 100 %)[6] making these materials very promising for possible device applications. Also, other properties such as the temperature dependence of the AMR is different from that observed in ferromagnetic metals, showing a large maximum near the metal to insulator transition (T_{MI}).

Unfortunately, the microscopic mechanism of the AMR is still under debate. The underlying mechanism is difficult to study since CMR materials are electronically phase separated. Contrary to ferromagnetic alloys, the electronic properties, including the AMR in CMR materials, are governed by a dynamic system of micro/nanosopic ferromagnetic metallic (FMM) domains and charge-ordered insulating (COI) ones, which is sensitive to small changes in the temperature and magnetic field near the T_{MI} .

Studies done over the last decades have shown that every studies of the AMR conducted in phase separated manganites raised new challenging questions. These questions need to be addressed in order to understand the complexity of this effect in such strongly correlated systems. Below, I highlight the unanswered problems associated with the AMR effect in manganites. These problems are being addressed in this thesis.

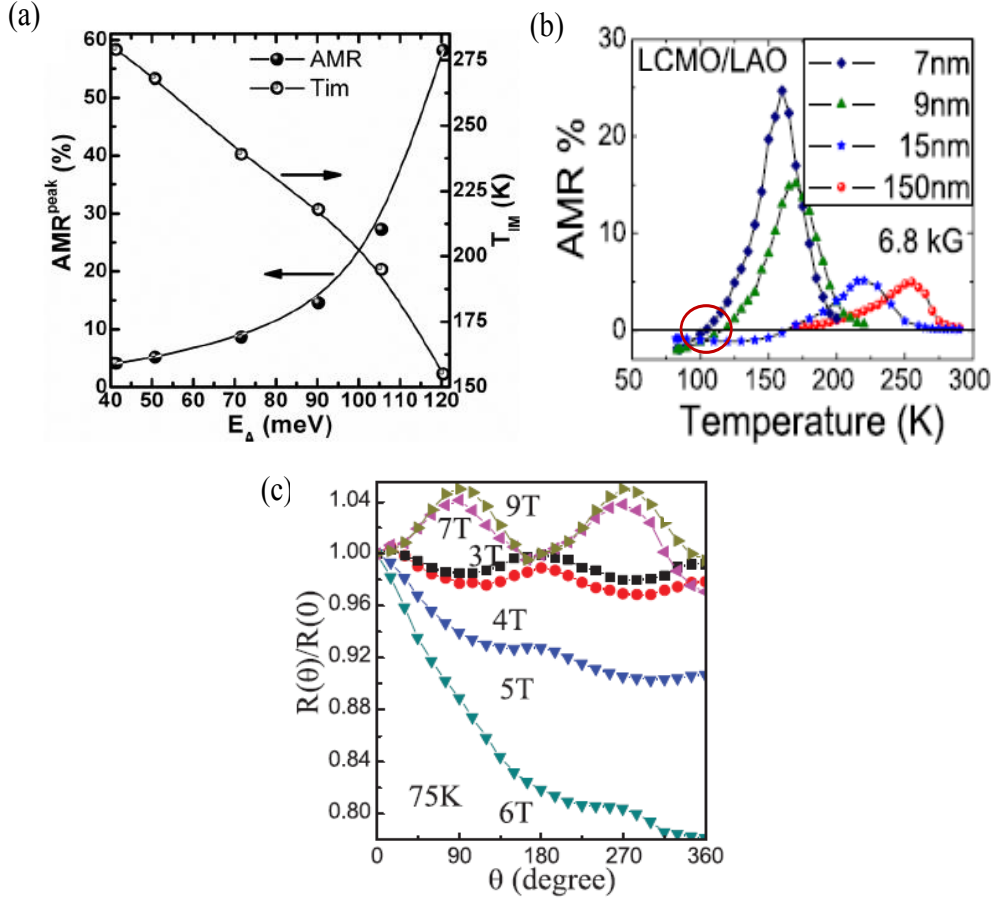


Figure 1.1: (a) The dependence of AMR on the activation energy (E_a) and metal to insulator transition temperature, T_{MI} for compressively strained $\text{Nd}_{0.55-x}\text{Sm}_x\text{Sr}_{0.45}\text{MnO}_3/\text{LAO}$ thin films. (b) The dependence of AMR on temperature for $\text{La}_{0.65}\text{Ca}_{0.35}\text{MnO}_3$ (LCMO)/LAO films showing crossover (in red circle) in the sign. (c) AMR exhibits exponential-like behavior as a function of θ at 6 T for $\text{Pr}_{0.7}\text{Ca}_{0.3}\text{MnO}_3$ (PCMO)/SLGO thin film. Figures (a)-(c) are reproduced from the references of [7], [6] and [9], respectively.

Carrier localization & AMR

Recent studies have shown that the AMR depends strictly on the local lattice distortions. Distortions are enlarged when the average ionic radius of the A-site cations decreases. For example, in $\text{Nd}_{0.55-x}\text{Sm}_x\text{Sr}_{0.45}\text{MnO}_3$ ($x=0.00-0.45$) compressively strained thin films, substituting smaller Sm^{+3} for Nd^{+3} cations produces stronger carrier localization. This is evidenced by the increase of the activation energy (E_a) of small polaron hopping in the paramagnetic insulating phase with an increasing x .^[7] The data (see Fig. 1 (a)) obtained for these films show a gradual exponential increase of the AMR with an increasing E_a . However, it is unclear whether this dependence is universal (i.e., still applies for other manganite systems) and how it depends on the sign of epitaxial strain (tensile and compressive). My goal was to address these issues. They are very crucial from the point of applications, since the knowledge of the value of E_a might be used to predict the maximum values of the AMR in manganite films.

Crossover phenomena in AMR

Another issue which requires better understanding is the crossover phenomena in the AMR. In general, dependence of the resistance on the angle, θ between the magnetic field and current shows $\sin^2\theta$ behavior over a wide range of temperatures in manganite thin films. Interestingly, some manganite thin films, subjected to compressive epitaxial strain, such as $\text{La}_{0.65}\text{Ca}_{0.35}\text{MnO}_3/\text{LAO}$ (see Fig. 1 (b)), crossover from $\sin^2\theta$ to $\cos^2\theta$ is observed as the temperature is lowered well below the metal - insulator transition temperature.^[6] Unfortunately, the crossover in the temperature dependence of the AMR has not been fully

understood. In fact, only compressive epitaxial strain causes this unexpected behavior. These observations raise several questions: How is this crossover affected by lattice distortions? Is there any correlation between the crossover temperature and the magnitude of the lattice strain? What is the effect of the crossover on the maximum AMR? My goal was to answer these fundamental questions.

Phase coexistence, size confinement & AMR (near T_{MI})

As previously emphasized, strong correlations are believed to affect the spin-orbit coupling and the magnitude of the AMR in electronically phase separated (EPS) manganites. In the temperature region where the competition between the electronic phases is the strongest, some thin films of manganites, such as $\text{La}_{0.67}\text{Ca}_{0.33}\text{MnO}_3$ [8] and $\text{Pr}_{0.7}\text{Ca}_{0.3}\text{MnO}_3$ [9](see Fig. 1 (c)) do not show standard oscillatory magneto-resistance. In these films the resistance decreases monotonically and exponential-like with an increasing angle between the directions of applied magnetic field and current. The origin of this unusual angular dependence remains unclear. In order to better understand the mechanism behind this unusual change, comprehensive study including the role of the dynamics of phase separation and thermal hysteresis effects on the AMR should be investigated.

Recent experiments have shown that fluctuations between the competing FMM and COI electronic phases are the dominant phenomenon that governs the first-order electronic phase transitions in manganites. The average size of these domains depends on the composition, temperature and magnetic field

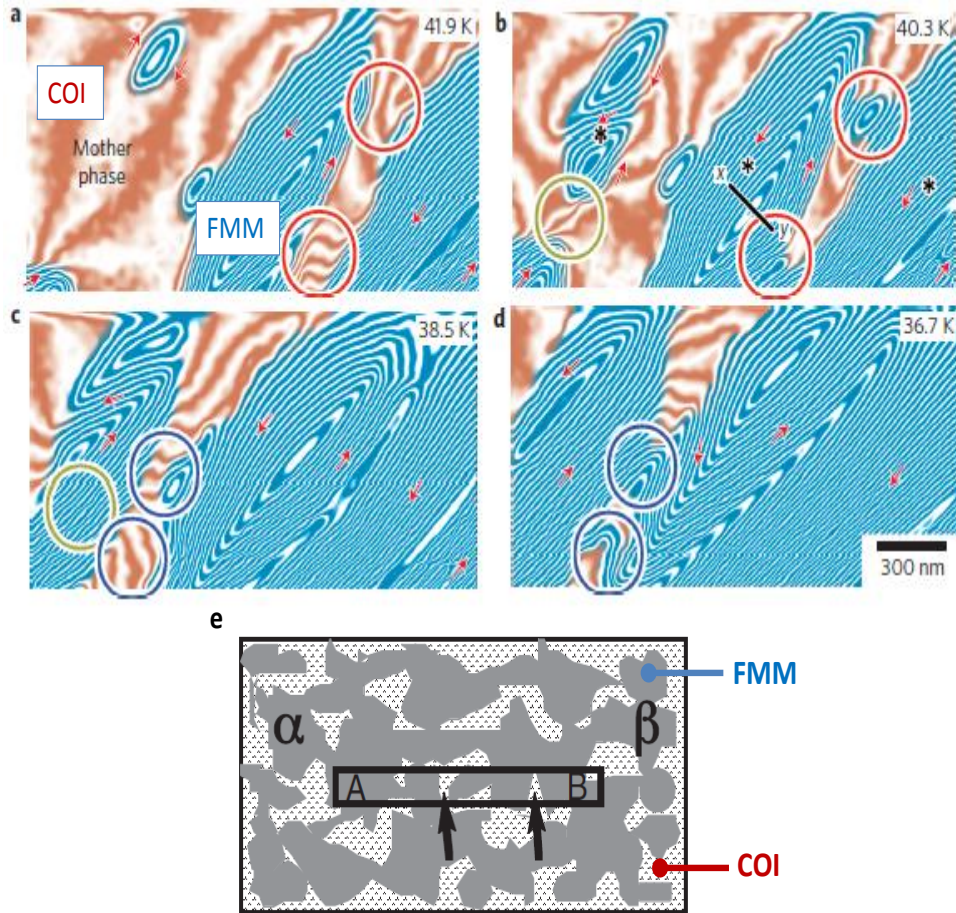


Figure 1.2: (a)-(d) Evolution of domain structure during the temperature drop from 41.9 K to 36.7 K in electronically phase separated manganite films. The pictures (a)-(d) are taken from.[10] (e) Schematic picture of spatially confined EPS systems. LPCMO wire (rectangular box) is comparable to the FMM and COI domain size. (taken from [11])

(see Fig. 2 (a)), and ranges from nanometers in most manganites to micrometers in $\text{La}_{0.25}\text{Pr}_{0.375}\text{Ca}_{0.375}\text{MnO}_3$ systems.[10] A small number of individual domains could be physically trapped by constricting them into micro-bridges,[11] at certain temperatures below the metal - insulator transition temperature. Using this configuration, a number of questions about the nature of the AMR at the FMM/COI domain level could be addressed. If the spatial dimension is reduced towards the length scale of the electronic phase separation, how do the competing electronic phases behave, and how does the AMR respond to this situation?

I attempted to address the aforementioned questions by measuring the temperature, field, and time dependence of resistance of a well-known electronically phase separated $\text{La}_{0.7-x}\text{Pr}_x\text{Ca}_{0.3}\text{MnO}_3$ LPCMO ($0.00 \leq x \leq 0.40$) manganite thin films. These films were subjected to epitaxial strain of various magnitude anisotropy and sign (compressive/tensile).

1.2 Organization of the thesis

I have investigated the magneto-transport properties of epitaxial manganite thin films. Brief descriptions of each chapter are given below:

Chapter 1 Motivation: summarizes some challenging questions associated with AMR effect and briefly mentions the goals of the dissertation.

Chapter 2 Theoretical background: consists of two parts; (*i*) the physics of perovskite manganites including the phase co-existence phenomena and elec-

tric transport under reduced dimensions. (ii) theory of anisotropic magneto-resistance in ferromagnetic metals and strongly correlated electronic systems.

In *Chapter 3*, the experimental techniques are reviewed. Section 3.1.1 gives details of the preparation of bulk (polycrystalline) LPCMO samples. In section 3.1.2, thin film deposition and device fabrication methods (photo-lithography techniques) are explained in detail. In section 3.2, sample characterization methods are described, such as electrical transport and structural characterization of bulk and thin film LPCMO samples.

In *Chapter 4*, the correlation between the charge localization and the AMR of LPCMO epitaxial films grown on STO and LAO substrates has been studied. Results have been obtained by measuring and analyzing temperature dependent resistance in the paramagnetic insulating state using Emin-Holstein's adiabatic small polaron hopping model.

In *Chapter 5*, the results obtained for the anisotropic magneto-resistance and its temperature dependence as a function of Pr doping for 45 nm thick LPCMO epitaxial films deposited on (001) oriented STO and LAO substrates are presented. The role of doping induced strain on the crossover temperature and their possible relation to the maximum anisotropic magneto-resistance have been analyzed and discussed.

Chapter 6 The in-plane AMR of LPCMO films deposited on (100) oriented NGO, and (001) oriented STO and LAO substrates is presented. The mechanism of the formation of nonmonotonic dependence of the resistance on the angle, θ between the magnetic field and the transport current at temperatures

where the electronic phase separation is the strongest. A method that recovers the regular, oscillatory behavior in the $R(\theta)$ for electronically phase separated manganites is introduced and discussed in detail.

In *Chapter 7*, spatial confinement effect on the AMR properties of LPCMO films grown on STO and LAO substrates is studied. Possible mechanisms associated with the AMR in confined geometries are discussed.

Chapter 8 summarizes the main results of the dissertation and discuss the future work.

In the *Appendix* section, the magneto-transport phase diagrams of the ruthenium (Ru) doped polycrystalline manganites are presented.

1.3 List of Publications

1. **H. S. Alagoz**, J. Jeon, S. T. Mahmud, M. M. Saber, B. Prasad, M. Egilmez, K. H. Chow, and J. Jung, *Recovery of oscillatory magneto-resistance in phase separated $La_{0.3}Pr_{0.4}Ca_{0.3}MnO_3$ epitaxial thin films*. Appl. Phys. Lett. **103**, 232402 (2013).
2. **H. S. Alagoz**, M. Khan, M. M. Saber, S. T. Mahmud, K. H. Chow, and J. Jung, *Influence of A-site doping and strain on the relationship between the anisotropic magnetoresistance and charge localization in films of $La_{0.3}Pr_{0.4}Ca_{0.3}MnO_3$ manganites*. Appl. Phys. Lett. **102**, 242406 (2013).
3. **H. S. Alagoz**, I. Zivkovic, S. T. Mahmud, M. M. Saber, G. Perrin, J. Shandro, Mahmud Khan, Y. Zhang, M. Egilmez, J. Jung, and K. H. Chow, *Compet-*

ing A-site and B-site doping effects on magneto-transport of $RE_{0.55}Sr_{0.45}MnO_3$ manganites in the vicinity of SGI and FMM border. *Phys. Stat. Sol. B.* **250**, 2158-2162 (2013).

4. J. Jeon, **H. S. Alagoz**, R. Boos, J. Jung, and K. H. Chow, *Reentrant low-field magneto-resistance in $La_{0.3}Pr_{0.4}Ca_{0.3}MnO_3$ film due to spatial confinement.* *Appl. Phys. Lett.* **104**, 122405 (2014).

5. M. A. B. Narreto, **H. S. Alagoz**, J. Jeon, K. H. Chow, and J. Jung, *Dynamic distortions & polaronic effects in $La_{0.8}Ba_{0.2}Mn_{1-x}Al_xO_3$ manganites.* *J. Appl. Phys.* **115**, 223905 (2014).

6. J. Jeon, **H. S. Alagoz**, J. Jung, and K. H. Chow, *Surface inhomogeneities and the electronic phase separated states in thin films of $La_{0.35}Pr_{0.35}Ca_{0.30}MnO_3$* *J. Appl. Phys.* **115**, 233907 (2014).

7. S. T. Mahmud, M. M. Saber, **H. S. Alagoz**, J. Jung, and K. H. Chow, *Current density and intrinsic electroresistance of the $Sm_{1-x}Sr_xMnO_3$ manganite.* *J. Phys. Chem. Solids* **74**, 1865-1867 (2013).

8. S. T. Mahmud, M. M. Saber, **H. S. Alagoz**, K. Biggart, R. Bouveyron, Mahmud Khan, J. Jung, and K. H. Chow, *Disorder enhanced intrinsic electroresistance in $Sm_{0.60}Sr_{0.40}Mn_{1-x}Fe_xO_3$.* *Appl. Phys. Lett.* **100**, 2320406 (2012).

9. S. T. Mahmud, M. M. Saber, **H. S. Alagoz**, K. Biggart, R. Bouveyron, Mahmud Khan, J. Jung, and K. H. Chow, *Intrinsic electroresistance of $Sm_{0.60}Sr_{0.40}MnO_3$ and $Sm_{0.55}Sr_{0.45}MnO_3$.* *Appl. Phys. Lett.* **100**, 072404 (2012).

CHAPTER 2

Theory

2.1 Introduction

In manganites, complex interplay between the spin, charge, and orbital degrees of freedom is believed to be responsible for a number of striking effects such as metal to insulator transition (T_{MI}) and colossal magneto-resistance (CMR).[12] These interactions are extremely sensitive to the structural distortions of MnO_6 octahedra which can be modified via chemical doping, epitaxial strain, magnetic field and temperature.[13] In order to better understand these physical properties, the fundamentals of manganite physics are introduced including some concepts such as the crystal and electronic structure of transition metal-oxides, exchange interactions. The multi-phase coexistence phenomena in LPCMO manganites are also introduced and the physics of magneto-transport under reduced dimensional systems is discussed. Finally, the theory of AMR in ferromagnetic metals and manganites is presented.

2.2 Manganite Physics

2.2.1 The perovskite structure

Rare-earth manganites crystallize in the cubic perovskite structure with the $RE\text{MnO}_3$ general formula, where RE represents the rare-earth ions such as La, Pr, Nd, Sm, Eu, Gd, ...etc.[14] Figure 2.1 shows the $RE\text{MnO}_3$ perovskite crystal structure where the rare-earth ions sit at the corner sites of the cube and Mn ion occupies the center of the cubic structure. The oxygen ions surround the Mn ions are located at the vertices of a octahedron. In an ideal perovskite structure, the bond lengths between the rare-earth, O and Mn ions have the ratio $\langle RE-O \rangle / \langle Mn-O \rangle = \sqrt{2}$. According to the ionic model where the bond lengths are defined by the ionic radii;[15] a deviation from the ideal cubic perovskite structure (tolerance factor) which compares the Mn-O separation with the separation of oxygen atom and RE-site occupant;

$$\textit{tolerance factor} : t = \frac{r(RE) + r(O)}{\sqrt{2}[r(Mn) + r(O)]} \quad (2.1)$$

where the $r(\text{Mn})$, $r(\text{RE})$ and $r(\text{O})$ are the average ionic radii of Mn, RE and the oxygen ions, respectively. Distorted perovskite structures such as the orthorhombic and rhombohedral type structures occurs when tolerance factor deviates from $t=1$.

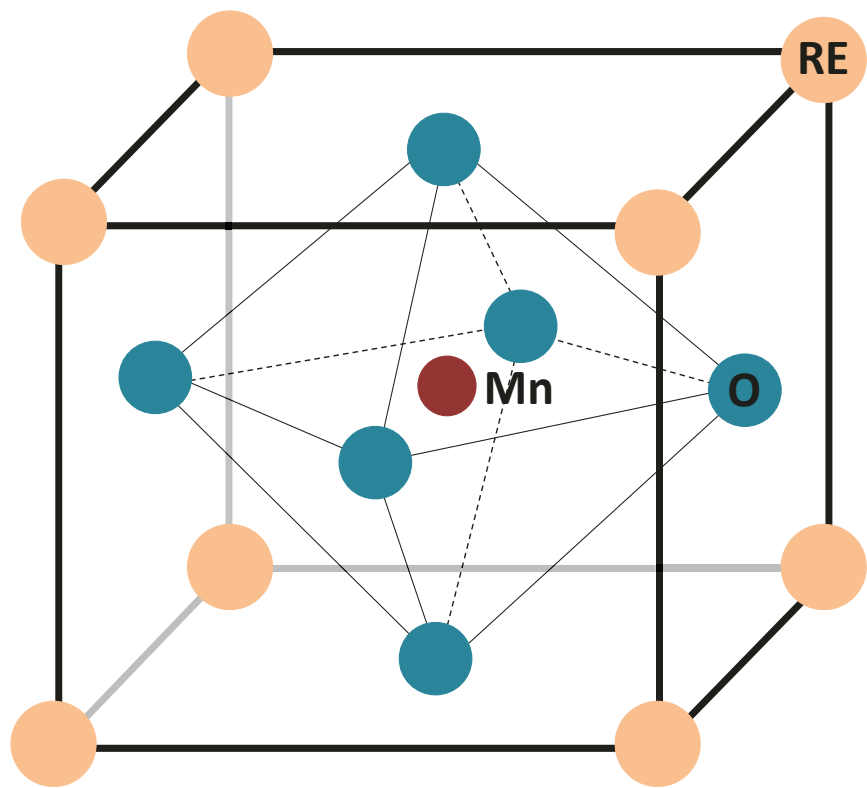


Figure 2.1: Ideal cubic perovskite structure with $AMnO_3$ (A=Rare earth ions). The anions (oxygens) are at the vertices of the octahedron. Mn cation sits in the center of the cube and rare earth ions at the corners of the cube.

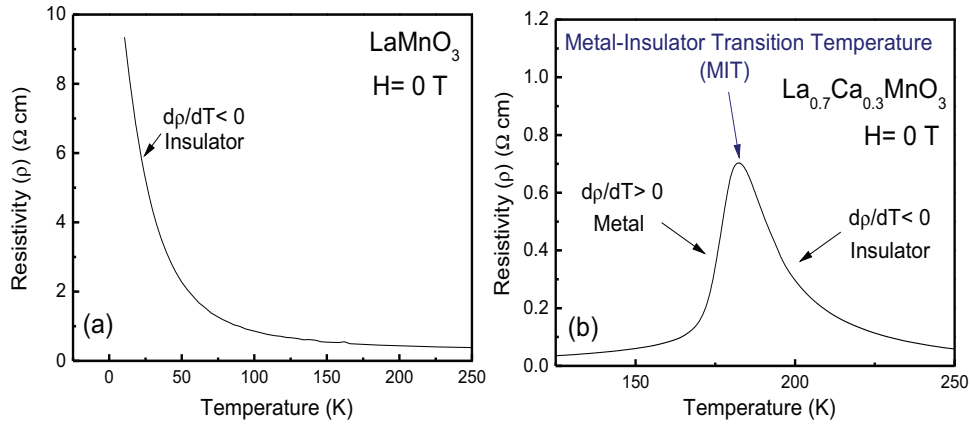


Figure 2.2: Temperature dependent resistivity for LaMnO_3 (LMO) (a) and $\text{La}_{0.7}\text{Ca}_{0.3}\text{MnO}_3$ (LCMO) (b) manganite films, showing insulating and metal-to-insulator transition, respectively.

Depending on the radius of the RE site ion and the valence state of Mn ion, magnetic and transport properties in manganites show different properties.[16, 17, 18] For instance, the ground state of LaMnO_3 (with La^{+3} , Mn^{+3} and O^{-2}) compound is an anti-ferromagnetic insulator (AFI). On the other hand, when trivalent La^{+3} ions are partially replaced by divalent Ca^{+2} ion (eg., $\text{La}_{0.7}\text{Ca}_{0.3}\text{MnO}_3$), the ground state of the manganite becomes ferromagnetic metallic (FMM) (see Fig. 2.2) Inclusion of Ca not only reduces the average ionic radius of the rare-earth site but also generates equivalent amount of Mn^{+4} ions in the compound. This means that magneto-transport properties of manganites are strongly affected when a mixed-valency (Mn^{+3} and Mn^{+4}) is produced in the compound. Questions are: how are the magnetic interactions affected when compound contains Mn ions with different valency? What is

the relation between the magnetism and the conductivity in these systems? Below, we describe the electronic structure of the Mn ion and its impact on the conductivity and magnetism when it experiences a crystal field, in the lattice with different degree of distortions (i.e., undistorted (ideal) cubic, and distorted tetragonal).

2.2.2 Crystal field theory and Jahn-Teller distortions

A free manganese (Mn) ion with $[\text{Ar}] 3d^5 4s^2$ electronic configuration has five d -states which are degenerate in the energy. However, in a crystal such degeneracy is lifted by electric field generated by the surrounding oxygen ions, crystal field. In following, we show how the atomic orbitals are rearranged with different energy and wave-functions under crystal field. Ligand oxygens are approximated by negative point charges, which affect the electrostatic potential of the central d electrons. In Figure 2.1, one sees six ligands in the center of the six faces of a cube. The total electrostatic potential can be expressed as;[\[19\]](#)

$$\begin{aligned}
 V(r) &= \sum_{i=1}^6 \frac{Ze^2}{4\pi\epsilon_0|\mathbf{r} - \mathbf{R}_i|} \\
 &= \frac{1}{4\pi\epsilon_0} \left\{ \frac{6Ze^2}{a} + \frac{7Ze^2}{2a^5} r^4 \sqrt{\frac{4\pi}{9}} \right. \\
 &\quad \left. (Y_{40}(\theta, \phi) + \sqrt{\frac{5}{14}}(Y_{44} + Y_{4-4})) + \dots \right\}
 \end{aligned} \tag{2.2}$$

where the \mathbf{R}_i is the position vector of the ligand point charge. Ze is the ligand

valence and r , θ , and ϕ are the polar coordinates of the central d electron. Y_{lm} represents the spherical harmonics. In the presence of this ligand field, five degenerate $3d$ orbitals, ϕ_{332} , ϕ_{321} , ϕ_{320} , $\phi_{33\bar{1}}$ and $\phi_{32\bar{2}}$ split into two groups (doubly degenerate E_{eg} and triply degenerate E_{t2g} orbitals). The one-electron wavefunctions of atoms or ions are expressed as the product of the radial wave function R_{nl} , angular wave function Θ_{lm} and the spherical harmonics Y_{lm}

$$\phi_{32m} = R_{32}(r) \Theta_{2m}(\theta) \Phi_m(\phi) \quad (2.3)$$

$$\Theta_{20}(\theta) = \frac{\sqrt{5}}{2\sqrt{2}}(3\cos^2\theta - 1), \quad \Theta_{2\pm 1}(\theta) = \mp \frac{\sqrt{15}}{2} \sin\theta \cos\theta \quad (2.4)$$

$$\Theta_{2\pm 2}(\theta) = \frac{\sqrt{15}}{4} \sin^2\theta, \quad \Phi_m(\phi) = \frac{1}{\sqrt{2\pi}} \exp(im\phi) \quad (2.5)$$

In order to get the energy values in E_{eg} and E_{t2g} symmetries, the 5×5 matrix of $V(r)$ can be diagonalized as follows,

$$\left(\begin{array}{c} \\ \\ \\ \\ \\ \end{array} V(r) \right) \rightarrow \left(\begin{array}{ccccc} E_{eg} & & & & \\ & E_{eg} & & & \\ & & E_{t2g} & & \\ & & & E_{t2g} & \\ & & & & E_{t2g} \end{array} \right) \quad (2.6)$$

$$\phi_1 = \phi_{320}, \phi_2 = \frac{1}{\sqrt{2}}(\phi_{322} + \phi_{32\bar{2}}), \phi_3 = \phi_{321}, \phi_4 = \phi_{32\bar{1}}, \phi_5 = \frac{1}{\sqrt{2}}(\phi_{322} - \phi_{32\bar{2}}) \quad (2.7)$$

$$E_{eg} - E_{t2g} = 10 Dq = \frac{1.67Ze^2}{a^5\epsilon_04\pi} \int_0^\infty r^4 R_{32}^2(r) r^2 dr \quad (2.8)$$

where $10 Dq$ is the crystal field splitting energy (the energy gap between the metal-based t_{2g} and e_g orbitals.) Fig. 2.3 (a) shows the energy level splitting when a free ion experiences the crystal field in cubic and tetragonal perovskite structures.

The wave-functions are recombined as follows and named $d\epsilon$ for d_{xy} , d_{yz} , d_{zx} and $d\gamma$ for $d_{x^2-y^2}$ and $d_{3z^2-r^2}$ orbitals, expressed in Eqn. 2.9. These functions are also plotted in Fig. 2.3 (b). In MnO_6 octahedron, the lobes of $d\gamma$ orbitals point in the direction of oxygen ions (O^{2-}), this increases their energy due to strong Coulombic repulsion of the MnO_6 octahedra whereas the $d\epsilon$ orbitals have lobes oriented between the oxygen ions.

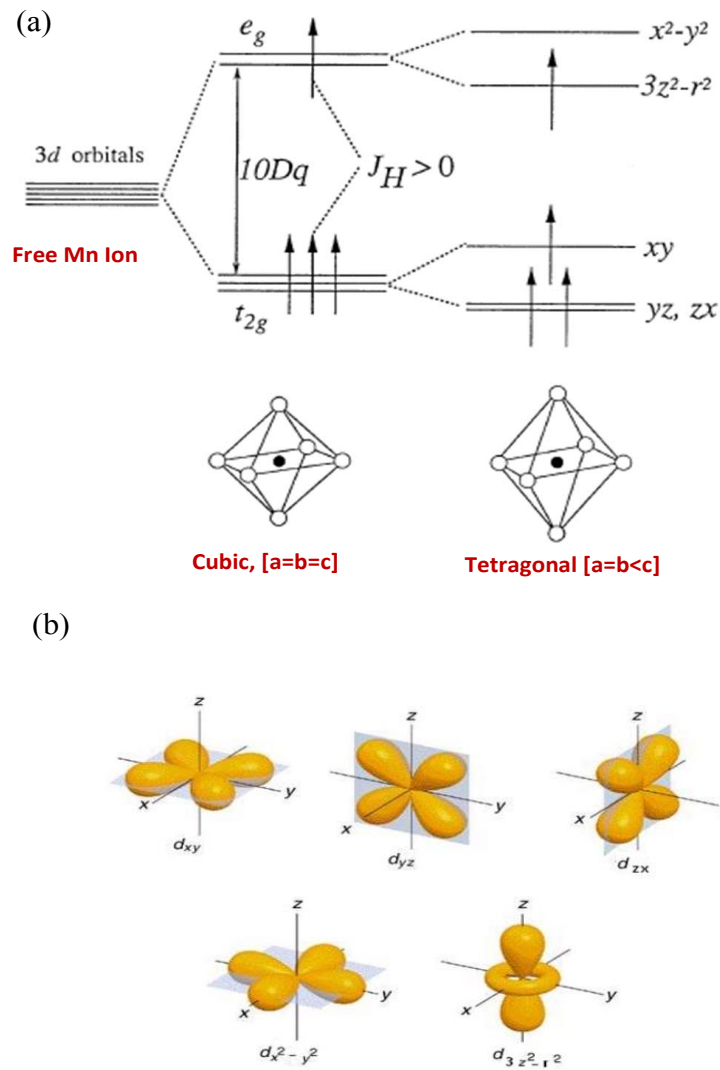


Figure 2.3: (a) d -orbital splitting by the crystal field in ABO_3 with perovskite structure in cubic (undistorted) and tetragonal (distorted) configurations. (figure taken from Tokura (1999)[18]) (b) Schematic representation of atomic orbitals.

$$\begin{aligned}
d_{xy} &= \sqrt{\frac{15}{4\pi}} R_{32}(r) \frac{xy}{r^2} = -\frac{i}{\sqrt{2}}(\phi_{322} - \phi_{32\bar{2}}) \\
d_{yz} &= \sqrt{\frac{15}{4\pi}} R_{32}(r) \frac{yz}{r^2} = \frac{i}{\sqrt{2}}(\phi_{321} + \phi_{32\bar{1}}) \\
d_{zx} &= \sqrt{\frac{15}{4\pi}} R_{32}(r) \frac{zx}{r^2} = -\frac{1}{\sqrt{2}}(\phi_{321} - \phi_{32\bar{1}}) \\
d_{x^2-y^2} &= \sqrt{\frac{15}{4\pi}} R_{32}(r) \frac{x^2-y^2}{r^2} = \frac{1}{\sqrt{2}}(\phi_{322} + \phi_{32\bar{2}}) \\
d_{3z^2-r^2} &= \sqrt{\frac{5}{16\pi}} R_{32}(r) \frac{3z^2-r^2}{r^2} = \phi_{320}
\end{aligned} \tag{2.9}$$

Free Mn^{+3} ion has 4 valence electrons which fill the d orbitals based on the Pauli exclusion principle (a quantum mechanical principle that two identical fermions (particle with half-integer spin) cannot occupy the same quantum state simultaneously). However, when the energy levels of Mn ions are split under the crystal field (i.e., in a cubic perovskite structure), the electrons are subjected to strong Hund's rule coupling (minimization of the Coulomb repulsion energy of the electrons on a given atom, while satisfying the Pauli exclusion principle). In this coupling, three electrons occupy the three available energy states in t_{2g} and the other remaining one occupies one of the empty e_g energy levels. In the case of tetragonal distortion, the degeneracy of the e_g orbitals are broken, with one orbital becoming lower in energy and the other higher than in the degenerate case. A System in a degenerate electronic state which becomes unstable and undergoes such distortion to form a system of lower symmetry and lower energy by removing its degeneracy is known to be Jahn-Teller (JT) effect. This electronic effects is named after Hermann Arthur Jahn and Edward Teller, who proved, using group theory that orbital

nonlinear spatially degenerate molecules cannot be stable.[20]

As mentioned previously, LaMnO_3 is an anti-ferromagnetic insulator. However, when a divalent ion (i.e., Ca^{+2}) is inserted at the rare-earth site forming $\text{La}_{0.7}\text{Ca}_{0.3}\text{MnO}_3$ for example the compound with a mixed-valent (Mn^{+3} and Mn^{+4}) manganese ions, it exhibits both metallic and ferromagnetic behavior. This indicates that the magnetic interactions between the Mn ions with different spin configurations have a profound effect on the material's conductivity. In the next section, we describe the magnetic-exchange interactions between the spins of adjacent ions and their relation to the material's conductivity.

2.2.3 Double-exchange mechanism

The empirical correlations between the ferromagnetism and the metallicity in doped manganites was discovered by Jonken and Van Santen in 1950.[21, 22] A year later Clarence Melvin Zener[23] proposed an explanation of the magnetic and transport properties of magnetic oxides. He noted that the two configurations in doped manganese oxides, namely;

$$\psi_1 : \text{Mn}^{+3} \text{O}^{2-} \text{Mn}^{+4} \text{ and } \psi_2 : \text{Mn}^{+4} \text{O}^{2-} \text{Mn}^{+3} \quad (2.10)$$

are degenerate and connected by the double-exchange (DE) matrix element. The matrix element is the consequence of the simultaneous electron transfer from Mn^{+3} to central O^{2-} and from O^{2-} to Mn^{+4} when the core spins of Mn ions are aligned ferromagnetically. The Fig. 2.4 shows schematically the

double exchange interaction between the Mn ions. When the core spins are parallel, the system resonates between the ψ_1 and ψ_2 , resulting in a ferromagnetic conducting ground state.

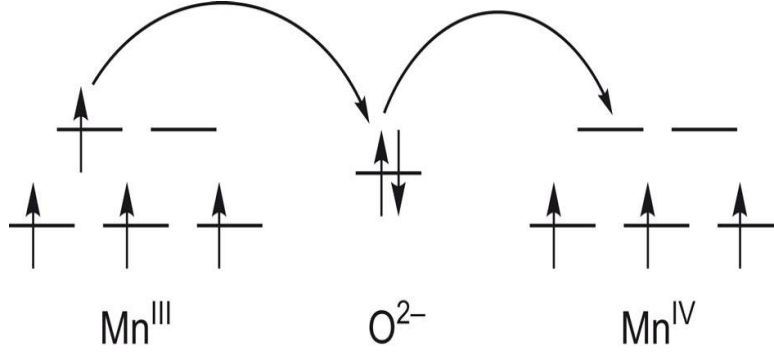


Figure 2.4: Double exchange process: Two electrons are simultaneously transferred, one from a bridging O^{2-} anion to the Mn^{4+} center and other from a Mn^{3+} center to the O^{2-} anion. Note that spins of t_{2g} electrons for Mn^{3+} and Mn^{4+} are ferromagnetically coupled. (Figure is reproduced from [25])

He then later developed a quantitative relationship between the electrical conductivity and the ferromagnetic Curie temperature given by the formula;

$$\sigma = \left(\frac{xe^2}{a_p h} \right) \left(\frac{T_C}{T} \right) \quad (2.11)$$

where x (eg. in $La_{0.7-x}Ca_xMnO_3$) is the doping level, a_p is the pseudo-cubic lattice parameter (or the Mn-Mn distance), h is the Planck's constant, e the charge of the electron, T is the temperature and the T_C is the magnetic Curie

temperature.

The Zener's DE theory was later revisited by Anderson and Hasegawa[24] where they treated the core spin of each Mn ion classically and the mobile electron quantum mechanically (large Hund (J_H) coupling limit). Their fundamental result was that the effective transfer integral t_{ij} (a charge carrier mobility) between the neighboring Mn ions (see Fig. 2.5) is proportional to $\cos(\theta/2)$, where the θ is the classical angle between the core spins, and

$$t_{eff} = b \cos(\theta/2) \quad (2.12)$$

where b is the transfer matrix element. The energy is lower when the itinerant electron's spin is parallel to the total spin of the Mn cores. This means that if the manganese spins are ferromagnetically aligned then the effective transfer integral will be maximized leading to a minimum electrical resistivity. This indicates that ferromagnetism and metallicity are intimately linked. In the case of antiferromagnetic coupling, the hopping amplitude is forbidden so the system becomes insulating. This provides a qualitative explanation between the metal to insulator transition and the Curie temperature. Indeed, during the application of magnetic field, the t_{2g} spins reduce the theta, consequently increase the hopping amplitude, therefore it produces less scattering in spin channel and thus increased conductivity.

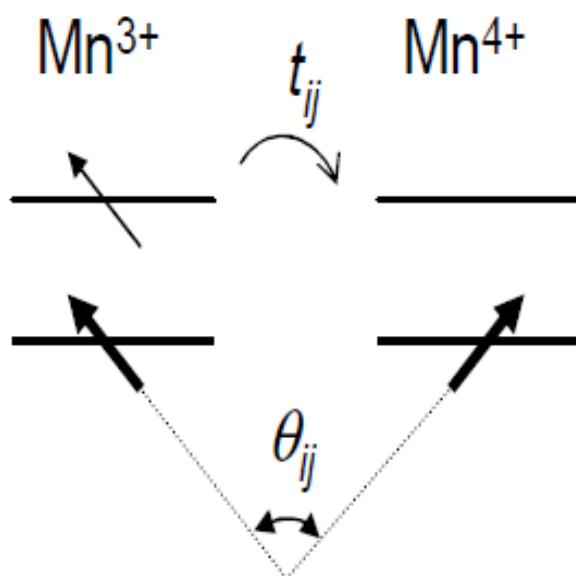


Figure 2.5: Representation of the hopping exchange integral in double exchange mechanism.

2.3 Electronic Phase Separation Phenomena

2.3.1 Multi-phase coexistence

Manganites appear to form phase separated states, where two competing phases reach an equilibrium by forming inhomogeneous patterns.[26] The competing phases may or may not have a different electronic density. But they have different symmetry breaking patterns. For instance, they tend to be ferromagnetic (all spins are parallel), or charge-ordered and anti-ferromagnetic (a staggered up and the down spin pattern). The manganite state in the CMR regime (a temperature region where the resistance drastically changes under magnetic field), shows percolative characteristics (metallic filaments across the sample; see Fig. 2.6 (a)). Metallic (percolative) and insulating regions have resistances R^{per}_M and R_I , respectively. The resistance of metallic region grows with an increasing temperature as any metal does while the resistance of insulating region increases with a decreasing temperature. This indicates that for a simple two-resistances in parallel description (see Fig. 2.6 (b)), it is natural to expect a peak in the effective resistance at intermediate temperatures. Applying a random resistive network model computationally using Kirchoff equations to a 100 x 100 random network clusters size, the net resistivity could be calculated. Figure 2.6 (c) shows the upper ($p=0$) and lower limiting case ($p=1$) where the sample shows fully insulating and metallic states respectively. 2D and 3D represent two and three dimensional square and cubic clusters. Percolative regime exists in the region between $p=0.4$ and $p=0.5$. It

shows a good agreement with the $(\text{La}_{5/8-y}\text{Pr}_y)\text{Ca}_{3/8}\text{MnO}_3$ (LPCMO) where the metallic fraction of p equals the amount of La in LPCMO.[27] The resistance of the insulating and metallic clusters are temperature dependent.

2.3.2 An interesting example: $\text{La}_{1-x}\text{Pr}_x\text{Ca}_{0.3}\text{MnO}_3$

$\text{La}_{1-x}\text{Pr}_x\text{Ca}_{0.3}\text{MnO}_3$ (LPCMO) is well-known and well studied phase separate manganite systems. Various microscopic studies have shown directly the percolative nature of this compound.[28, 29] A typical LPCMO sample is paramagnetic insulating (PI) at high temperatures. The compound enters into the charge-ordered insulating (COI) phase at around 220 K.[30] The size of the COI clusters is reduced at lower temperatures where the size of ferromagnetic metallic (FMM) clusters increases.[31] Around T_{MIT} , the balance between the FMM and COI phase is fragile (i.e., size of the clusters are sensitive to the change in temperature and magnetic field). At temperatures well below the T_{MIT} , the samples contain predominantly FMM phase. A direct evidence of the percolative nature of the LPCMO manganites has been demonstrated by Zhang *et al.*[32] and is shown in Fig. 2.7. Temperature dependence of the magnetic force microscopy (MFM) images has been collected during cooling (Fig. 2.7 (a)) and warming (Fig. 2.7 (c)). As confirmed from the MFM spectrum, FMM domains grow and merge at the T_{MIT} which leads to a steep drop the resistivity seen in Fig. 2.7 (b). On the other hand, during warming, the FMM domain size remains unchanged until near the T_{MIT} .

So far, we have discussed the percolative nature of LPCMO manganites.

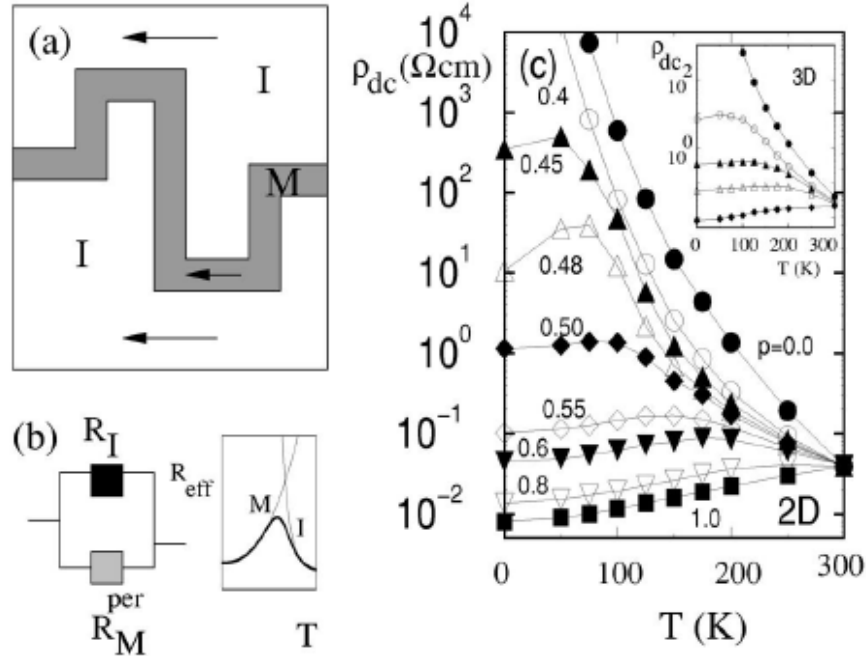


Figure 2.6: (a) Mixed-phase state near the percolation threshold where arrows indicate the conduction either through the metallic or the insulating regions, depending on temperature. (b) Two-resistance model for Mn-oxides. The schematic plot of the effective resistance R_{eff} vs. temperature for the parallel connection of metallic (percolative) R^{per}_M and insulating R_I resistances. (c) Effective resistivity ρ_{dc} vs. temperature produced for 100 x 100 random resistor network cluster. The $p=1$ (fully metallic) and 0 (fully insulating) are the limits taken from Ref.[27]. Figures adapted from Ref.[33].

But, why are LPCMO systems so important? There are several reasons for studying AMR phenomena in LPCMO manganites:

- LPCMO perovskite manganite is well known for its large-scale phase separation. This enables one to study the relationship between the self organized electronic phases and the AMR effect over a wide-range of temperature.
- The relative fraction of the coexisting ferromagnetic metallic (FMM) and charge ordered insulating (COI) phases in LPCMO rapidly changes with time. This allows one to investigate the response of anisotropic magneto-resistance (AMR) to the direct the competition between the electronic phases in this system.
- LPCMO contains ferromagnetic metallic FMM and charge order insulating COI domains of size of a few μm near metal to insulator transition temperature. LPCMO thin film bridges a few micrometer wide can be produced easily using standard wet-etch photolithography allowing one to investigate the AMR properties at the domain level.

2.3.3 Electron transport in manganites of reduced dimensions

When the dimension of the electronically phase separated manganite wire is reduced to a scale which is comparable with the inherent length scale ($\sim 1 \mu\text{m}$),^[10] the magneto-transport property of the system will be strongly affected.^[34, 35] The size of the phase separated domains in LPCMO film

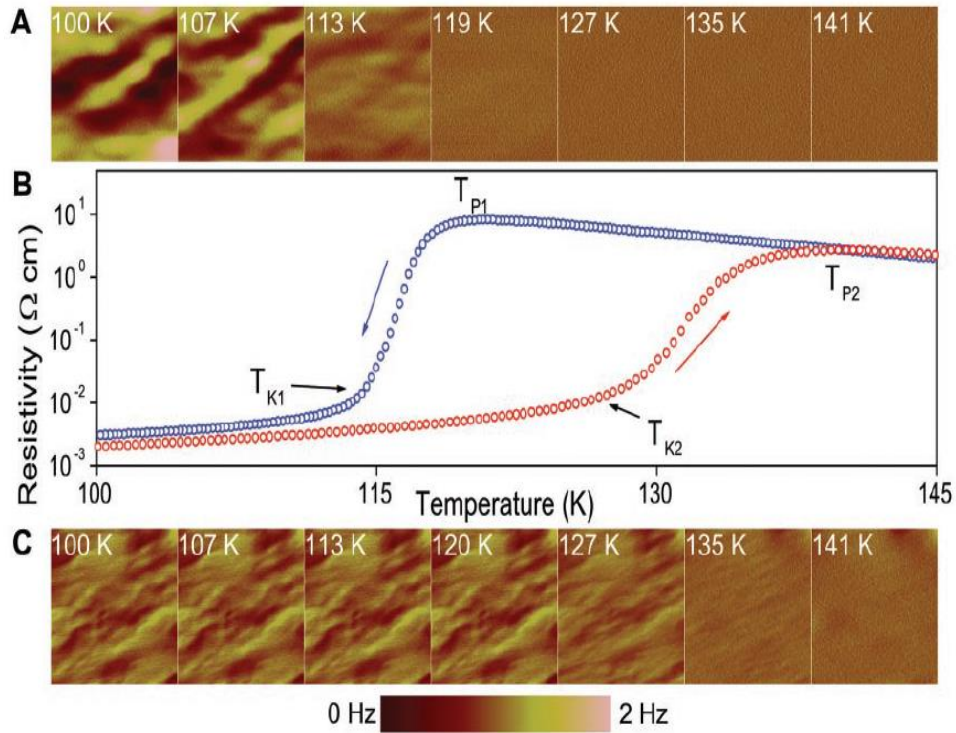


Figure 2.7: (a) Temperature dependence of the MFM image sequence for cooling. (b) The temperature dependence of the resistivity of the $\text{La}_{0.33}\text{Pr}_{0.34}\text{Ca}_{0.33}\text{MnO}_3$ manganite thin film over a thermal cycle. The blue curve corresponds to cooling and the red curve to the warming. (c) Temperature dependence of the MFM image sequence during warming cycle. Figure is reproduced from Ref.[32]

depends on the composition and temperature and ranges from nanometer to micrometer. As previously mentioned, the metal to insulator transition temperature in LPCMO system is percolative in nature. If the system size is reduced into a wire of a width comparable to the length scale of the FMM and COI domains, the electrical transport at an arbitrary point in the wire could be interrupted by an COI domain. This will may cause abrupt changes in the electrical resistivity in the samples (see Fig. 2.8 (a)). The amount of FMM phase increases at the expense of the COI phase due to the application of magnetic field which eliminates the jumps in the wire (see Fig. 2.8 (b)). However, the main issue in spatially confined systems is the reproducibility of the resistivity jumps. The drops in the resistivity do not take place at the same temperature or magnetic field. Computational studies performed on the phase separated LPCMO systems have shown that sizes as well as the distribution of metallic and insulating phases depends on the temperature.[36] This means that domain size and distribution of the phases are different for every temperature cycle, consequently producing resistance drops at different temperatures.

Time dependent resistivity measurement of spatially confined LPCMO wires due to fluctuations between the FMM and COI domains near the first-order phase transitions show that a universal and smooth transition does not occur in all these domains; instead, electronic phases in finite domains individually flip from a metal to an insulator. The transition time between two fluctuating domains has been described by Ward *et al.*[37]

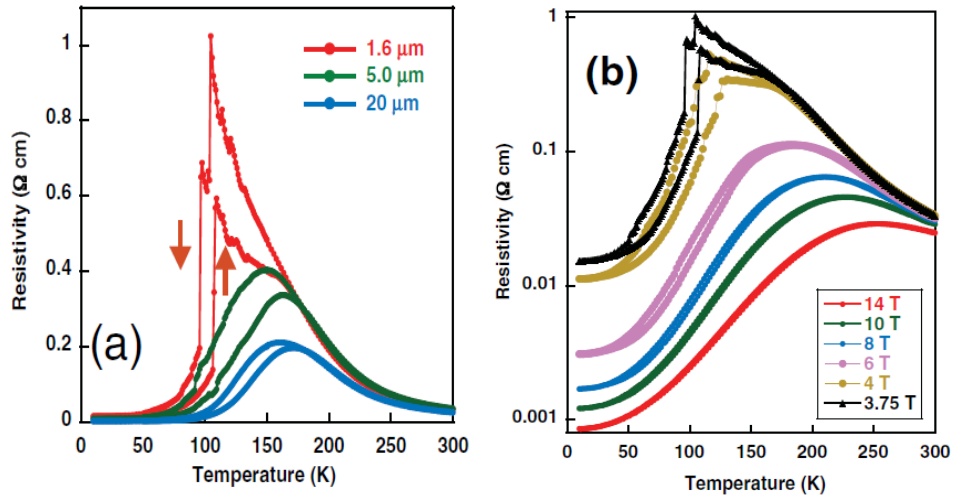


Figure 2.8: (a) Resistivity versus temperature for the LPCMO wires under magnetic field of 3.75 T. Arrows indicate the warming or cooling cycles. The 1.6 μm wire whose size is comparable to those of the FMM and COI domains, exhibits giant ultra-sharp peak in the temperature dependence of resistivity. (b) When the magnetic field increases from 3.75 T to 14 T, the jumps are reduced. Figure is adapted from Ref.[11]

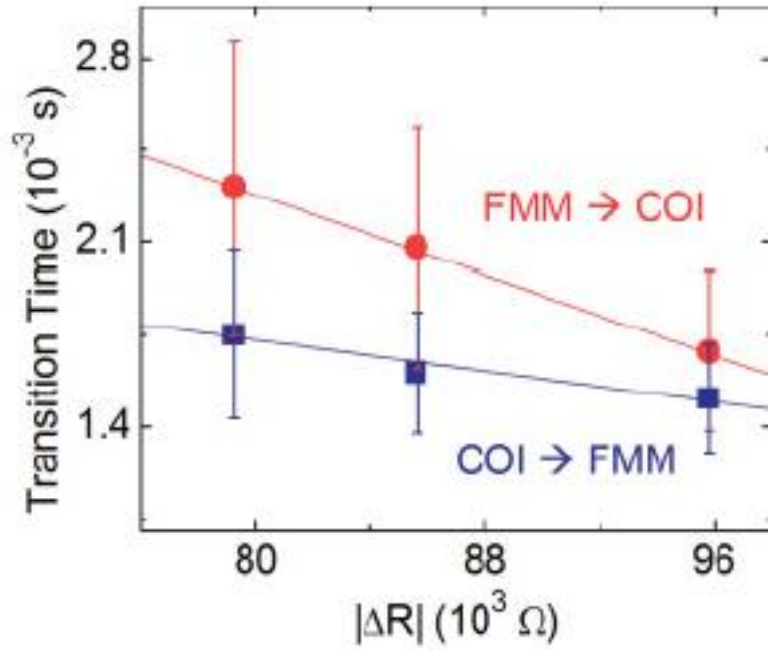


Figure 2.9: Transition time from a metal to insulator or insulator to a metal of a single electronic domain on each of the three background states in $10 \mu\text{m} \times 50 \mu\text{m} \times 70 \text{nm}$ LPCMO wire. The lifetimes are averages of those of thousands of individual transitions on each of the three background resistive states. In each case, it takes more time for the domain to transition from the disordered FMM phase to the ordered COI phase. Figure is adapted from Ref.[37]

$$R = A * e^{-t/\tau} \tag{2.13}$$

where R is the resistance, A is a constant, t is time, and τ is the transition lifetime. The transition time is from COI phase to the FMM one is shorter than that of to be shorter than from the FMM phase to the COI one (see Fig. 2.9).

All these observations indicate that phase separation in LPCMO manganite is dynamic where the formation of the metallic and insulating phases vary in size and shape. This in fact brings about a complexity in the underlying mechanisms of fundamental properties in these systems.

2.4 Theory of anisotropic magneto-resistance (AMR)

In 1857, William Thomson (Lord Kelvin) discovered the dependence of the resistance of iron and nickel on the “amplitude” as well as the “direction” of the applied magnetic field.[38] This effect is known as anisotropic magneto-resistance (AMR). In a ferromagnet, the orientation of the orbital angular momentum is coupled to the lattice of the ferromagnet which is fixed in a certain direction (i.e., easy axis). Therefore, the spin-orbit coupling influences the scattering rate of the conduction electrons and hence electrical resistance.

The resistivity of ferromagnetic film can be understood phenomenologically

from the symmetry considerations.[39] The electric field \mathbf{E} in the ferromagnetic film (see Figure 2.10) has two components: one is perpendicular to the magnetization \mathbf{E}_\perp one parallel to the magnetization \mathbf{E}_\parallel . Similarly, the current density \mathbf{J} can also be decomposed into \mathbf{J}_\perp and \mathbf{J}_\parallel . By using Ohm's law, the relation between the \mathbf{E} and \mathbf{J} can be shown by

$$E_\parallel = \rho_\parallel J_\parallel \quad (2.14)$$

$$E_\perp = \rho_\perp J_\perp \quad (2.15)$$

where

$$E_\parallel = |\mathbf{E}| \cos \theta \quad (2.16)$$

$$E_\perp = |\mathbf{E}| \sin \theta \quad (2.17)$$

and

$$J_\parallel = |\mathbf{J}| \cos \theta \quad (2.18)$$

$$J_\perp = |\mathbf{J}| \sin \theta \quad (2.19)$$

where θ represents the angle between \mathbf{J} and \mathbf{M} . Expressing the magnitude of the electric field and rearranging the equations as:

$$\begin{aligned} |\mathbf{E}| &= E_\parallel \cos \theta + E_\perp \sin \theta \\ &= |\mathbf{J}|(\rho_\parallel \cos^2 \theta + \rho_\perp \sin^2 \theta) \\ &= |\mathbf{J}|(\rho_\parallel - \rho_\perp) \cos^2 \theta + \rho_\perp \end{aligned} \quad (2.20)$$

The resistance depends on the angle θ between the magnetization M can be calculated as:

$$\rho(\theta) = \frac{|\mathbf{E}|}{|\mathbf{J}|} = \frac{\rho_{\parallel} + 2\rho_{\perp}}{3} + (\cos^2\theta - \frac{1}{3})(\rho_{\parallel} - \rho_{\perp}) \quad (2.21)$$

where ρ_{\parallel} and ρ_{\perp} are resistivities measured with the current flowing parallel and perpendicular to the direction of the magnetization respectively. This allows us to define the AMR as,

$$\rho_A = (\rho_{\parallel} - \rho_{\perp}) / (\frac{1}{3}\rho_{\parallel} + \frac{2}{3}\rho_{\perp}) \quad (2.22)$$

In most conventional metals, the AMR is about few percent and decreases with increasing temperature or decreasing magnetization. Whereas, in manganites, it can exceed 100 % [6] and its temperature dependence is non-monotonic.[40] These drastic differences in the AMR suggest that different mechanism must be involved in different materials.

A model proposed by Campbell [41] successfully describes the AMR in metallic alloys. This model is based on the scattering of the s waves on the d sites of these materials and properly describe the effects of impurity and the temperature dependence. Based on the Mott's two current model,[42] Smith *et al.*[43] proposed the spin orbit coupling for explaining the AMR effect in $3d$ ferromagnets:

$$H_{SO} = \lambda [L_Z S_Z + \frac{1}{2}(L_+ S_- + L_- S_+)] \quad (2.23)$$

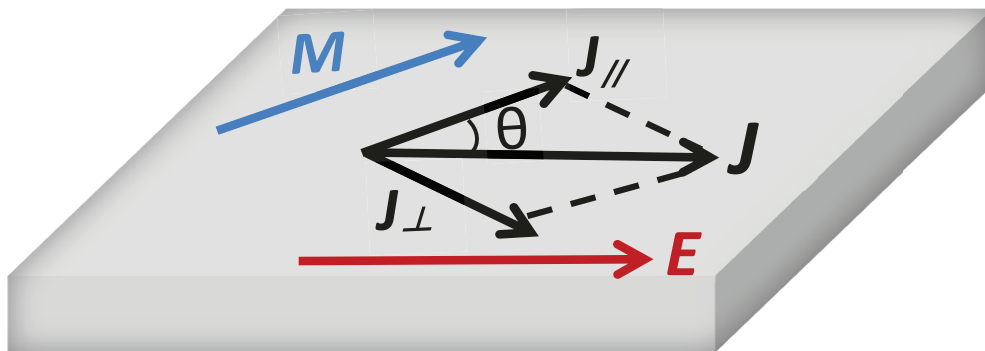


Figure 2.10: Resistance of the ferromagnet depends on the angle, θ between the current, \mathbf{J} direction and the magnetization, \mathbf{M} .

where λ is the spin-orbit (SO) coupling and the subscripts z , $+$ and $-$ indicate the z component and climbing operators of the spin S and the angular momentum L . The s electrons with two spin state (spin-up and spin-down) constitute two parallel conduction channels with resistivity of ρ_{\uparrow} and ρ_{\downarrow} and when the spin-flip ($\rho_{\uparrow\downarrow}$) process is taken into account, the total resistivity is shown:

$$\rho = \frac{\rho_{\uparrow}\rho_{\downarrow} + \rho_{\uparrow\downarrow}(\rho_{\uparrow} + \rho_{\downarrow})}{\rho_{\uparrow} + \rho_{\downarrow} + 4\rho_{\uparrow\downarrow}} \quad (2.24)$$

For each spin current, the resistivity comes from the dominated s - d and minor s - s scattering described as $\rho_{\sigma} = \rho_{s\sigma} + \rho_{s\sigma \rightarrow d}\mu$ where μ and σ represent the spin state of d and s electrons. From the spin-orbit coupling SO, d orbitals are unevenly mixed which causes $\rho_{s\sigma \rightarrow d}\mu$ dependent on the magnetic field directions. When we donate the resistivity changes $\Delta\rho_{\uparrow}, \Delta\rho_{\downarrow}$ between $\mathbf{M} \parallel \mathbf{J}$ and $\mathbf{M} \perp \mathbf{J}$ of the spin-up and spin-down channels, the general expression of the resistivity changes are expressed according to Ref.[44]

$$\begin{aligned} \Delta\rho_{\uparrow} &= \gamma_{\uparrow\uparrow}\rho_{\uparrow} + \gamma_{\uparrow\downarrow}\rho_{\downarrow} \\ \Delta\rho_{\downarrow} &= \gamma_{\downarrow\uparrow}\rho_{\uparrow} + \gamma_{\downarrow\downarrow}\rho_{\downarrow} \end{aligned} \quad (2.25)$$

For strong ferromagnets (i.e., dilute Ni alloys), $\rho_{\downarrow} \gg \rho_{\uparrow}$. In this case equation 2.24 becomes to $\Delta\rho_{\downarrow} = -\gamma\rho_{\downarrow}$ and $\Delta\rho_{\uparrow} = -\gamma\rho_{\downarrow}$. By neglecting the spin-flip scattering, Campbell *et al.* [3] obtained the following equation:

$$\frac{\Delta\rho}{\rho} = \gamma(\alpha - 1) \quad (2.26)$$

where γ is the spin-orbit coupling constant and $\alpha = \rho_{\downarrow} / \rho_{\uparrow}$.

However, this model is not appropriate for manganites where the carriers hop between the d states of the transition metal. General formula obtained by Döring [45] for the resistivity of a cubic ferromagnet with the magnetization in the $(\alpha_1, \alpha_2, \alpha_3)$ direction and the current in the $(\beta_1, \beta_2, \beta_3)$ direction can be calculated from:

$$\begin{aligned} \rho = & \rho_0 \left[1 + k_1(\alpha_1^2\beta_1^2 + \alpha_2^2\beta_2^2 + \alpha_3^2\beta_3^2 - \frac{1}{3}) \right. \\ & + 2k_2(\alpha_1\alpha_2\beta_1\beta_2 + \alpha_2\alpha_3\beta_2\beta_3 + \alpha_3\alpha_1\beta_3\beta_1) + \\ & k_3(s - \frac{1}{3}) + k_4(\alpha_1^4\beta_1^2 + \alpha_2^4\beta_2^2 + \alpha_3^4\beta_3^2 + \frac{2}{3}s - \frac{1}{3}) + \\ & \left. 2k_5(\alpha_1\alpha_2\alpha_3^2\beta_1\beta_2 + \alpha_2\alpha_3\alpha_1^2\beta_2\beta_3 + \alpha_3\alpha_1\alpha_2^2\beta_3\beta_1) \right] \end{aligned} \quad (2.27)$$

where $s = \alpha_1^2\alpha_2^2 + \alpha_2^2\alpha_3^2 + \alpha_3^2\alpha_1^2$.

Fuhr *et al.* [46] used this relation to calculate the normalized resistivity in a nearly cubic perovskite structure of $\text{La}_{0.75}\text{Sr}_{0.25}\text{MnO}_3/\text{SrTiO}_3$ (100) manganite film. Angle, θ between the electrical current \mathbf{I} and the magnetic field \mathbf{H} is the same as the angle between \mathbf{I} and the magnetization \mathbf{M} . The current I is applied either parallel to [100] or the [110] of the crystallographic axis of the LSMO, they obtained:

$$\frac{\Delta\rho(\theta)}{\rho(0)} \approx \begin{cases} C_1 \cos^2(\theta) + C_3[\cos^4(\theta) - \cos^2(\theta)] \text{ for } I \parallel [100] \\ C_2 \cos^2(\theta) - C_3[\cos^4(\theta) - \cos^2(\theta)] \text{ for } I \parallel [110] \end{cases} \quad (2.28)$$

where $C_1 = k_1 + k_2$, $C_2 = k_2$ and $C_3 = (k_4 - 3k_3)/3$ are constants. The experimental results have shown that C_2 and C_3 are negligibly small, and only C_1 is large.

As discussed before the octahedral symmetry around the Mn ion splits the $3d$ energy level into a lower triplet t_{2g} and higher e_g doublet. Fuhr *et. al.* [46] further described the spinless Hamiltonian on a cubic lattice:

$$H = \sum_{\langle ij \rangle \alpha \beta} t_{ij}^{\alpha\beta} c_{i\alpha}^\dagger c_{j\beta} \quad (2.29)$$

where the $t_{ij}^{\alpha\beta}$ are the hopping integrals which depend on the type of the orbitals α, β and the direction between adjacent i, j sites. When the spin-orbit (SO) coupling is included, the degeneracy of the e_g orbitals ($|z\rangle = |3z^2 - r^2\rangle$, $|x\rangle = |x^2 - y^2\rangle$) is lifted. The coupling between the $e_g\uparrow$ and $t_{2g}\uparrow$ orbitals (separated by a crystal field of about 1.5 eV) is taken into account. The characteristic of these two non degenerate orbitals ($|1\rangle, |2\rangle$) depend on the direction of the applied magnetic field. From the second order perturbation theory, one can obtain the shift and the coupling of the two original e_g orbitals for the magnetization in a given direction (θ_B, ϕ_B) , spherical coordinates referred to axes parallel to the crystalline axes is expressed as spin-orbit Hamiltonian;

$$H_{SO} = g \begin{pmatrix} 3\sin^2(\theta_B) & \sqrt{3}\sin^2(\theta_B)\cos^2(2\phi_B) \\ \sqrt{3}\sin^2(\theta_B)\cos^2(2\phi_B) & \sin^2(\theta_B) + 4\cos^2(\theta_B) \end{pmatrix} \quad (2.30)$$

where $g = \lambda^2 / \Delta_{CF}$, λ is the SO coupling constant and the Δ_{CF} the crystal field splitting between t_{2g} and e_g orbitals. From this perturbation, new energy levels ($\varepsilon_{1,2} = g(2 \mp \Delta)$) and eigenvectors can be calculated as:

$$|1\rangle, |2\rangle = \frac{a \mp \Delta}{r_{1,2}} |z\rangle + \frac{b}{r_{1,2}} |x\rangle \quad (2.31)$$

where $a = \sin^2(\theta_B) - 2\cos^2(\theta_B)$

$b = \sqrt{3}\sin^2(\theta_B)\cos(2\phi_B)$

$\Delta = \sqrt{x^2 + b^2}$

$r_{1,2} = \sqrt{(a \mp \Delta)^2 + b^2}$

the conductivity in a given direction \hat{r} [47] is:

$$\sigma_{\hat{r}} = e^2 \tau \int d^3k |v_{\hat{r}}(\vec{k})|^2 \frac{\partial f}{\partial \varepsilon(\vec{k})} \quad (2.32)$$

with $v_{\hat{r}}(\vec{k}) = \hat{r} \cdot \vec{\nabla} \varepsilon(\vec{k})$ and $f(\varepsilon)$ is the Fermi function and τ is the isotropic relaxation time. The conductivity, σ enters the current density expression:

$$\vec{J} = \sigma \cdot \vec{E} \quad (2.33)$$

Because of the cubic symmetry of the LSMO system, all non-diagonal components of the conductivity tensor are equal to zero. The argument of the

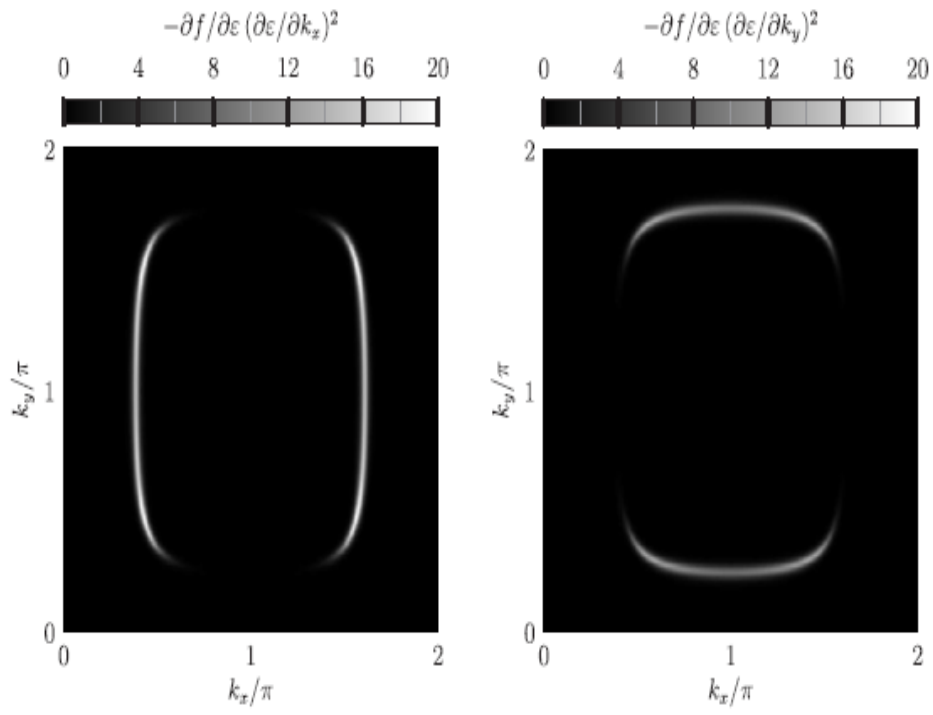


Figure 2.11: Density plot of the argument of the integral defined in equation 2.31 for H, M in the x direction, and $k_z = \pi/2$. Figure is adapted from Ref.[46]

integral in equation 2.31 for σ_{xx} and σ_{yy} is shown in Fig. 2.11 as a density plot, in the (k_x, k_y) plane, for the magnetization in the x direction and $k_z = \pi/2$. For this figure, Fuhr *et al.* again used large values for the SO coupling ($g/t = 0.2$) and the electronic temperature ($k_B T_e/t = 0.05$) to better visualize the effect. It shows that the integrand to obtain σ_{xx} (parallel to H) is larger than the corresponding value for σ_{yy} , leading to a lower resistivity.

Figure 2.12 shows the numerical results obtained for the normalized conductivity as a function of magnetization direction β , compared to the simple form of $\cos(2\beta)$. The results obtained by Fuhr *et al.* suggest that a simple tight-binding model (a model that calculates the electronic band structure using an approximate set of wave functions based on the superposition of wave functions for isolated atoms located at each atomic site),[48] which includes the on-site SO coupling, is able to explain the main features including sign, magnitude of the low temperature AMR in single crystal manganite films. Just as the authors have stated, the proposed model is just a starting point and its extension would be difficult to explain AMR at higher temperatures due to the complicated polaronic effects.

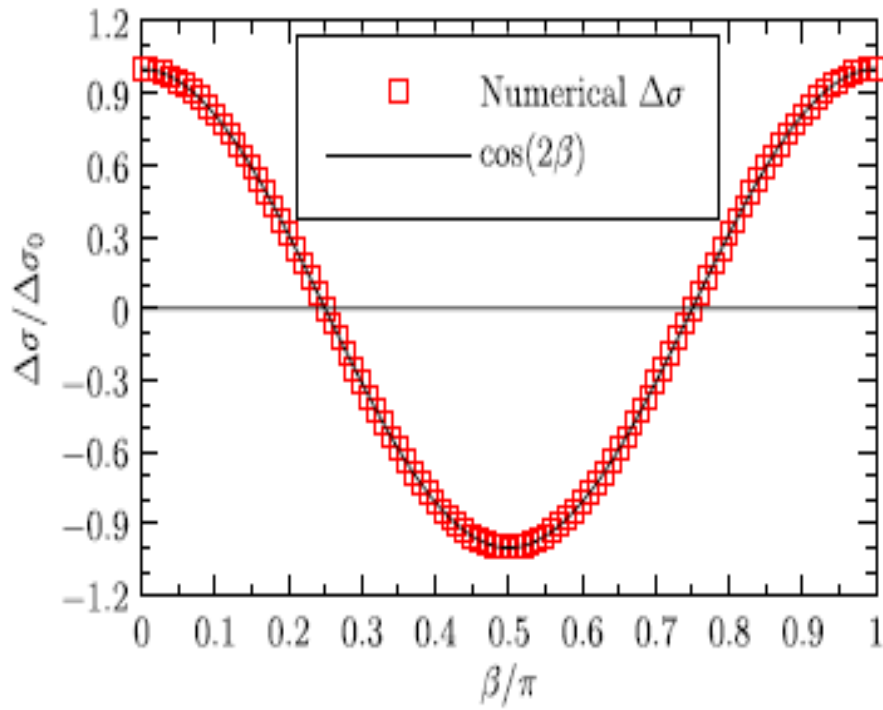


Figure 2.12: Numerical results for the normalized conductivity. Solid line shows the $\cos(2\beta)$ dependence behavior of the conductivity. Figure is adapted from Ref.[46]

CHAPTER 3

Experimental Aspects

3.1 Introduction

The details of the experimental techniques which have been used to obtain the results described in this dissertation are presented in this chapter. First, I present the methods used to prepare the $\text{La}_{0.7-x}\text{Pr}_x\text{Ca}_{0.3}\text{MnO}_3$ (LPCMO) polycrystalline (bulk), thin film materials and the micron-size patterned thin film devices; followed by the structural characterization. In the remaining part of this chapter, I describe procedures for the magneto-transport measurements, such as temperature, field, time dependent resistance measurement of LPCMO films and devices as a function of angle between the current and magnetic field.

3.1.1 Polycrystalline (Bulk) LPCMO samples

Polycrystalline samples of $\text{La}_{0.7-x}\text{Pr}_x\text{Ca}_{0.3}\text{MnO}_3$ (LPCMO) ($0.0 \leq x \leq 0.7$) were prepared by using the high temperature solid state reaction method.[49, 50] In order to prepare stoichiometric $\text{La}_{0.3}\text{Pr}_{0.4}\text{Ca}_{0.3}\text{MnO}_3$, a well-mixed prescribed ratio of La_2O_3 , Pr_6O_{11} , CaCO_3 , and MnO_2 were first reacted at 1200 C° for 24 hours in air. The resulting samples were reground and sintered twice using the same annealing conditions. Then the pellet-shaped samples were finally sintered at 1200 C° for 48 hours, and subsequently furnace cooled to the room temperature with a rate of 10 C°/min. In order to verify the sample's stoichiometry, rectangular-shaped bars were cut out from these pellets and magneto-transport measurements were performed to compare the sample's metal-insulator and magnetic Curie temperatures with the values previously reported in the literature. To check the samples purity, the remaining parts of the pellet were pulverized and used in a powder X-Ray diffraction analysis. After all the structural and magneto-transport results verified the desired stoichiometry, the same preparation method have been applied to produce the disk of an 1 inch in diameter, which has used as a target for thin film deposition.

3.1.2 Thin film growth and device fabrication

In situ off-axis magnetron sputtering of manganite is the simplest method to produce high quality thin films since the deposition is well controlled and allows a slow growth of films over large area. The principle of magnetron sputtering

relies on the momentum transfer of an ionized argon gas (i.e., gaseous plasma) to atom of the target (see Figure 3.1). The ejected atoms from the target are deposited on a heated substrate which is located a few cm away from the sputtering source.[51] The ejected sputtered atoms should be able to move freely towards the substrate with little impedance to their movement. This is why sputter coating is a vacuum process. Lower pressures can maintain high ion energies by preventing too many atom-gas collisions after ejection from the target.[52]

In this dissertation, we have used commercially available (100) oriented and one-side polished cubic SrTiO₃(STO), LaAlO₃(LAO) and orthorhombic (100) oriented NdGaO₃ (NGO) single crystal substrates. Cleanliness of the substrates is essential for obtaining high quality epitaxial thin films since dust and other contaminants can collect on a substrate and prevent epitaxial deposition of the film. Prior to the deposition, the substrates were carefully cut to a desired size using a diamond wire saw. Then the substrates were cleaned with a solution of liquid-detergent and deionized water at 70 C° for half an hour followed by the ultrasonic bath in an acetone. They were subsequently rinsed with hot distilled water and isopropyl alcohol (IPA). The substrates were attached to the nickel plate using silver paste to increase thermal conductivity between the heater and the substrates. The silver paste was left to dry in air for few hours. The nickel plate was then placed on the heater and the chamber was evacuated using a cryopump to a base pressure of about 1×10^{-7} Torr. The temperature of the substrates were controlled by a temperature controller with a stability of ± 1 C°. The substrate's temperature was

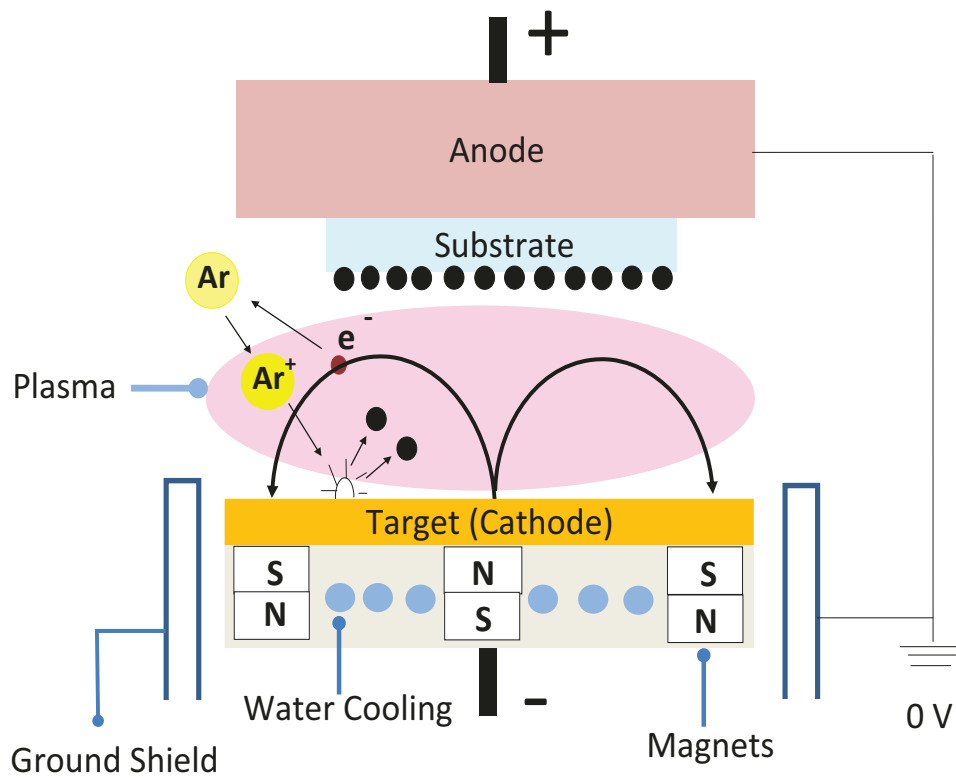
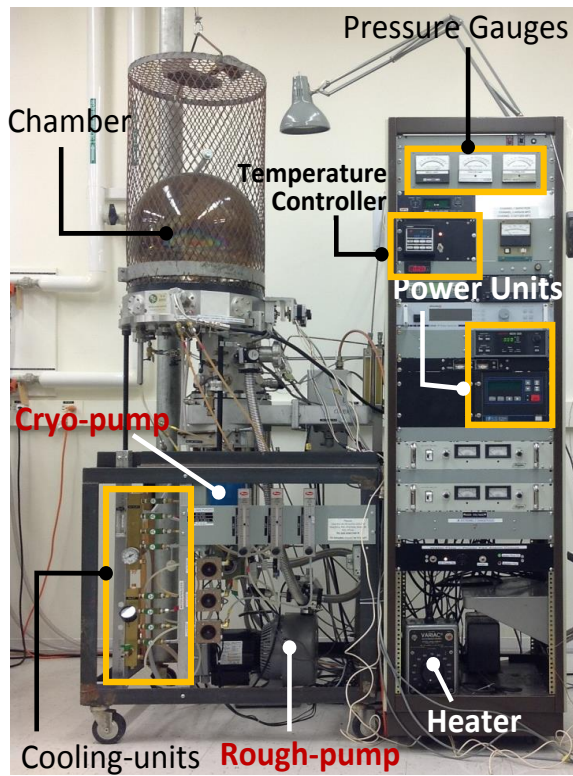


Figure 3.1: Physics of magnetron sputtering. Neutral Argon atoms are ionized when a strong potential difference (DC) is applied between the anode and cathode. The ions are then accelerated to a target. After the collisions with the surface of target, atoms are released (sputtered) and travel to the substrate and form layers of atoms in the thin film.

~ Sputtering System General View ~



~ Inside the Chamber ~

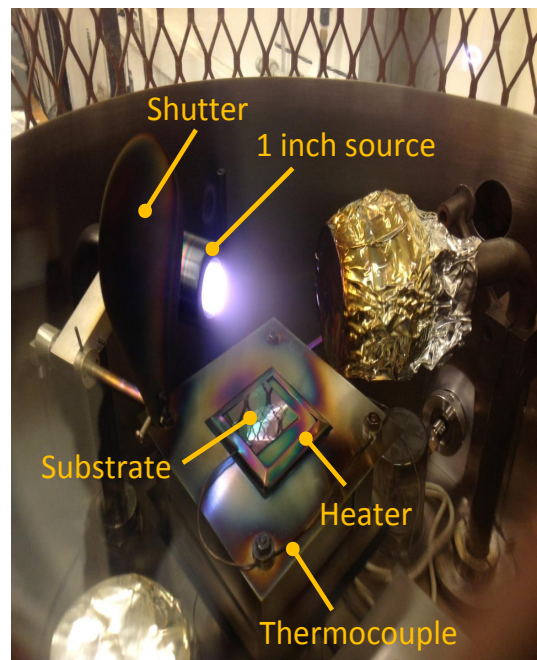


Figure 3.2: Magnetron sputtering systems. The picture on the right taken during LPCMO epitaxial thin film deposition.

raised to 750 C°. Before deposition, the target was pre-sputtered at 30 W for 10 minutes onto the shutter plate in order to clean it. During deposition, the power level was set to 50 W. The deposition system is shown in Figure 3.2. After the deposition of the thin film, the shutter is closed and the chamber is filled with oxygen with a pressure close to atmospheric pressure. The film was annealed at these conditions at 650 C° for 3 hours. Annealing in oxygen is essential since it ensures the optimum oxygen content in manganite thin films. Finally, after annealing, the films were cooled down to room temperature with a rate of about 15 C°/min.

Micro-lithography is one of lithographic patterning method that is capable of structuring thin film material on a fine scale.[53] The films investigated in this dissertation were patterned at the Nanofab facility of University of Alberta. The detailed fabrication process [54] can be seen in Figure 3.3 (a). We patterned LPCMO films on 5 x 10 mm² substrates. HPR 504 photo-resist layer was spread on it using spinner at 500 rpm for 10 s followed by spinning at a speed of 4000 rpm for 40 s. The photoresist-coated films were then prebaked on a hot plate at around 115 C° for 90 seconds. The photoresist was then exposed to intense ultra-violet (UV) light for 3 seconds. The exposed light results a chemical change that allows photoresist to be removed by applying a 354 developer (sodium hydroxide solution) for 20 seconds. After developing process, we etched the uncovered part of the film using the solution of HCl+KI+H₂O with an etching rate of about 1 nm/s. The sample was then rinsed with deionized water, an acetone and IPA. Patterned films were carefully inspected using optical microscope (see Fig. 3.3 (b)).

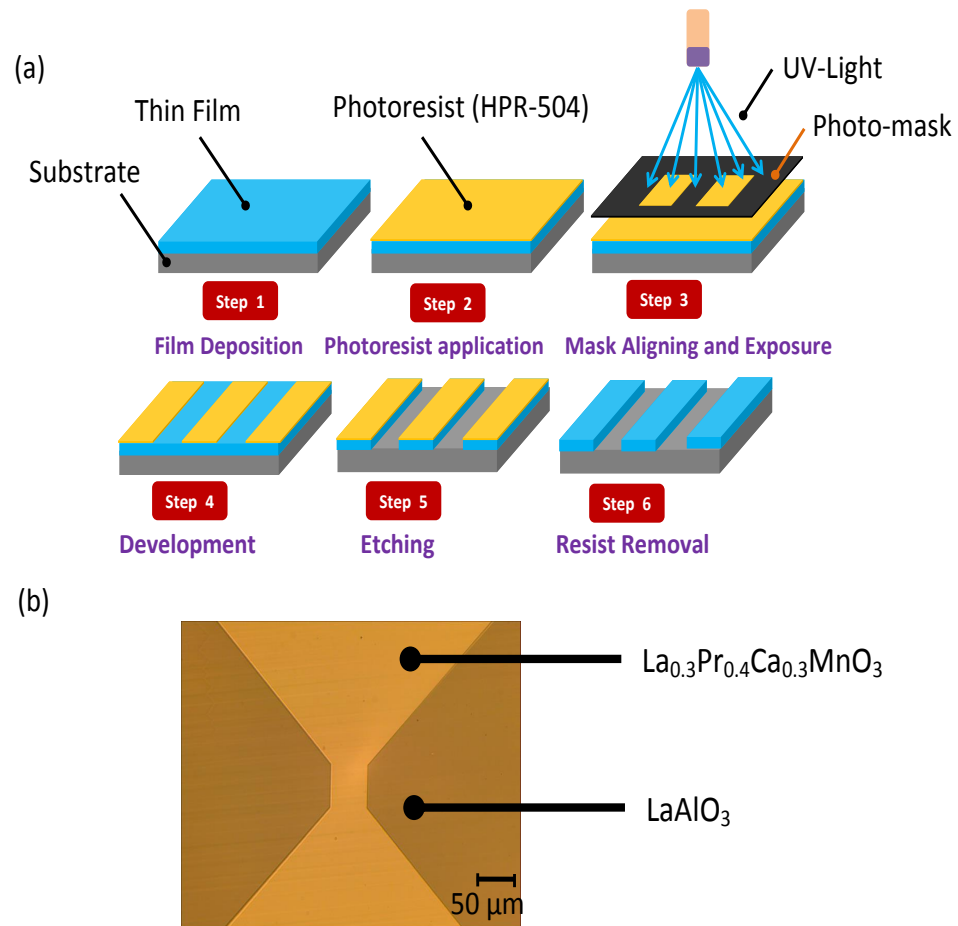


Figure 3.3: (a) Step by step photo-lithography process for manganite film based device fabrication. (b) A picture taken during inspecting the 50 micro- meter wide $\text{La}_{0.3}\text{Pr}_{0.4}\text{Ca}_{0.3}\text{MnO}_3$ bridge patterned on (001) oriented LaAlO_3 single crystal substrate.

3.2 Sample characterization

The main characterization techniques in this dissertation are listed in two sections: (i) Structural characterization which includes the powder and thin film diffractions measurements using Rigaku X-ray diffractometer. (ii) Magneto-transport measurements, which covers the details of resistance measurements as a function of temperature, field, time and the angle between the current and the field for all samples investigated in this dissertation.

3.2.1 Structural characterization

X-ray diffraction (XRD) θ - 2θ scans were used to examine the crystallographic quality, phase purity and lattice constants of the manganite bulk and thin films. The scans were performed at room temperature (300 K) on a 12 kW Rigaku X-ray diffractometer with a rotating anode and Cu-K α line radiation. Figure 3.4 (a) shows the XRD spectrum of polycrystalline (bulk) $\text{La}_{0.35}\text{Pr}_{0.35}\text{Ca}_{0.3}\text{MnO}_3$ (LPCMO) sample. The XRD pattern was fitted via Rietveld method using the FULLPROF Suite program to calculate the lattice parameters. Refinement results indicate that the LPCMO is a single phase with $Pbnm$ perovskite phase. The XRD spectrum of LPCMO (Pr=0.35) thin films deposited on (001) oriented LaAlO_3 and SrTiO_3 respectively, are shown in Figs. 3.4 (b) and (c). Films are epitaxially grown with the c -axes normal to the film plane. As indicated in the figure, 001 and 002 peaks in LPCMO/LAO and LPCMO/STO peaks are located at angles of 22.98° and 47.01° and 23.24°

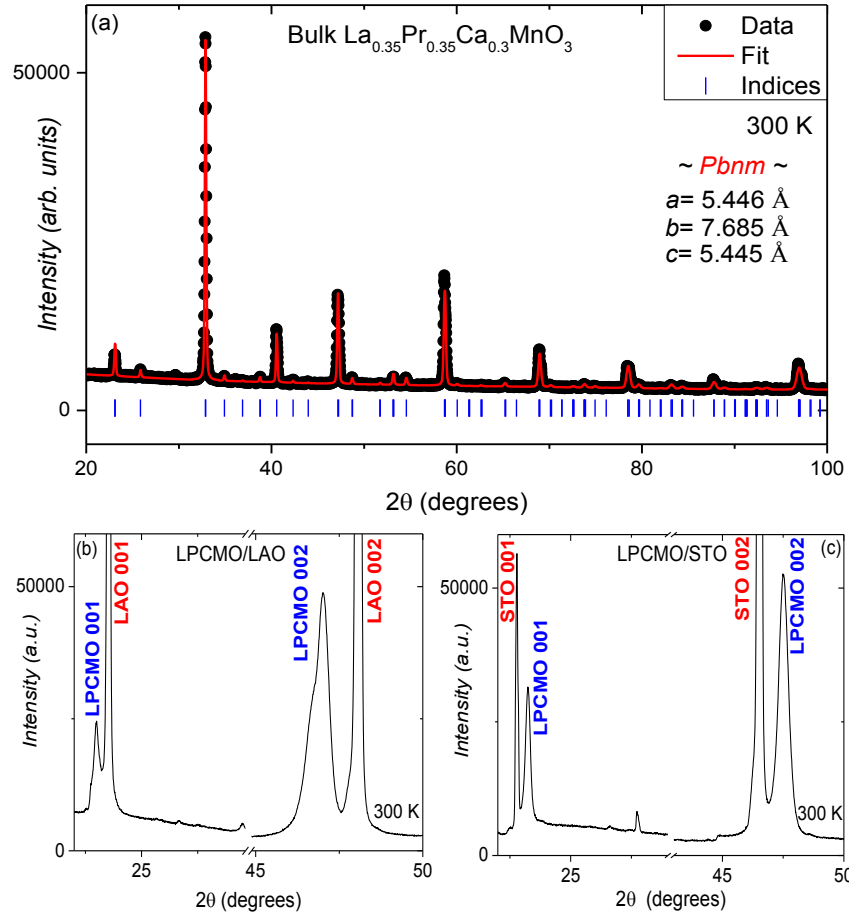


Figure 3.4: (a) Room-temperature X-ray diffraction (XRD) pattern for polycrystalline $\text{La}_{0.35}\text{Pr}_{0.35}\text{Ca}_{0.3}\text{MnO}_3$ (LPCMO) obtained using Rietveld refinement. (b) and (c) 45 nm thick LPCMO (Pr=0.35) films deposited on LaAlO_3 and SrTiO_3 single crystal substrates.

and 47.51° , respectively. The corresponding average c lattice parameters calculated from 001 and 002 peaks for 45 nm thick LPCMO films grown on LAO and STO substrates are $3.86 \text{ \AA} (\pm 0.01 \text{ \AA})$ and $3.82 \text{ \AA} (\pm 0.02 \text{ \AA})$, respectively. Once the lattice parameters of the bulk and the films are determined, one can calculate the lattice strain of each composition. The epitaxial strain studied in this dissertation can be calculated using the following equation;[55]

$$\epsilon_z = (100\%)(c_{film} - c_{bulk})/c_{bulk} \quad (3.1)$$

where c_{film} and c_{bulk} represent the lattice parameters of c -axes of the film and bulk manganites, respectively.

3.2.2 Magneto-transport measurements

The setup that was used to perform magneto-transport measurements consist of the following major parts: cryogenic apparatus, sample holder, non-superconducting electromagnets and motorized angle controller system. Figure 3.5 shows the general view of the magneto-transport measurement system. The details of these parts which constitute the transport system are presented below.

Cryogenic apparatus consist of Sumitomo RDK-408D2 closed cycle refrigerator system which provides 1.0 Watt of cooling power at 4.2 K temperature and can reach 3 K minimum temperature on the cold head without any heat load. The closed cycle system is run by the compact water cooled helium

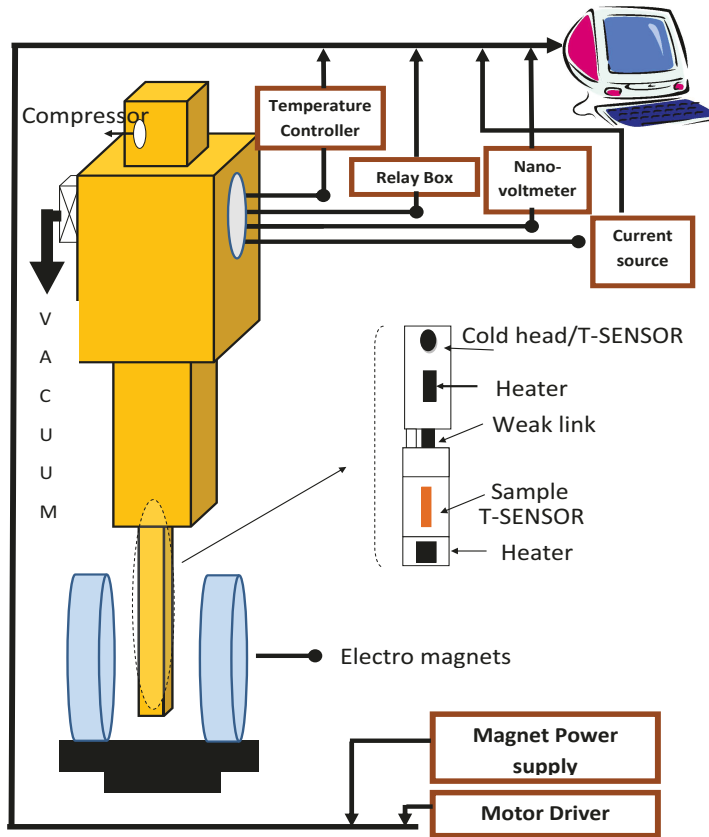


Figure 3.5: Diagram of AMR measurement circuitry.

compressor (CSW-71).

The magnetic field was applied to the sample using a horizontal electro-magnet (GMW 3473-70, Dipole Electromagnet) with a maximum 96 mm gap between the coils and maximum 70 Amp coil pair. The electro magnet was water-cooled. The magnet provides a maximum field of 1.1 Tesla powered by a unipolar power supply (Elgar, model SGA60/83C-1CAA). The magnetic field generated by this power supply was measured and recorded by a Hall probe and a Lakeshore Gaussmeter. The calibration curve (voltage versus magnetic field)

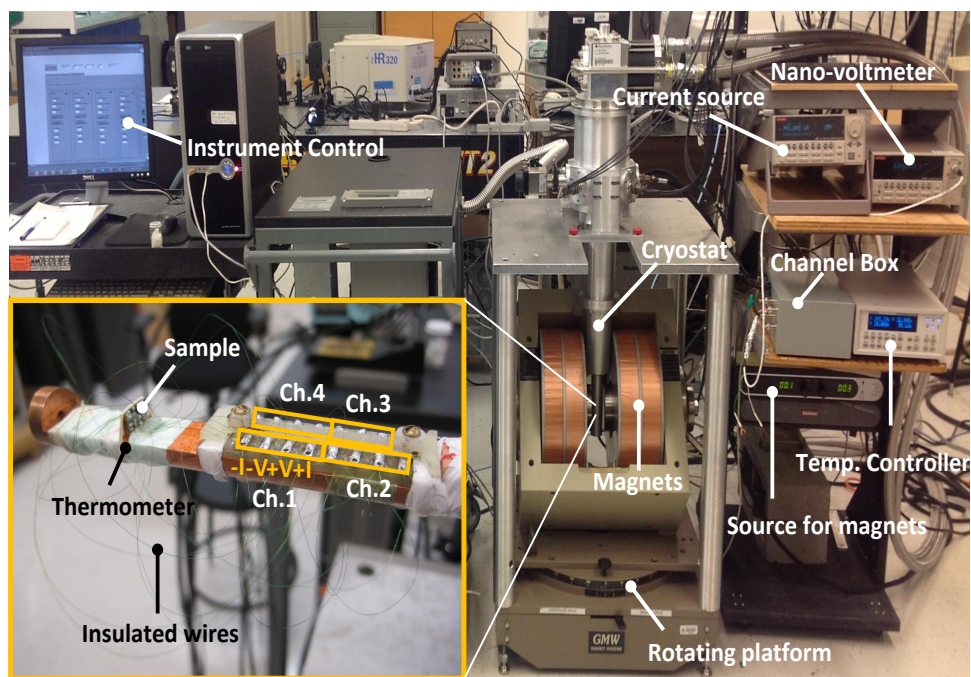


Figure 3.6: A view of the magneto-transport measurement set-up. Left inset shows the electrical connections to thin film sample.

was used in the Labview programming to read the magnitude of magnetic field generated at the center between the magnets. The electro-magnet is motorized and allows the field rotation with a resolution of 0.1 degree. The rotating platform of the electro-magnet is controlled by a microprocessor based step motor.

The sample holder consists of a oxygen free copper block mounted to the cold head (Sumitomo RDK-408D2). A thin layer of Apiezon N type grease

was applied between the copper sample holder and the cold head in order to maintain good thermal coupling. This Kapton foil was attached to the copper block using Apiezon grease in order to isolate the sample electrically from the conducting copper. The samples were directly attached to the Kapton foil with an Apiezon grease. The grease provides good thermal contact between the sample, Kapton foil and the copper block. Temperature sensor (LakeShore Cernox CX -1050 - AA) was attached directly to the copper sample holder. Sample temperature was controlled using 50 Watt (CADDOCK MP850) thick film resistor, attached to the copper sample holder near the cold head. In order to provide better stability of the temperature of the sample, another (CADDOCK MP850) thick film resistor was mounted on the sample holder. A LakeShore 332 temperature controller was used for controlling the temperature of the sample. Proportional integral derivative (PID) parameters were adjusted separately for several temperature zones from 10 to 325 K.

Resistance measurements:

Electrical resistance measurements of all samples studied in this dissertation were performed using four point probe technique.^[56] Four silver contacts were deposited on a manganite samples where the outer and inner contacts were used to apply the current and the read voltage of the samples. For bulk and normal wide (i.e., millimeter wide) manganite thin films, the 1 μ A current was applied to the samples in the form of short pulses in both directions. This eliminates the charge accumulation, background noise and the Joule heating. The voltage of samples was measured using Keithley 2182 nanovoltmeter which was paired with Keithley 6221 current source. The Keithley 2182 nanovoltmeter

was operated in delta mode. This mode allows the measurement and calculation of the voltage for the automatic DC current reversal which cancels out any constant thermoelectric offsets produced in the leads. The delta voltage is calculated as:

$$V(\text{Delta}) = \frac{V1 - V2}{2} \quad (3.2)$$

where, $V1$ and $V2$ are the measured voltages on the positive and the negative phases of the current source. Each delta mode measurements were repeated ten times and only the average value of the ten measurements, the maximum and the minimum values were stored to the computer. In the case of manganite bridges, a Keithley 6221 DC/AC source was used to provide a constant current of $1\mu\text{A}$ to the film, the voltage was measured subsequently with a Keithley 2182A nanovoltmeter. The resolution of the nanovoltmeter was set to 50 ns which compromise between the noise and the speed were acceptable for the measurements. The measurement of voltage (or resistance) with this technique is important since any sudden electronic domain change in the manganite bridges can be measured at a better resolution. However, these sudden changes can not be properly measured with Delta-mode due to time-delay produced during averaging the maximum and minimum voltages. Resistance measurements for the manganite bridges are extremely sensitive to the external noise. To minimize the noise, all the wires and the connections were shielded properly. The detailed procedure of resistance measurements are described below.

Temperature and time dependent resistance measurements:

Temperature (T) and time (t) dependence of the resistance of samples were measured between 10 K and 300 K either in zero or in a 1.1 Tesla magnetic field. Before measurements, samples were first cooled down in a zero field from 300 K to 10 K. When the temperature was stabilized at 10 K, $R(T)$ was measured during warming from 10 K to 300 K. The measurements of $R(t)$ under magnetic field of 0 and 1.1 Tesla were performed using the following procedure: At 10 K, resistance was measured over a time of 100 minutes at a values of constant θ (i.e., $\theta = 0^\circ$). The magnetic field was always turned off right after the time measurements. Then the sample's temperature was increased until it reached the temperature of the measurement under 0 Tesla.

Hysteresis - $R(H)$ measurements:

The hysteresis, $R(H)$ was measured at $\theta = 0^\circ$, where the magnetic field \mathbf{H} was kept to parallel to current direction \mathbf{J} . The field is first increased from 0 to 1.1 T with 0.1 T step and subsequently decreased with the same step to 0 Tesla.

Angular dependence of resistance, $R(\theta)$ measurements:

In this dissertation, angular dependent resistance $R(\theta)$ measurements between the magnetic field and the current were performed for two different orientations of the magnetic field with respect to the current directions. The “in-plane” and the “out-of-plane” resistance measurements were used to determine the magneto-resistive anisotropy of the samples studied.[57, 58, 59]

The out-of and in-plane AMR configurations are shown schematically in Figure 3.5. In order to measure out-of plane AMR, the applied magnetic field

is rotated towards the c -axis of the film. For in-plane AMR, the field is rotated in the ab plane of the film. Note that during the rotation of the magnetic field, the transport current direction is fixed. The detailed measurement procedure of the $R(\theta)$ is the following: after cooling down the samples from 300 K to 10 K in a zero field, a magnetic field \mathbf{H} of 1.1 T was applied at certain angle relative to the direction of the current \mathbf{J} , then the sample temperature was increased until it reached the temperature of the measurement.

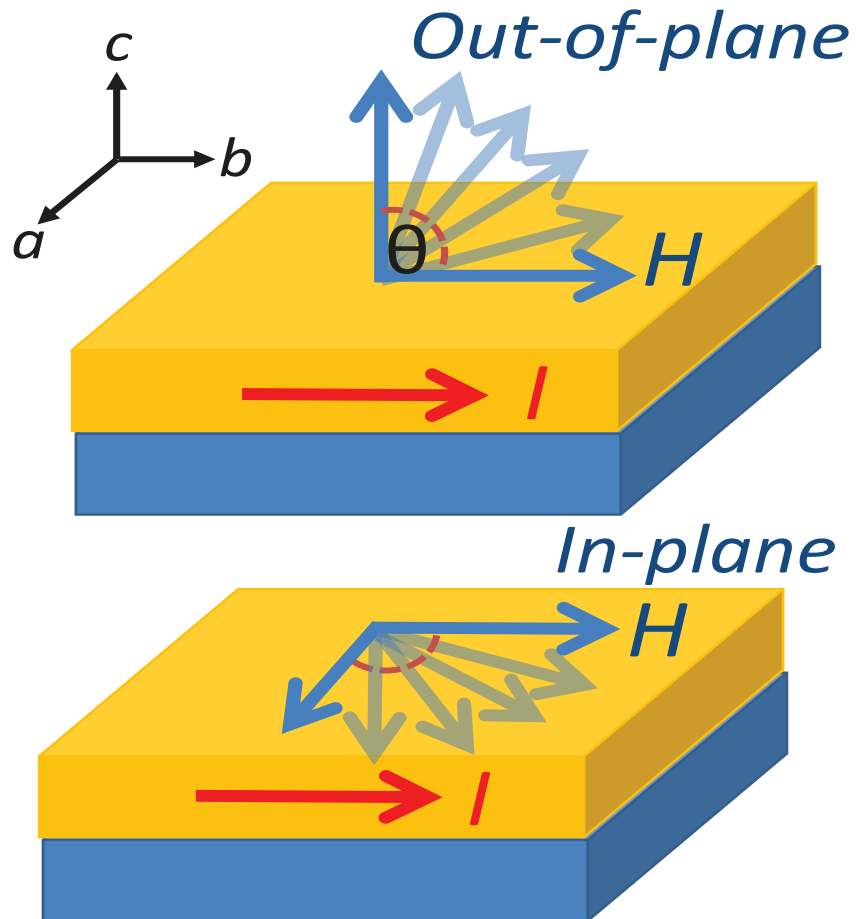


Figure 3.7: Schematic representation of the out-of plane and the in-plane anisotropic magnetoresistance measurements of a thin film sample. The angle, θ between the magnetic field \mathbf{H} and transport current \mathbf{I} is indicated in the figures.

CHAPTER 4

Correlation between charge localization and anisotropic magneto-resistance in $\text{La}_{1-x}\text{Pr}_x\text{Ca}_{0.3}\text{MnO}_3$ films

4.1 Introduction

The subtle balance between the competing electronic phases has a unique effect on the properties of manganites. One such property is the anisotropic magneto-resistance (AMR). The AMR of manganite thin films of composition $\text{RE}_{1-x}\text{AE}_x\text{MnO}_3$ (where RE and AE are the rare earth and alkaline earth elements, respectively) exhibits an unusual temperature dependence with a large maximum in the vicinity of the metal-insulator transition (MIT) and the Curie temperature (T_C), in sharp contrast with the AMR in ferromagnetic metals whose temperature dependence does not exhibit a peak.[5, 41, 60]

The origin of AMR in manganites is still not entirely clear. It is believed that the AMR is an intrinsic property of manganites, which stems from the spin-orbital and magneto-elastic couplings. Strong correlations between spin, charge, and orbital degrees of freedom, spin-orbit coupling (SO), crystal-field, and exchange-field splitting appear to influence the AMR in manganites, which is especially evident in the vicinity of ferromagnetic metallic (FM)-paramagnetic insulator (PI) transition temperature (T_{MIT}).[\[40, 61, 62\]](#) Many internal and external factors, such as orbital deformations controlled by the epitaxial strain,[\[6\]](#) inhomogeneity near the phase boundaries,[\[8, 9, 63\]](#) direction of the transport current with respect to the crystalline axes,[\[46\]](#) and magnetic field direction and strength[\[64, 65\]](#) affect the behavior of the AMR in manganite thin films. A recent work[\[66\]](#) has suggested that the broken symmetry, through distortions in the crystal lattice structure, leads to a large anisotropic magneto-elastic response to an external magnetic field and consequently to a large AMR.

A recent study[\[7\]](#) revealed that the magnitude of the out-of-plane AMR depends strongly on the local lattice distortion which could be enlarged by decreasing the average ionic radius $\langle r_A \rangle$ and consequently the cationic size mismatch σ^2 of the RE and AE ions on the A site in the perovskite lattice of $\text{RE}_{1-x}\text{AE}_x\text{MnO}_3$ manganites. Specifically, the substitution of smaller Sm^{3+} cations for the larger Nd^{3+} cations in $\text{Nd}_{0.55-x}\text{Sm}_x\text{Sr}_{0.45}\text{MnO}_3$ ($0.00 \leq x \leq 0.45$) oriented 300 nm thick polycrystalline thin films grown on LaAlO_3 substrate causes $\langle r_A \rangle$ to decrease and Jahn-Teller distortions of the MnO_6 octahedra to increase with an increasing x . This causes stronger charge carrier

localization as evidenced by the increase in the activation energy E_a of small polaron hopping with an increasing x . The data obtained on these films have shown a gradual exponential-like increase of the AMR with an increasing E_a .

These studies raises several intriguing questions: Is this relationship universal, i.e. the same for epitaxial films of other manganite systems that are subjected to A-site doping? What is the effect of the lattice strain and its sign (tensile and compressive) in the film on the carrier localization and the AMR vs E_a dependence? Is the knowledge of the value of E_a in the paramagnetic state of a film sufficient to accurately predict its AMR_{max} value? Addressing these issues is very important from the point of view of understanding the origin of the AMR as well as applications that may require manipulation of the magnitude of the AMR in thin films.

In this chapter, we present the anisotropic magneto-resistance of manganite thin films of $\text{La}_{0.7-x}\text{Pr}_x\text{Ca}_{0.3}\text{MnO}_3$ ($0.00 \leq x \leq 0.35$) and its relation to E_a . The charge localization in these films was controlled by varying x (the concentration of Pr on the A-site), the thickness of the film (the magnitude of the lattice strain), and the substrate type (the sign of the lattice strain).

The studies were performed on the following groups of samples. The dependence on x was investigated only in $\text{La}_{0.7-x}\text{Pr}_x\text{Ca}_{0.3}\text{MnO}_3$ ($0.00 \leq x \leq 0.35$) (LPCMO) films with a thickness of 44 nm. The dependence on the thickness of the film (within the range of 10 - 300 nm) was studied in LPCMO films for two compositions; $x = 0$ and $x = 0.35$. LPCMO films were deposited on SrTiO_3 (STO) and LaAlO_3 (LAO) substrates allowing us to compare and ana-

lyze the doping, thickness/strain and sign of lattice strain on the AMR versus carrier localization relation.

4.2 Experimental details

Epitaxial thin films of LPCMO were deposited with an off-axis dc magnetron sputtering (using 50 W power and an argon-oxygen mixture of partial pressures: 20 mTorr and 100 mTorr, respectively) on (001) oriented STO and LAO substrates at a temperature of 750°C. After deposition, the chamber was filled with oxygen at atmospheric pressure in order to ensure that the samples gained the optimum amount of oxygen. The films were then cooled to 650 °C with a rate of 10 °C/min, followed by annealing at 650 °C for 3 hours and subsequent cooling down to room temperature with a rate of about 15 °C/min. Room temperature x-ray diffraction confirmed that the films are single phase. We measured the c-axis lattice constants for all the films and calculated the corresponding c-axis lattice strain across the thickness of the films defined as $\epsilon_z = (100\%)(c_{film} - c_{bulk})/c_{bulk}$, where c_{film} and c_{bulk} are c-axis lattice constants of the film and the bulk sample, respectively.

The temperature dependence of resistivity, $\rho(T)$, was measured in a zero magnetic field during warming cycle over a temperature range between 10 and 350 K (in 2 K steps) using the standard four point probe technique after the sample was cooled down from 300 K to 10 K. The AMR was measured over a temperature range of 10 - 300 K, according to the following procedure; the sample was first cooled in a zero field from 300 K to 10 K, then a magnetic

field of 1.1 T was applied at 10 K in a direction either parallel to the current or perpendicular to both the current and the film. This was followed by the measurement of resistivity during warming from 10 K to 300 K. The out-of-plane AMR in percent was calculated from the formula $(100 \times (\rho_{\parallel} - \rho_{\perp}) / \rho_{avg})$, where ρ_{\perp} is the resistivity measured with the 1.1 T magnetic field perpendicular to the current direction and to the film plane, ρ_{\parallel} is the resistivity measured with the field parallel to the current direction, and $\rho_{avg} = \rho_{\parallel}/3 + 2\rho_{\perp}/3$.

4.3 Results and discussion

The measurements of $\rho(T)$ revealed that all films have a metal-insulator transition which decreases with increasing x or decreasing thickness of the film. The temperature dependence of resistivity in the paramagnetic regime above T_{MIT} has been used to calculate the activation energy E_a of small polaron hopping. At temperatures above T_{MIT} , a linear dependence is obtained between $\ln(\rho/T)$ and $1/T$ for all the samples studied, strongly supporting the Emin-Holstein adiabatic small-polaron conduction model, [7, 67, 68, 69, 70] i.e. $\rho(T) = bT \exp(E_a/2k_B T)$, where k_B is the Boltzmann constant, E_a is the activation energy ($E_a \approx E_p/2$, where E_p is the polaron binding energy), and $b = 2k_B/(3na^2e^2\nu)$ is a constant that depends on charge concentration n , longitudinal optical frequency ν , hopping distance a , and electron charge e .

The activation energy E_a was calculated for each film by fitting the $\rho(T)$ data in the paramagnetic state (see Fig. 4.1 (a)) to the above equation. Figure 4.2 (a) shows that E_a increases with the Pr concentration x for 44 nm thick

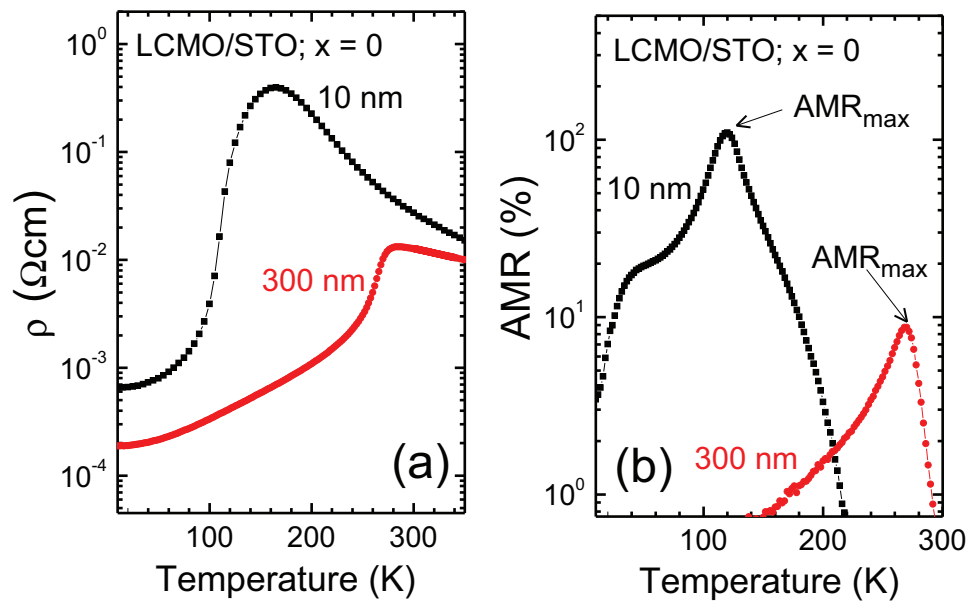


Figure 4.1: (a) Typical temperature dependence of resistivity of selected LCMO/STO ($x = 0$) films, and (b) the corresponding temperature dependence of the AMR.

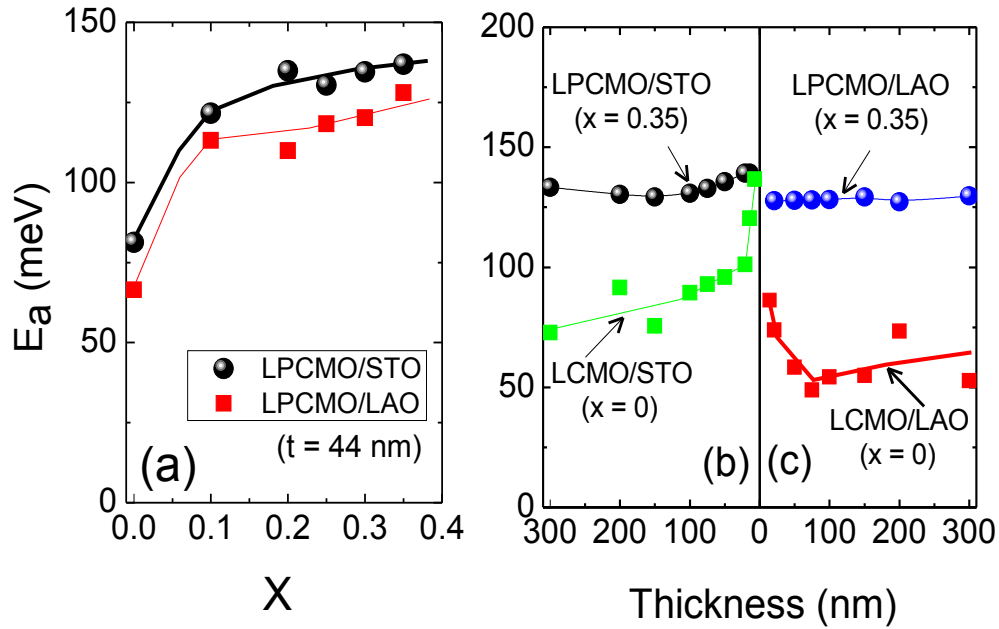


Figure 4.2: (a) Dependence of the activation energy E_a on the concentration x of Pr in $\text{La}_{0.7-x}\text{Pr}_x\text{Ca}_{0.3}\text{MnO}_3$ ($0.00 \leq x \leq 0.35$) films (44 nm thick) deposited on LAO and STO substrates. (b) and (c) Thickness dependence of E_a for LCMO ($x = 0$) and LPCMO ($x = 0.35$) films deposited on LAO and STO substrates.

films of LPCMO ($x = 0 - 0.35$). Furthermore, Figs. 4.2 (b) and (c) present the dependence of E_a on the film thickness for LCMO ($x = 0$) and LPCMO ($x = 0.35$). For LCMO E_a clearly increases with a decreasing film thickness in this range. Substitution of the smaller Pr^{3+} cation for the larger La^{3+} in LPCMO ($x = 0.35$) results in a large increase of E_a but reduces its dependence on the film thickness. These observations imply that the lattice strain as well as the Pr (A-site) doping have a profound effect on the localization of charge carriers in these films.

All films exhibit sizable AMR peaks in the vicinity of their metal-insulator transition temperatures. Figure 4.3 shows the dependence of the AMR_{max} (the magnitude of the AMR at the maximum; see Figure 4.1) on x and film thickness for tensile and compressively strained LPCMO thin films, deposited on STO and LAO substrates, respectively. The AMR_{max} in LPCMO/STO films increases with an increasing x or film thickness. At large x and small thicknesses this AMR_{max} is significantly larger than the corresponding AMR_{max} measured in LPCMO/LAO films. It is also much larger than the AMR_{max} in LCMO films. Similarly, very thin LCMO/STO films exhibit much higher AMR_{max} than LCMO/LAO ones. However, the dependence of the AMR_{max} on strain ϵ_z (see Figure 4.3 (d) and (e)) implies that there is no universal relationship between these two quantities for all the films studied. Therefore ϵ_z cannot be used as a tunable parameter to predict the value of the AMR_{max} .

By contrast, note the dependence of the AMR_{max} on E_a is shown in Figure 4.4 for all films. Figure 4.4 (a) presents this dependence for 44 nm thick LPCMO/STO and LPCMO/LAO films, obtained for different concentrations

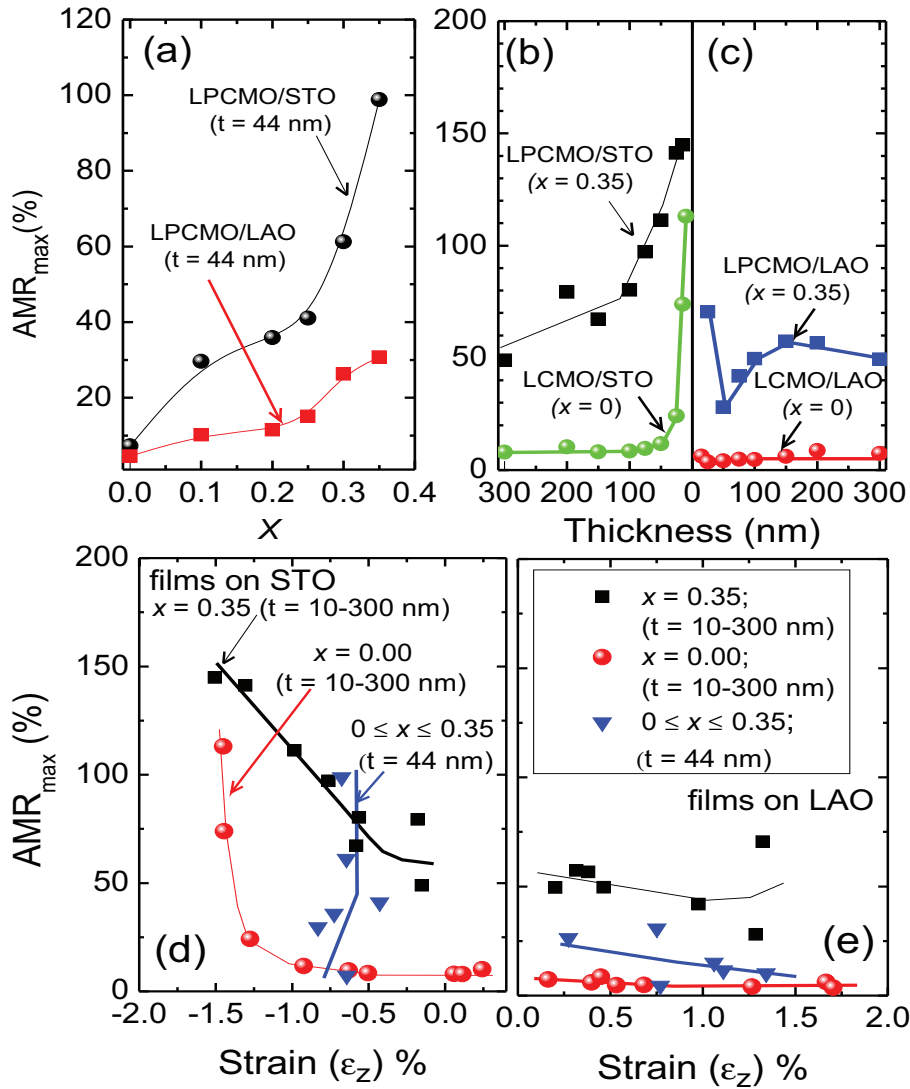


Figure 4.3: (a) Dependence of the AMR_{max} (AMR at the maximum) on the concentration x of Pr in $La_{0.7-x}Pr_xCa_{0.3}MnO_3$ ($0.00 \leq x \leq 0.35$) films (44 nm thick) deposited on LAO and STO substrates. (b) and (c) Thickness dependence of the AMR_{max} for LCMO ($x = 0$) and LPCMO ($x = 0.35$) films deposited on LAO and STO substrates. (d) and (e) Dependence of the AMR_{max} on strain ϵ_z for all films studied.

x of Pr in the LPCMO lattice. The AMR_{max} gradually increases with an increasing E_a . The trend is similar to that seen for 300 nm thick NSSMO/LAO films (see [7]), where the dependence of the AMR_{max} on E_a is plotted for different concentrations x of Sm on the A-site in the NSSMO lattice. The data for LPCMO/STO and LPCMO/LAO films lie on the same curve with the AMR_{max} in LPCMO/STO films reaching higher values.

Figures 4.4 (b) and 4.4 (c) show the data compiled for all the LPCMO/STO and LPCMO/LAO films studied, and for all strain and doping levels. The dependence of the AMR_{max} on E_a shows two distinct regimes. For values of E_a roughly below 125-130 meV the AMR_{max} increases slowly with an increasing E_a . For E_a higher than 130 meV the AMR_{max} increases dramatically. The dependence of the AMR_{max} on E_a obtained for the LPCMO/STO and LPCMO/LAO films exhibits a similar trend. Interestingly, the points corresponding to samples with different film thicknesses (magnitude of the epitaxial strain), and strain signs (STO and LAO substrates), appear to lie on a “universal” curve of AMR_{max} versus E_a . This implies, perhaps surprisingly, that knowledge of the value of E_a in the paramagnetic state of a film is sufficient to accurately predict its AMR_{max} value, irrespective of how this particular value of E_a is achieved. This potentially introduces a highly “tunable” parameter for an important magneto-transport property of the manganite film.

In the following section, we discuss possible mechanisms for our observations. In order to understand the thickness dependence of the activation energy E_a for LCMO films, shown in Figure 4.2, one has to consider the role of strain, due to the lattice mismatch between the film and the substrate. It is known[71]

that strain induced compression or the elongation of MnO_6 octahedra results in a crystal field splitting of the e_g levels by lowering either $3z^2-r^2$ or the x^2-y^2 orbital energy in the pseudocubic structure. The strain due to the film-substrate mismatch enhances the Jahn-Teller distortions and increases the tendency of electrons to become more localized.[71] This raises the polaron activation energy as the film thickness decreases.[72] For LCMO films thinner than 100 nm, the lattice strain is enhanced gradually, resulting in a gradual increase of the activation energy. Similar relationship between the strain and the activation energy has been previously reported in $\text{La}_{0.67}\text{Ca}_{0.33}\text{MnO}_3$ 40 - 500 nm thick films deposited on (110) oriented NdGaO_3 substrates.[73] An increase of the activation energy observed here for 200 nm thick LCMO films, could be caused by lattice defects which form during strain relaxation in films of thickness above the critical value. These defects enhance the JT distortions, the carrier localization and E_a . [72] The large difference between the magnitudes of the activation energies measured in LCMO/STO and LCMO/LAO films at small thicknesses suggests that E_a depends on the strain sign. Tensile strain (LCMO films on STO substrates) leads to a stronger charge localization than the compressive one (LCMO films on LAO substrates).[74]

Fig. 4.2 shows that there is an increase of E_a with decreasing thickness in both our compressive and tensile strained films of $\text{La}_{0.7}\text{Ca}_{0.3}\text{MnO}_3$ (LCMO, $x=0$). However, this doesn't seem to be the case for some other systems, such as $\text{La}_{0.9}\text{Sr}_{0.1}\text{MnO}_3$ (LSMO) films, where the opposite dependence of E_a on thickness has been reported.[69] This difference may be due to the co-existence of a number of magnetic phases[75] which are quite different from

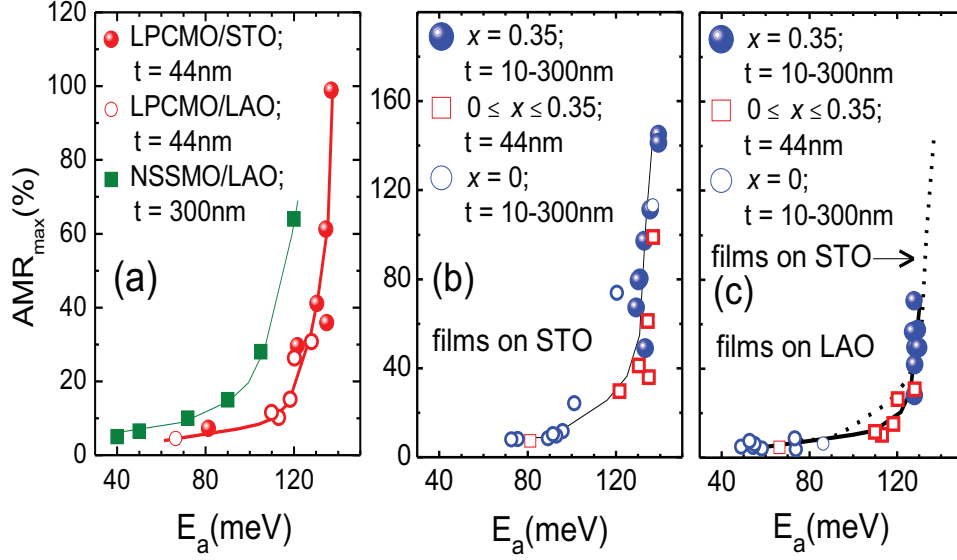


Figure 4.4: (a) Dependence of the AMR_{max} on the activation energy E_a for 44 nm thick films of LPCMO (where the concentration of Pr x varies between 0 and 0.35) deposited on STO and LAO substrates. These data are compared with those obtained for 300 nm thick films NSSMO deposited on LAO substrates. For the NSSMO films the data are plotted versus x , the concentration of Sm on the A-site. (b) and (c) Dependence of the AMR_{max} on E_a for all LPCMO films studied. The data were obtained for LCMO ($x = 0$) and LPCMO ($x = 0.35$) films of thickness t between 10 and 300 nm, and for 44 nm thick films of LPCMO (of compositions $x = 0 - 0.35$).

those in LCMO films.

In LPCMO films doping with Pr (increase of x) causes the average ionic radius $\langle r_A \rangle$ to decrease and consequently E_a to increase, but interestingly E_a becomes less sensitive to changes in the thickness of the film. E_a in LPCMO is generally larger than that in LCMO at higher thicknesses. This implies that at these thicknesses, the doping effect due to Pr is more effective in controlling E_a than the effects due to changing thicknesses.

The presence of a maximum in the temperature dependence of the AMR observed in the vicinity of T_{MIT} has been attributed to the distinct lattice response to an external magnetic field due to anisotropic Jahn-Teller (JT) distortions.[66] JT distortions modify the Mn-O-Mn bond angle, the conduction bandwidth, and the spin orbit coupling. Enhanced JT distortions caused by an increase in the epitaxial strain,[76] for example, may favor the growth of carrier localization resulting in stronger SO coupling and enhancement of the AMR.

In order to explain a sharp increase of the AMR_{max} with an increasing E_a (see Figure 4.4 (a)) observed in doped LPCMO films, we refer to the mechanism previously reported in [77]. The change in doping concentration x affects the coupling between the itinerant e_g electrons and the t_{2g} local spins. Increase of lattice distortions with an increasing x results in an enhancement of the spin-orbit coupling. In addition, non-uniformity caused by doping enhances the spin-dependent scattering of conduction electrons. Both effects lead to an increase of the AMR. Furthermore, within this model, doped films are

expected to have higher AMR than undoped ones. The AMR versus E_a curve for LPCMO films is shifted relative to that for NSSMO/LAO films, previously reported in Ref. 15, to higher values of E_a . This could be attributed to smaller values of $\langle r_A \rangle$ in LPCMO films ($\langle r_A \rangle \simeq 0.121$ nm at $x = 0$) compared to those that characterize NSSMO samples ($\langle r_A \rangle \simeq 0.135$ nm at $x = 0$).

Figures 4.4 (b) and 4.4 (c) show the dependence of AMR_{max} on E_a for LPCMO ($0.00 \leq x \leq 0.35$) films deposited on STO and LAO substrates. These films are subjected to tensile and compressive epitaxial strains, respectively. As pointed out earlier, the dependence of the AMR_{max} on E_a is very similar in both cases. However, when the LPCMO films are deposited on LAO substrates, the magnitudes of E_a and consequently AMR_{max} do not reach values as high as those measured in the LPCMO/STO films. This was observed for all LPCMO films studied (in which E_a was raised by increasing the doping or by decreasing the film thickness). This cannot be attributed to a magnitude of the strain, since the range of values of ϵ_z is similar in the thinnest LPCMO/STO and LPCMO/LAO films, as shown in Figure 4.3 (d) and (e). Therefore, the sign of the strain is a dominating factor, i.e. the tensile strain (LPCMO on STO) leads to a stronger charge localization and consequently to a larger E_a than the compressive one (LPCMO on LAO).[74]

4.4 Conclusions

In summary, we have shown that a universal correlation exists between the AMR and carrier localization effect in manganite films. A rise of the carrier

localization is reflected by the increase in the activation energy E_a of small polaron hopping. The relationship between the AMR_{max} and E_a was found to be independent of the type (magnitude and sign) of the epitaxial lattice strain and doping concentration x on the A-site. This implies that knowledge of the value of E_a measured in a film could be potentially sufficient to accurately “tune” its AMR_{max} value.

CHAPTER 5

Crossover of anisotropic magneto-resistance in phase separated $\text{La}_{1-x}\text{Pr}_x\text{Ca}_{0.3}\text{MnO}_3$ thin films

5.1 Introduction

By controlling the orbital occupation via epitaxial strain and chemical doping, the AMR in manganite thin films is greatly enhanced in the vicinity of the ferromagnetic metallic (FM)-paramagnetic insulating (PI) transition temperature (T_{MI}). This is one of the interesting observation that we have reported in the previous chapter. At low temperatures, different qualitative features of the AMR behavior have also been observed for certain type of strained manganite films. In particular, temperature dependence of the AMR for compressively strained films shows a cross-over, i.e. the AMR sign transformation from $\sin^2(\theta)$ to $\cos^2(\theta)$ as temperature is reduced well below the T_{MI} . However, this is not the case for tensile strained films which show $\sin^2(\theta)$ dependence at

the same temperatures and magnetic fields.

It is well documented that manganite thin films subjected to compressive and tensile epitaxial strain have different magnetic anisotropy at low temperatures.[78, 79, 80] For instance, low temperature magnetization measurements of $\text{La}_{0.7}\text{Sr}_{0.3}\text{MnO}_3$ and $\text{La}_{0.7}\text{Ca}_{0.3}\text{MnO}_3$ thin films exposed to tensile and compressive strain at the film/substrate interface favors in-plane and out-of-plane magnetization, respectively. The presence of such different strong anisotropy has been linked to the sign difference (corresponding to the $\theta = 90^\circ$ shift in the angular dependence of the resistivity $\rho(\theta)$) in the AMR for tensile and compressive strained films at low temperatures.[81]

In manganites, inhomogeneity driven by chemical doping near the phase boundaries is of essential importance for the AMR. An increased magnetization enhances the spin polarization leading to an increased AMR, but it also suppresses the phase inhomogeneity, thus reducing the spin-dependent scattering or the AMR.

These important observations in the AMR raise a number of questions. How is the crossover between the $\sin^2(\theta)$ and the $\cos^2(\theta)$ dependence affected by chemical doping driven inhomogeneity? What is the relationship between this crossover and the maximum in the temperature dependence of the AMR near T_{MI} ? These questions are important from the point of view of understanding of the anisotropic magneto-transport properties of manganite thin films and their potential use in applications.

In order to address these problems we studied the AMR and its temperature

dependence as a function of Pr doping in 45 nm thick $\text{La}_{0.7-x}\text{Pr}_x\text{Ca}_{0.3}\text{MnO}_3$ (LPCMO) epitaxial films deposited on STO and LAO substrates. Controlled Pr doping of LCMO allows one to change lattice distortions gradually and subsequently many of its properties, such as resistivity, T_{MI} , magneto-resistance (MR) and the AMR. As previously suggested, magneto-transport properties of manganite thin films are very sensitive to lattice distortions driven by chemical doping.[7]

5.2 Experimental details

LPCMO films of a fixed doping level x were deposited simultaneously on (001) oriented LAO and STO substrates by an off-axis dc magnetron sputtering at 750 °C in an oxygen-argon mixture. Parameters, such as base pressure (3.5×10^{-7} Torr), deposition power (50 W), deposition pressure of 120 mTorr (100 mTorr of O_2 and 20 mTorr of Ar partial pressures) and the target-substrate distance 5-cm were kept the same for all compositions. After the deposition, the chamber was filled with oxygen at atmospheric pressure in order to ensure that samples received the optimum oxygen content. The films were then cooled from 750 °C to 650 °C with a rate of 10 °C/min, followed by annealing at 650 °C for 3 hours and subsequent cooling to room temperature with a rate of about 15 °C/min. The structural characterization was performed by X-ray diffraction (XRD) at room temperature. It was used to determine the c -axis epitaxial strain ε_z for all the films.

The resistivity ρ and its dependence on temperature and angle θ between

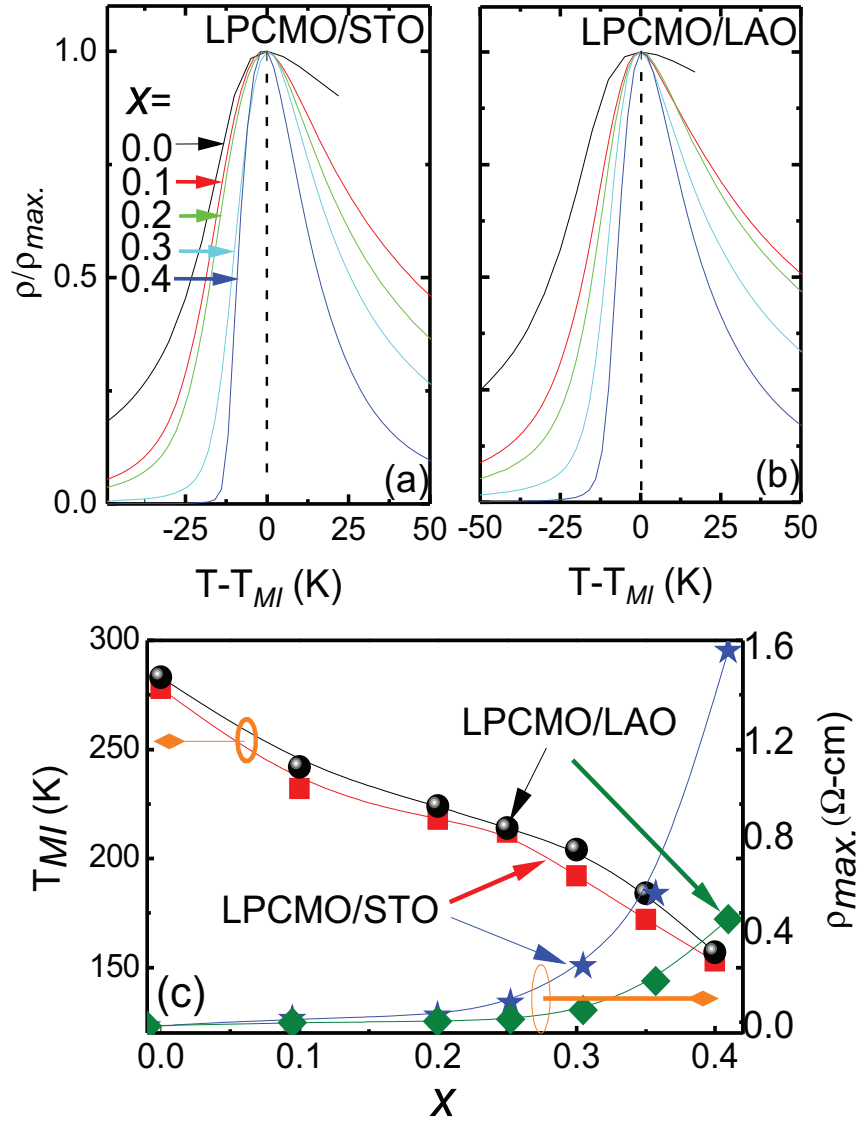


Figure 5.1: Normalized resistivity, $\rho(T)/\rho_{max}$ at a zero field, plotted for selected $\text{La}_{0.7-x}\text{Pr}_x\text{Ca}_{0.3}\text{MnO}_3$ films for $0 \leq x \leq 0.40$ deposited on (a) STO and (b) LAO substrates, respectively. The data shown were taken during warming. (c) The maximum resistivity (ρ_{max}) and corresponding metal-insulator transition temperatures, T_{MI} as a function of doping concentration, x .

the direction of magnetic field \mathbf{H} and that of the current \mathbf{J} (see the inset in Figure 5.2 (a)) were measured with the standard four probe technique using $1\mu\text{A}$ current pulses over a temperature range between 10 and 300 K. Before these measurements the samples were cooled in a zero field from 300 K to 10 K. The $\rho(T)$ was measured during warming from 10 to 300 K. The data are plotted as a function of x in Figs. 5.1 (a) and 5.1 (b).

The measurements of $\rho(\theta)$ were performed using the following procedure: After cooling down to 10 K, magnetic field \mathbf{H} of magnitude 1.1 T was applied parallel to \mathbf{J} (which corresponds to $\theta = 0^\circ$) and subsequently magnetic field has been rotated towards the c-axis direction of the films (where $\theta = 90^\circ$; see the inset in Fig. 5.2 (a)). This measurement allowed us to determine the out-of-plane component of the AMR. $\text{AMR} = (\rho_{\parallel}^{\text{in}} - \rho_{\perp}^{\text{out}}) / \rho_{av}$, where $\rho_{\parallel}^{\text{in}}$ is the resistivity of the film when magnetic field \mathbf{H} is applied in the plane of the film in the direction parallel to the current \mathbf{J} , and $\rho_{\perp}^{\text{out}}$ is the resistivity measured when \mathbf{H} is perpendicular to both the film's plane and the direction of \mathbf{J} . The average resistivity is defined as $\rho_{av} = (1/3)\rho_{\parallel}^{\text{in}} + (2/3)\rho_{\perp}^{\text{out}}$. The AMR was measured over a temperature range of 10-300 K, according to the following procedure; the sample was first cooled down in a zero field from 300 K to 10 K, then a magnetic field of 1.1 T was applied at 10 K in a direction either parallel to the current or perpendicular to both the current and the film. This was followed by the measurement of the resistivity during warming from 10 K to 300 K.

5.3 Results and discussion

Figures 5.1 (a) and 5.1 (b) show the normalized resistivity $\rho(T)/\rho_{max}$ of doped LPCMO films deposited on STO and LAO substrates, respectively. Regardless of the type of the substrate used, the width of the resistivity peak decreases gradually with an increasing doping level x . Reduction of T_{MI} and an increase of the peak resistivity with an increasing concentration of Pr (see Fig. 5.1 (c)) are due to the reduction of the average ionic radius $\langle r_A \rangle$ of the A-site cations. The LPCMO/STO films exhibit slightly lower T_{MI} than the LPCMO/LAO films.

Interestingly, at high Pr doping levels ρ_{max} measured at the T_{MI} in the LPCMO/STO films is higher than that measured in the LPCMO/LAO ones. This could be due to the different strain states that these films experience, which modify the orbital states and consequently the magneto-transport properties of these samples. [82, 83, 84]

The temperature dependence of the AMR for all films deposited on STO and LAO substrates are shown in Fig. 5.2 (a) and 5.2 (b), respectively. The AMR of all samples exhibit a peak close to the T_{MI} . At high doping levels the magnitude of these peaks (AMR_{max}) in LPCMO/STO films is much higher than those in LPCMO/LAO films. For tensile strained films (on STO), the AMR_{max} increases continuously with x , while for compressively strained films (on LAO), the AMR_{max} increases up to $x = 0.35$, and then starts to decrease at higher x .

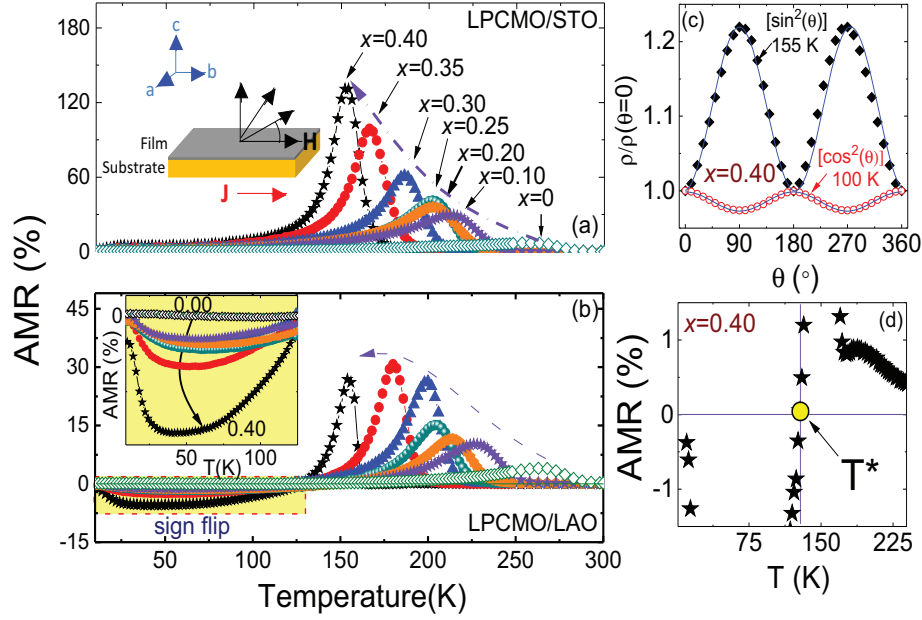


Figure 5.2: Temperature dependence of the out-of-plane magnetoresistive anisotropy, AMR measured in a field of 1.1 T at doping levels between $x=0$, and $x=0.40$ for films grown on (a) SrTiO₃ and (b) LaAlO₃ substrates. Dashed curves in both figures show the expected dependence of the AMR_{max} on doping. The change of sign of the AMR with an increasing doping is shown in the rectangular yellow area. Insets in (a) and (b) show the direction of magnetic field \mathbf{H} and the direction of the current \mathbf{J} , and the expanded view of the AMR at low temperatures for LPCMO/LAO doped films, respectively. (c) The normalized angular dependent resistivity measured at 155 K (i.e., where the AMR has a peak) and at 100 K (i.e., yellow region). The solid lines are the fits to the data (see text). (d) The crossover temperature, T^* at which the AMR sign changes from positive to negative is shown for $x=0.40$ doped film.

The most interesting behavior is observed at low temperatures well below T_{MI} , where the AMR in LPCMO/LAO films changes sign (see the inset in Fig. 5.2 (b)). The sign change in the AMR is shown for LPCMO with $x = 0.40$ in Fig. 5.2 (c) where the AMR measured at 155 K is positive (i.e., $\sin^2(\theta)$) dependence while it is negative at 100 K where it has a $\cos^2(\theta)$ dependence. The solid lines in Fig. 5.2 (c) represent the theoretical fits of $\rho(\theta)$ data to the expression $\rho(\theta) = A + [\rho_{\parallel}^{\text{in}} - \rho_{\perp}^{\text{out}}] \cos^2(\theta)$ which describes the angular dependence of resistivity on a magnetic field in ferromagnetic metals.[85]

Temperature at which the AMR changes sign is marked as the crossover temperature T^* (see Fig. 5.2 (d)). Plotting the dependence of T^* and the c -axis epitaxial strain ε_z on the doping level x (see Figure 5.3) reveals similar patterns, which implies that the epitaxial strain is partly responsible for the shift of T^* in the AMR(T) for LPCMO/LAO films.

In order to visualize better the influence of doping and temperature on the sign of the AMR in LPCMO/LAO, the AMR(x) for the LPCMO/LAO films has been compared with that for the LPCMO/STO ones at temperatures between 10 K and 200 K (see Figs. 5.4 (a)-(d)). The AMR for all LPCMO/STO films has positive values which increase with an increasing x over the whole range of temperatures. However, for LPCMO/LAO films the sign of the AMR changes to negative (i.e., the AMR becomes $\cos^2(\theta)$ like) at low temperatures below T^* . The AMR has a pronounced minimum at x around 0.2. The most negative values of the AMR have been observed at 50 K. The crossover from $\cos^2(\theta)$ to $\sin^2(\theta)$ behavior takes place at higher temperatures. Above 162 K, the values of the AMR become positive for all the films. At low temperatures,

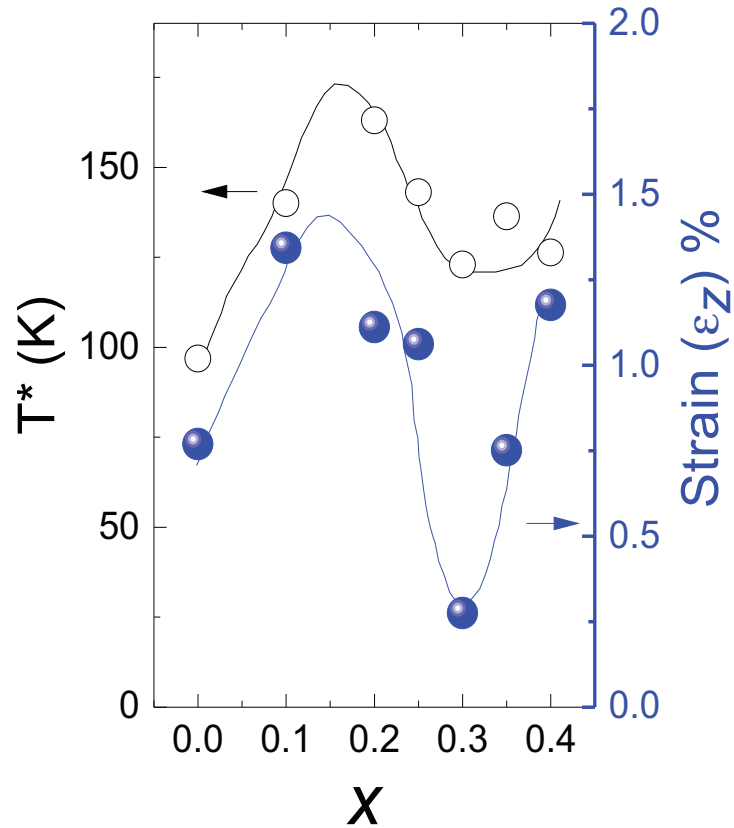


Figure 5.3: The dependence of the crossover temperature, T^* and c -axis epitaxial strain ϵ_z on doping concentration x for LPCMO/LAO thin films.

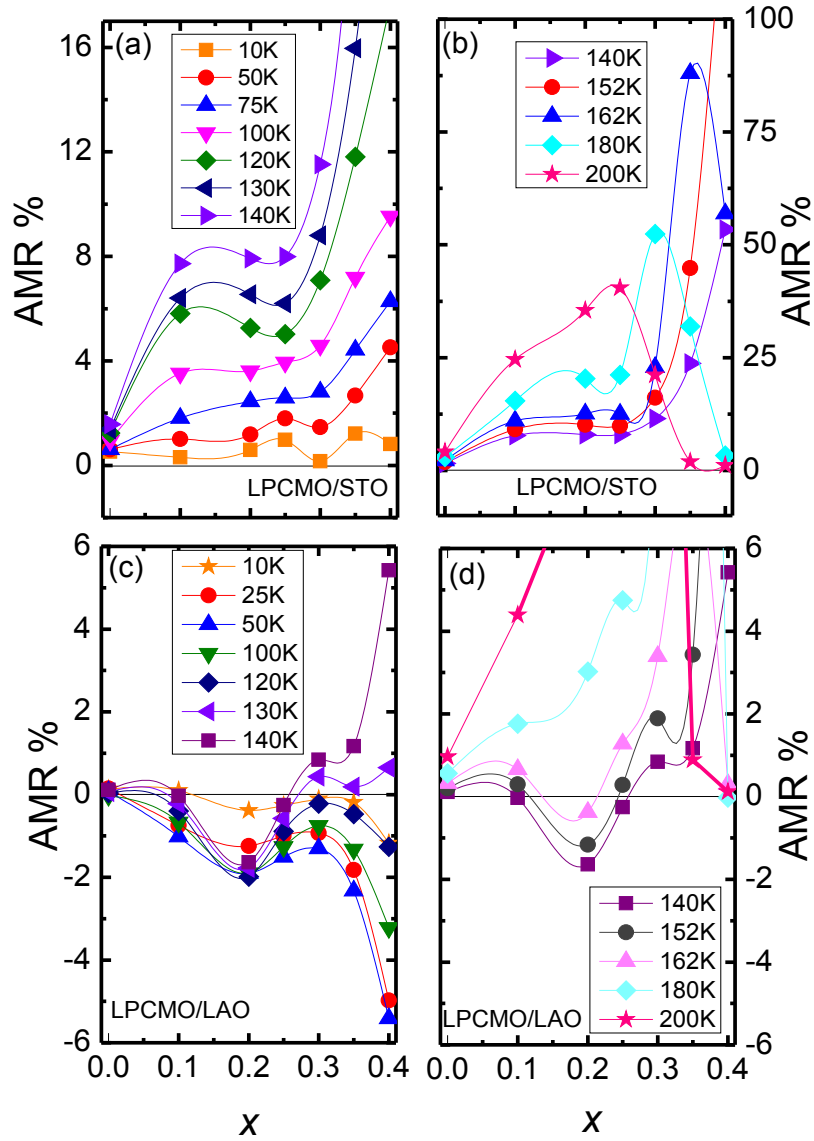


Figure 5.4: The influence of temperature and doping x on the AMR sign evolution for tensile LPCMO/STO (a - b), and compressive strained LPCMO/LAO films (c -d) collected at temperatures between 10 K - 200 K for ($0.0 \leq x \leq 0.40$).

eg. 50 K (see Fig. 5.5 (a)), the doping dependence of the AMR for compressive and tensile strained films show a clear symmetry with respect to AMR = 0 line (green solid line).

The presence of a maximum in the temperature dependence of the AMR observed in manganite films near T_{MI} has been attributed to the asymmetric Jahn-Teller (JT) distortions.[66] A system with larger JT distortions should have a higher AMR. This happens because the JT distortions modify the Mn-O-Mn bond angle and the conduction bandwidth, resulting in a stronger spin-orbit coupling. Previous studies have indicated that very large lattice distortions have been responsible for the largest maximum in the temperature dependence of the AMR observed for example, in 20-40 nm thick $\text{La}_{1-x}\text{Ca}_x\text{MnO}_3/\text{STO}$ films.[64] Smaller lattice distortions in 20-40 nm thick $\text{La}_{1-x}\text{Sr}_x\text{MnO}_3/\text{STO}$ films resulted in a smaller AMR.[64] Similar trends have been also reported for $\text{La}_{1-x}\text{Ca}_x\text{MnO}_3/\text{STO}$, $\text{Pr}_{1-x}\text{Sr}_x\text{MnO}_3/\text{STO}$ and $\text{La}_{1-x}\text{Ca}_x\text{MnO}_3/\text{STO}$ films.[58, 66, 77, 86] This behavior is consistent with that exhibited by our tensile strained LPCMO/STO films (see Fig. 5.2 (a)) where the AMR_{max} increases monotonically with an increasing x due to the decrease of the average radius of the A-site ion in LPCMO, and subsequent increase of JT distortions.

On the other hand, the situation for compressively strained LPCMO/LAO films is completely different. An increase of the AMR_{max} with an increasing x is much smaller than that observed in the LPCMO/STO films. The AMR_{max} levels off at around 30% at high dopings. In addition, at low temperatures below T^* the AMR changes sign and its magnitude increases with an increasing x .

Most of earlier studies have shown that the magnetic anisotropy in epitaxial thin films of the same composition depends on the substrate induced distortion of MnO_6 octahedron.[87, 88] For instance low temperature magnetization measurements for $\text{La}_{1-x}\text{Ca}_x\text{MnO}_3$ (LCMO) films with $x=0.30-0.33$ shows easy axis magnetization in the plane, when they are deposited on STO (compressed octahedron) and shows perpendicular (i.e., out-of-plane) magnetization for films on LAO (elongated octahedron).[89, 90, 91] According to this argument, it is reasonable to expect that the $\theta = 90^\circ$ shift between the angular dependence of the resistivity $\rho(\theta)$ measured at low temperatures (see Fig. 5.5 (a)) for films deposited on STO and LAO substrates is due to the strain induced rotation of the direction of the easy axis magnetization (see Fig. 5.5 (b) and 5.5 (c)). This argument is consistent with the results on $\text{Pr}_{0.67}\text{Sr}_{0.33}\text{MnO}_3$ and $\text{La}_{0.65}\text{Ca}_{0.35}\text{MnO}_3$ thin films, where the AMR sign is negative and positive at low temperatures for films grown under compressive and tensile stress respectively.[86]

An almost symmetric increase of both positive and negative AMR with an increasing x at 50 K (see Fig. 5.5 a) could be due to the doping driven enhancement of electronic non-uniformity which increases the spin-dependent scattering and AMR in doped manganite films according to Ref. [77].

The absence of AMR sign cross-over in tensile strained LPCMO/STO films implies that the easy-axis magnetization favors in-plane configuration regardless of the x , temperature and magnetic field.[92] This is also true for other manganite systems such as the tensile strained LSMO/STO films where the sign cross-over is absent in these films due to their strong in-plane easy-

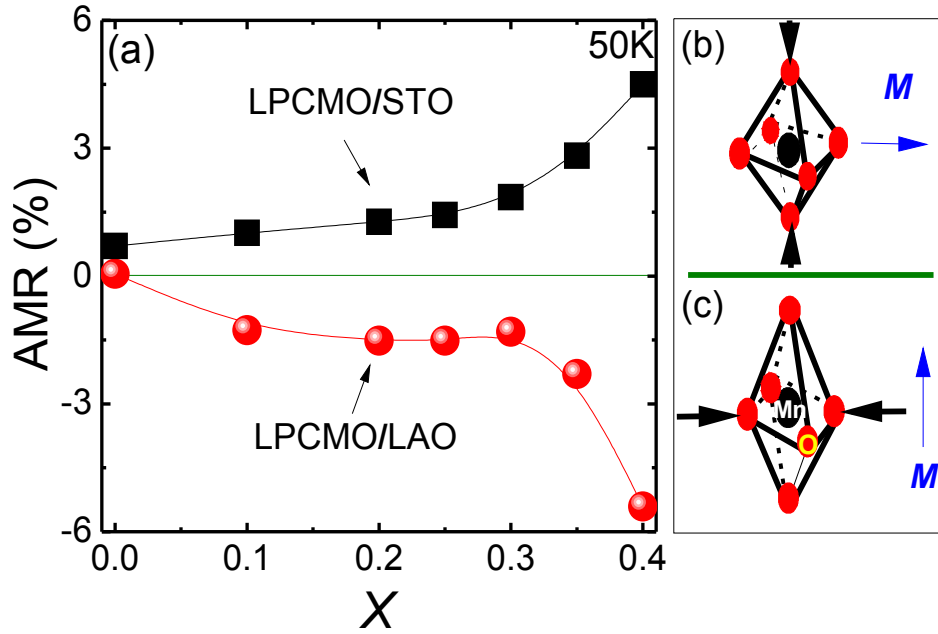


Figure 5.5: (a) The dependence of AMR on doping concentration x at 50 K for LPCMO/STO and LPCMO/LAO films. The Jahn-Teller distortion of MnO₆ octahedron under tensile and compressive strain are shown in (b) and (c) respectively. The black arrows show the stress axis and the blue arrow shows the corresponding direction of the easy-axis magnetization.

magnetization.[93]

Figure 5.6 shows the temperature dependent magnetization measured at a magnetic field of 1.1 T applied parallel and perpendicular to the (100) crystallographic direction for LPCMO ($x=0.40$) films deposited on LAO and STO substrates, respectively. For LPCMO/LAO film, magnetization for H perpendicular to (100) is higher than the magnetization measured for H parallel to (100) below the cross over temperature of $T^*=100$ K. However, magnetization for H parallel to (100) is higher than the magnetization for H perpendicular to (100) for the whole range of temperature in LPCMO/STO film. The magnetization measurements clearly indicate that the sign of the epitaxial strain modifies the easy-axis magnetization in the LPCMO films.

The possible mechanism of the sign cross-over in the AMR for the compressive strained films is as follows: In manganites, the structure of MnO_6 octahedron is sensitive to the changes in temperature for certain strained films.[94] Thermally driven distortion of the octahedron could modify the direction of easy-axis magnetization which consequently changes the AMR sign as the temperature approaches T^* . Beside the temperature effects, chemical doping induced distortion of MnO_6 octahedron also modifies the easy-axis magnetization. This can be seen in Fig. 5.3 where the change in T^* roughly follows the doping driven change of the epitaxial strain in the films. According to Ref. [95], magnetostriction due to presence of Pr^{+3} could produce rotation of the easy-axes magnetization and consequently the sign change in the AMR for PSMO/LAO thin films.

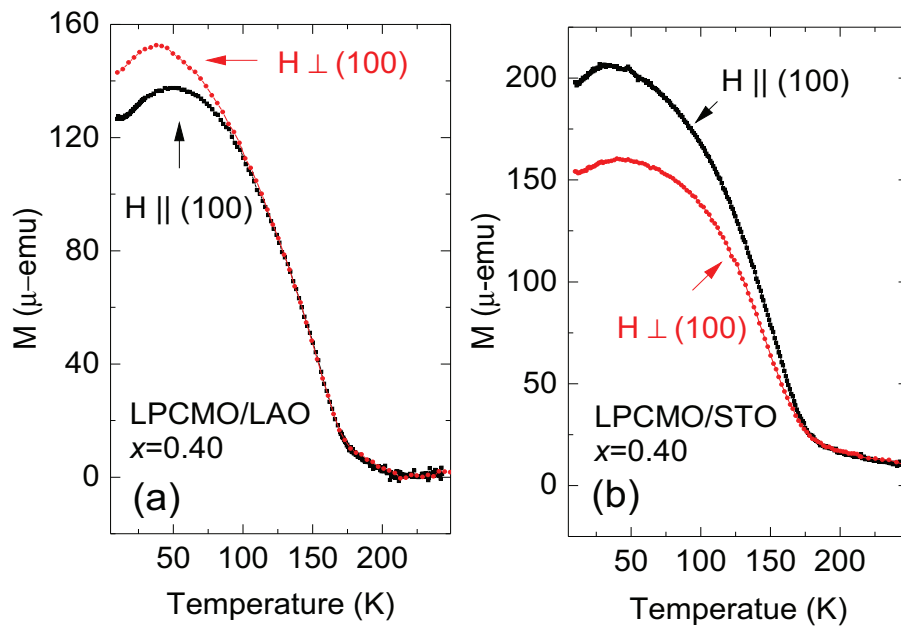


Figure 5.6: The dependence of magnetization on temperature measured in a magnetic field of 1.1 T applied parallel and perpendicular to the (100) crystallographic direction of the LPCMO ($x=0.40$) films on (a) LAO and (b) STO substrates, respectively.

As a follow up study, we suggest that the effects of thickness dependence (with a constant Pr concentration films deposited on LAO substrates) may shed further light on the AMR-crossover in LPCMO manganites. Since systematic change of film thickness as compared to Pr-doping could eliminate the complicated effects of the chemical substitution on the AMR sign.

5.4 Conclusions

In summary, we have shown that the presence of a maximum in the temperature dependence of the AMR in the vicinity of the T_{MI} increases gradually with x for tensile strained films while the change of the maximum AMR with doping much smaller for compressively strained films. We attribute this difference to the competition between JT driven enhancement of the $\sin^2(\theta)$ and $\cos^2(\theta)$ dependent AMR at the T_{MI} and low temperatures.

CHAPTER 6

Recovery of oscillatory magneto-resistance in $\text{La}_{0.3}\text{Pr}_{0.4}\text{Ca}_{0.3}\text{MnO}_3$ epitaxial thin films

6.1 Introduction

In previous chapters, we have seen the influence of carrier localization and the magnetic anisotropy on the AMR in LPCMO films. These effects are observed at low and high temperatures where the samples are predominantly ferromagnetic metallic and paramagnetic insulating phases, respectively. In this chapter, we investigate the AMR near the metal-to-insulator transition where the competing metallic and insulating phases are very sensitive to small changes in temperature and magnetic field.

Studies done over the last decade have shown that phase separated (PS) manganites have a wide range of unique properties due to the complex interplay between spin, charge, and orbital degrees of freedom, which is believed to

be responsible for the coexistence of the self-organized magnetic and electronic phases.[96] One such property is the anisotropic magneto-resistance (AMR). Strong correlations are believed to affect the spin-orbit coupling and the magnitude of the AMR.[55, 61] Large value of the AMR in PS manganite are promising for certain applications. However, the AMR phenomena and the underlying physics/mechanism of the AMR in these systems have not been fully understood. For example, recent publications [8, 9] reported unusual behavior of the AMR in manganite thin films of $\text{La}_{0.67}\text{Ca}_{0.33}\text{MnO}_3$ and $\text{Pr}_{0.7}\text{Ca}_{0.3}\text{MnO}_3$ deposited on NdGaO_3 and SrLaGaO_4 substrates, respectively. In particular, the resistance measured as a function of the angle θ between the magnetic field direction and the direction of the current in the plane of these films does not follow the standard oscillatory dependence (i.e., $\cos^2\theta$ or $\sin^2\theta$) observed in many manganite films.[64, 77, 97, 98]

Instead, the resistance decreases monotonically exponential-like with an increasing angle from a value much larger than that expected in its oscillatory state.[8, 9] This non-oscillatory dependence on θ depends strongly on an applied magnetic field, and it is very pronounced at high fields. Furthermore, the authors of these studies did not report any recovery of the oscillatory state of the resistance. They suggested only that the irreversible melting of the antiferromagnetic insulator (AFI) phase at the percolation threshold in high fields is likely responsible for this suppression of the metastable resistance.

In order to better understand the nature of this unusual behavior, we explored the angular dependence of resistivity, $\rho(\theta)$ as a function of temperature, magnetic field and time for the $\text{La}_{0.3}\text{Pr}_{0.4}\text{Ca}_{0.3}\text{MnO}_3$ (LPCMO) films

grown on (100) oriented NdGaO₃ (NGO) and (001) oriented SrTiO₃(STO) and LaAlO₃(LAO) substrates. These substrates produce epitaxial lattice strain of different magnitudes, anisotropy and signs (compressive/tensile) in the plane of the LPCMO film. NGO, STO and LAO substrates give rise to anisotropic compressive, quasi-isotropic compressive, and quasi-isotropic tensile strain, respectively.

LPCMO is a prototypical manganite which is well known for its large-scale phase separation.[11, 99] Our studies have shown that at high fields and at a temperature at which the electronic phase separation is the strongest, the system is in the metastable state with a large resistivity whose magnitude decreases with time. Furthermore, this resistivity drops monotonically with an increasing θ and does not display an oscillatory behavior. Interestingly, we discovered that the regular $\cos^2\theta/\sin^2\theta$ oscillations in $\rho(\theta)$ can be recovered by repetitive sweeping/cycling of θ between 0° to 180° in the plane of the films. These results suggest that the large metastable resistivity and the recovery of the oscillations in $\rho(\theta)$ are controlled by the magnetic field induced percolation in strongly phase-separated manganite films.

6.2 Experimental details

The 44 nm thick LPCMO epitaxial films were deposited in an off-axis dc magnetron sputter deposition system on 100 oriented NGO and 001 oriented STO and LAO substrates at a temperature of 750 °C. These films were grown in an argon-oxygen mixture of partial argon and oxygen pressures of 20 mTorr

and 100 mTorr, respectively. After the deposition, the chamber was filled with oxygen at atmospheric pressure in order to ensure the optimum oxygen content in these samples. The films were then cooled down to 650 °C with a rate of 10 °C/min, followed by annealing at 650 °C for 3 hours and subsequent cooling to room temperature with a rate of about 15 °C/min.

The resistivity ρ and its dependence on temperature, magnetic field, time and the angle θ between the directions of the magnetic field \mathbf{H} and the current \mathbf{J} (see Figure 6.1 (b)) were measured with the standard four point probe technique over a temperature range between 10 and 300 K, and in magnetic fields up to 1.1 T. The measurements were done on LPCMO films patterned to form of a 0.5 mm wide and 5 mm long bridges. Most of the measurements were carried out for the warming cycle. In this case, before the measurements of $\rho(T)$, $\rho(H)$, $\rho(t)$ and $\rho(\theta)$ the sample was cooled in a zero field from 300 K to 10 K. $\rho(T)$ was measured during warming from 10 to 300 K. The measurements of $\rho(H)$ and $\rho(\theta)$ were performed using the following procedure: At 10 K a magnetic field \mathbf{H} of magnitude 1.1 T was applied in the plane of the film at a certain angle θ relative to the direction of the current \mathbf{J} . Then the sample's temperature was increased until it reached the temperature of the measurement. $\rho(H)$ hysteresis was measured at $\theta = 0^\circ$, where \mathbf{H} is parallel to \mathbf{J} . The measurement of $\rho(\theta)$ was performed at a constant magnetic field by repetitive back and forth sweeping of θ between 0° and 180° in the plane of the film. The measurements of $\rho(t)$ and $\rho(\theta)$ were also performed during the cooling cycle. In this case the sample's temperature was first reduced from 300 K down to the temperature of the measurement in a zero field. Then a

magnetic field was applied, which was followed by the measurements of $\rho(t)$ and $\rho(\theta)$.

6.3 Results and discussion

The temperature dependence of the resistivity of the LPCMO thin films grown on NGO, STO and LAO substrates, which were measured in a zero magnetic field, is shown in Figure 6.1 (a). The LPCMO films deposited on NGO, STO and LAO substrates show the metal-insulator transition temperatures (T_{MIT}) at 140 K, 150 K and 160 K respectively.

The $\rho(H)$ curves are plotted in Figures 6.2 (a), (c) and (e) for selected temperatures between 100 and 170 K. At temperatures close to T_{MIT} , the hysteresis loops are much larger than those measured at 100 K or 170 K. Near T_{MIT} the hysteresis loops are the result of the percolative phase separated state formed by the charge ordered antiferromagnetic insulating (COI-AFI) and ferromagnetic metallic (FMM) phases.[30, 100] However, at lower and higher temperatures the area of the hysteresis loops is reduced, the phase separation is small, and the film is predominantly ferromagnetic metal at 100 K, and charge ordered insulator at 170 K.[101]

In order to compare the behavior of $\rho(\theta)$ with the size of the $\rho(H)$ hysteresis loop, we measured $\rho(\theta)$ in a field of 1.1 T at temperatures between 100 and 170 K (see Figure 6. 2 (b), (d) and (f)), starting at $\theta = 0^\circ$. At these temperatures ρ is θ dependent. At 125 K, 140 K and 155 K where the $\rho(H)$ hysteresis

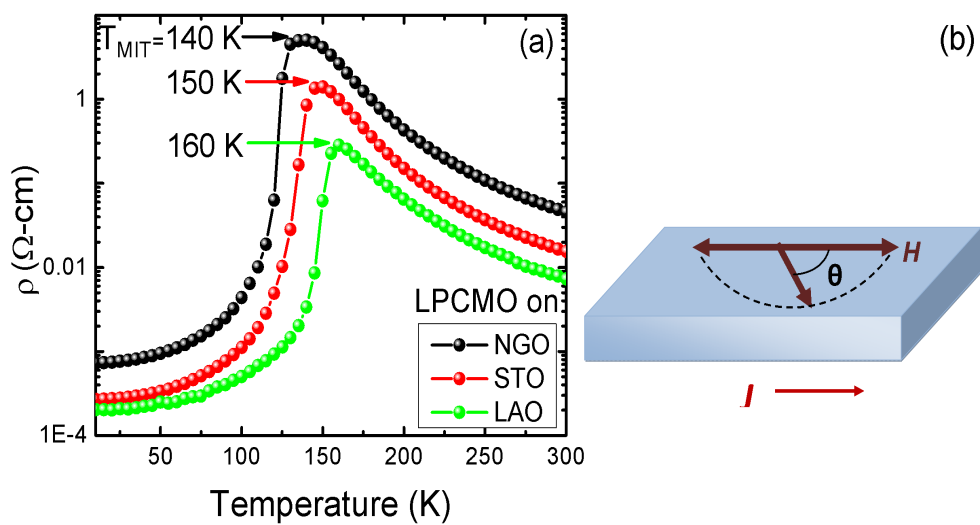


Figure 6.1: (a) Temperature dependence of resistivity of LPCMO film deposited on NGO, STO and LAO substrates in a zero magnetic field; (b) Schematic showing the direction of magnetic field \mathbf{H} and direction of the current \mathbf{J} both located in the plane of the film.

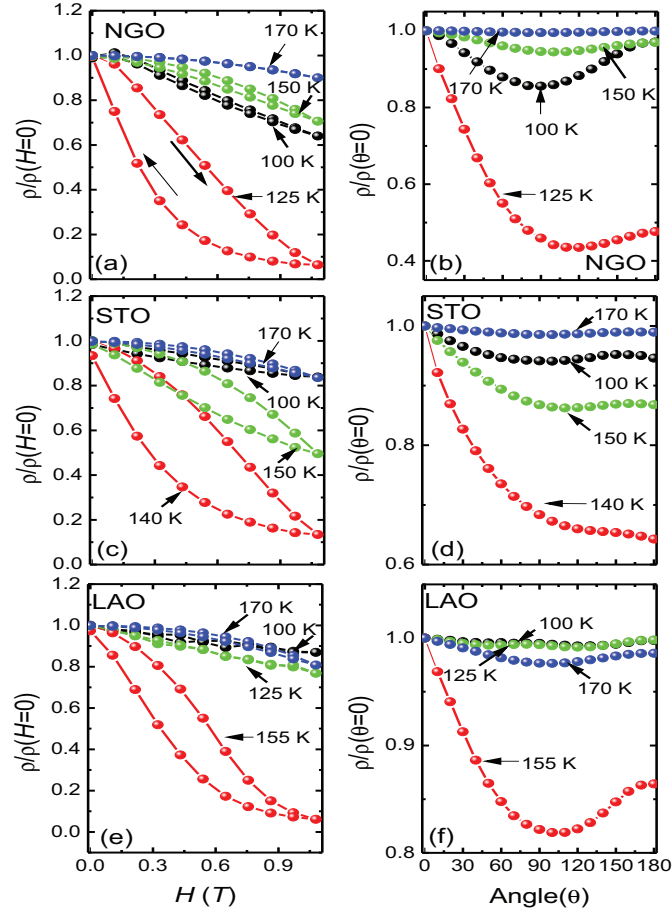


Figure 6.2: [(a), (c) and (e)] Dependence of the normalized resistivity on magnetic field measured at selected temperatures between 100 and 170 K. Magnetic field is parallel to J ($\theta = 0$). The hysteresis loop is the largest at 125 K, 140 K and 155 K for the film deposited on NGO, STO and LAO substrates, respectively. The arrows inside the loop in (a) indicate the sweeping directions of the applied magnetic field. [(b), (d) and (f)] Dependence of the normalized resistivity on the angle θ between \mathbf{H} and \mathbf{J} at a field of 1.1 T, measured at temperatures between 100 K and 170 K for films deposited on NGO, STO and LAO substrates.

loops are the largest in LPCMO films on NGO, STO and LAO substrates, respectively, $\rho(\theta)$ exhibits dramatic non-oscillatory behavior. An increase in θ causes ρ to drop by about 50%, 40% and 20% in film on NGO, STO, and LAO substrates respectively.

In order to understand better the dependence of ρ on θ at these temperatures, we carried out several back-and-forth angular scans of $\rho(\theta)$ at 1.1 T on our three films (starting at $\theta = 0^\circ$) (see Figure 6.3 (a), (b) and (c)). Oscillations are superposed on a large metastable resistivity which decreases monotonically, and significantly, with an increasing θ during the *first scan* of θ from 0° to 180° . Interestingly, we have found that the metastable resistivity could be eliminated by the subsequent back-and-forth angular scans of θ between 0° to 180° , which ultimately recovers the symmetric oscillatory behavior of $\rho(\theta)$ in all the samples.

Since time is also increasing during the angular scans shown in Fig. 6.3, it is natural to inquire whether the suppression of the metastable resistivity (and hence the apparent recovery of the oscillatory behavior) is primarily due to a time-relaxation of ρ whose decay rate reaches zero at long times. In an attempt to address this issue, we carry out the measurements summarized in Fig. 6.4. Fig. 6.4 (a), (b), and (c) show the time dependencies of ρ for LPCMO/NGO, LPCMO/STO and LPCMO/LAO films at 125 K, 140 K and 150 K, respectively in a field of 1.1 T. During the first 100 minutes, the value of θ is fixed at 0° . Clearly, the metastable ρ in all three films decreases with time during this time interval. After approximately 100 minutes, the decrease in the resistivity has slowed considerably. After this time, the resistivity was measured during

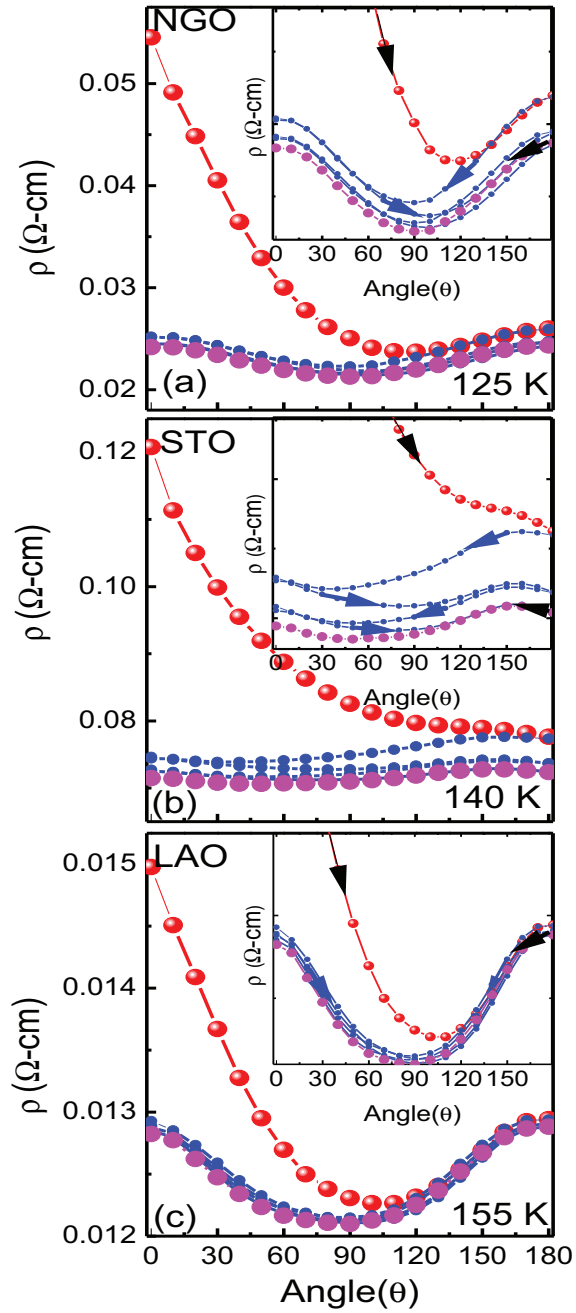


Figure 6.3: [(a), (b) and (c)] The angular repetitive sweeps of the resistivity at 125 K, 140 K and 155 K in a field of 1.1 T for films grown on NGO, STO and LAO respectively. The inset shows the expanded view of $\rho(\theta)$. Arrows indicate an increase/decrease of θ .

the back-and-forth angular scanning between 0° and 180° . Notably, the ρ of all the films still show a dramatic decrease during the first angular sweep from 0° to 180° . Subsequent sweeps between 0° and 180° produce clear oscillatory behavior centered about a nearly time-independent resistivity level.

We emphasize that although the magnitude, sign, and anisotropy of the lattice strains due to the substrate are different in the three LPCMO films, Fig. 6.3 and Fig. 6.4 show that the main qualitative features such as the time dependence of the resistivity at a fixed θ ($=0^\circ$), the “rapid drop” in the resistivity upon the first angular sweep of the magnetic field, and the subsequent “recovery” of the oscillatory resistance upon further angular sweeps, are common to all the films.

We suggest that phase competition between the FMM and COI-AFI phases [102] plays an important role in explaining our observations described above. The decrease in ρ with increasing time at a fixed angle ($\theta = 0^\circ$), shown in Fig. 6.4, indicates that the metallic state is the more “stable” state in LPCMO films (at 1.1 T). The conversion to this state occurs via the growth of the metallic domains, and at the temperatures and fields shown in Fig. 6.4, occurs on the timescale of roughly an hour.

The mechanism of the subsequent evolution of ρ with the angular sweeps is proposed to be as follows: The magnetic field applied in a particular direction parallel to the film plane causes a preferential expansion of the volume of FMM domains in that field direction. Hence, during the first angular sweep, by a continuous sweeping of the magnetic field direction in the film plane, the

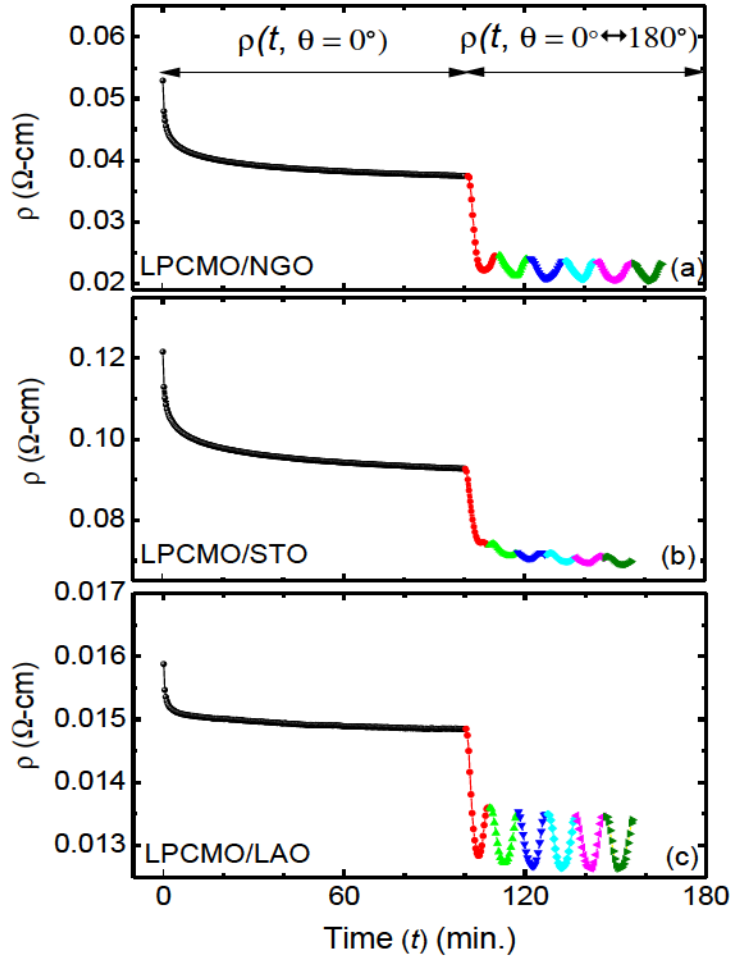


Figure 6.4: [(a), (b) and (c)] Dependence of the resistivity on time for the magnetic field of 1.1 T, parallel to J ($\theta = 0$) at a temperature of 125 K, 140 K and 155 K for LPCMO films grown on NGO, STO and LAO substrates, respectively. The measurement of ρ for times larger than 100 min was performed during the angular repetitive sweeps of θ between 0° and 180° .

overall volume of FMM domains is increased dramatically. This leads to an enhanced percolation within the film and a dramatic drop of the resistivity to its “oscillatory” level. The oscillations in the subsequent angular sweeps are just the regular $\cos^2\theta/\sin^2\theta$ behavior of the AMR qualitatively observed in many manganite films.[103, 104]

Our proposed mechanism for the sharp resistivity drop has been further tested by investigating the effects of thermal cycling. Since the size and shape distribution of the metallic and insulating clusters in the LPCMO films during the cooling cycle produces more pronounced electronic phase separation than during the warming cycle, [36, 105] one expects a larger resistivity drop in the former.

In order to test this hypothesis, we measured the time dependent AMR for all films during the cooling and warming cycles. We have found that the cooling cycle leads to a larger drop in resistivity as compared to the warming cycle for all of the films. This is shown in Fig. 6.5 for the LPCMO/NGO film: the normalized resistivity drop upon the first angular sweep of the magnetic field is significantly larger during the cooling cycle.

Finally, we remark that the observed resistivity drop depends on the applied magnetic field. To further investigate the magnetic field effect on the resistivity drop, we performed time dependent AMR measurements at various magnetic fields between 0.11 T and 1.1 T for all of the films. Our data revealed that the drop in resistivity increases with an increasing magnetic field, consistent with the increase of the phase separation between the COI-AFI and FMM phases

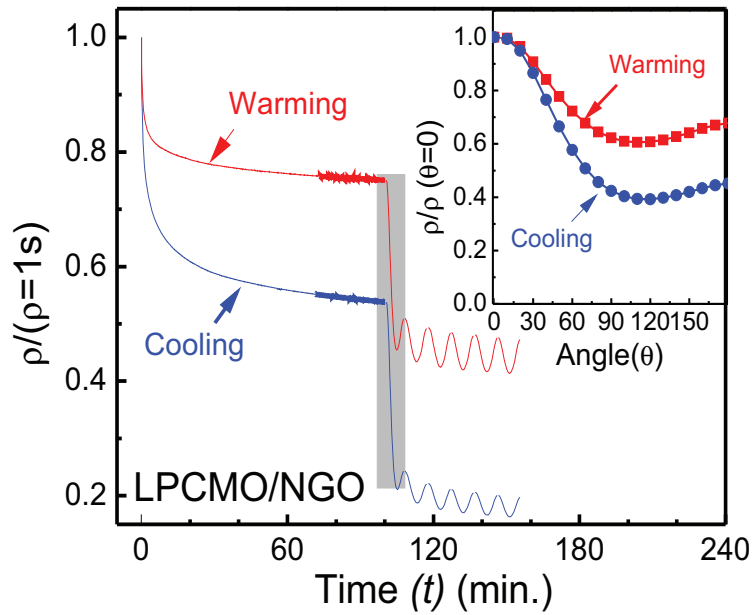


Figure 6.5: Dependence of the normalized resistivity, ρ and $\rho(\theta)$ on time for the magnetic field of 1.1 T, recorded during cooling and warming cycles at a temperature of 125 K for LPCMO/NGO film. The inset shows the normalized $\rho(\theta)$ obtained during the first angular sweep of the magnetic field. It corresponds to the time period marked by the shaded rectangular region in the main figure.

up to 1.1 T. In this experiment, 1.1 T was the maximum field that could be applied to the samples and is not high enough to produce a pure FMM phase in the LPCMO films.[106, 107] This is visible in Figures 6.2 (a), (c) and (e), wherein at 1.1 T, the resistivity has not decreased to its low-resistivity “saturation” value. Although we are unable to perform these experiments due to the limitations of our experimental setup, we anticipate that at significantly higher fields where a pure FMM state is produced in the sample, the drop in resistivity during the first angular sweep of the magnetic field will be highly suppressed.

6.4 Conclusion

We have found that the metastable irreversible non-oscillatory resistance observed in the LPCMO films at an fixed angle θ between the magnetic field and the current strongly depends on the field induced percolation in these systems. The regular oscillatory $\cos^2\theta/\sin^2\theta$ dependent resistance can be recovered by the repetitive scans of θ between 0° to 180° . These results may provide useful information regarding the control of the anisotropic magneto-resistance in manganite-film-based devices.

CHAPTER 7

Anisotropic magneto-resistance in spatially-confined phase separated manganite structures

7.1 Introduction

Spatial manipulation of electron transport in strongly correlated ferromagnetic oxides has allowed one to understand the nature of complex couplings between spin, charge, lattice, and/or orbital degrees of freedom, which are responsible for a number of striking phenomena observed in these systems, such as colossal magneto-resistance (CMR), Mott transition, multiferrocity, high temperature superconductivity, etc..[108, 109, 110, 111, 112]

The anisotropic magneto-resistance (AMR) in CMR manganites, which is the difference in the resistances at different orientations between the magneti-

zation and the current density, is one of the fundamental magneto-transport parameters that has attracted considerable attention because of its unusual behavior in these materials.[55, 61] The AMR has potential applications in magnetic data storage devices and spintronics.[113, 114] Moreover, understanding of the AMR might shed light on the nature of other fundamental properties, believed to be associated with the AMR, such as spin-orbit coupling or magneto-crystalline anisotropy in magnetic materials.[115] Unfortunately, the microscopic mechanism of the AMR in these complex oxides remains unclear.

An example is a puzzling feature in the temperature dependence of the AMR; a peak in the vicinity of the ferromagnetic metallic (FM)-paramagnetic insulator (PI) transition temperature (T_{MIT}).[92] There is a great deal of debate about the mechanisms that produce the AMR peak near T_{MIT} . At present, many studies refer to the anisotropic Jahn-Teller (JT) electron-lattice couplings[64, 116] or local electronic non-uniformities[77] as the primary mechanisms. However, understanding how these processes contribute to the AMR peak at T_{MIT} has been always elusive.

Recent experiments have shown that the fluctuations between the competing phases such as ferromagnetic metallic (FMM) and charge-ordered insulating (COI) domains is the dominant phenomenon that governs the first-order electronic phase transitions in phase separated $(La_{1-y}Pr_y)_xCa_{1-x}MnO_3$ manganite thin films.[37, 102]

Direct observation of these fluctuations with the electron transport and various imaging techniques[28, 32, 100] have revealed that at the metal-insulator

transition a universal and smooth transition does not occur in all these domains; instead, electronic phases in finite domains individually flip from a metal to an insulator.

These experimental observations raise several intriguing questions; What is the AMR of a trapped single domain phase? Can we gain further insight into the nature of the AMR effect in these complex materials by isolating or monitoring the domain fluctuations? If the spatial dimension is reduced towards the length scale of the electronic phase separation (EPS), how do the competing electronic phases behave, and how does the AMR respond to this situation?

In the previous chapters, we revealed that AMR magnitude and sign have different characteristics for compressive and tensile strained millimeter-wide LPCMO films. How are those properties affected by the spatial confinement? In the next two sections, we are looking for the answers to these questions by analyzing the AMR of phase-separated LPCMO manganite micro-bridges deposited on LAO and STO single crystal substrates.

7.2 Anisotropic magneto-resistance of spatially confined LPCMO/SrTiO₃ epitaxial films

7.2.1 Experimental details

In order to investigate the microscopic nature of AMR in strongly correlated ferromagnetic oxides, and address questions raised in the introduction part, we manufactured two 45 nm thick La_{0.3}Pr_{0.4}Ca_{0.3}MnO₃ (LPCMO) micro-bridges of dimensions 2 μm \times 2 μm and 25 μm \times 25 μm , respectively. LPCMO is an ideal system for these types of studies since the ferromagnetic metallic FMM and charge order insulating COI domains have a size of over 1 μm near T_{MIT} .^[29] The LPCMO micro-bridges of this size can be produced using the standard wet-etch photolithography.

45 nm thick LPCMO films were deposited on SrTiO₃ substrates at a temperature of 750 °C by using direct current (d.c.) magnetron sputtering in an argon-oxygen mixture of partial argon and oxygen pressures of 20 mTorr and 100 mTorr, respectively. After the deposition, the chamber was filled with oxygen at atmospheric pressure in order to ensure the optimum oxygen content in these samples. The films were then cooled down to 650 °C with a rate of 10 °C/min, followed by annealing at 650 °C for 3 hours and subsequent cooling to room temperature with a rate of about 15 °C/min. The deposition rate was calibrated before films deposition by using Alphastep 250 profilometer. The appropriate geometries of the bridges were obtained by using standard pho-

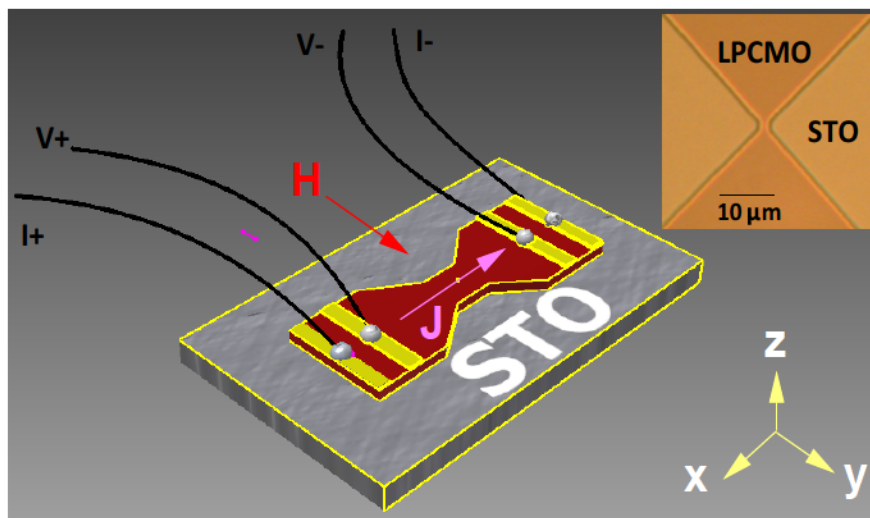


Figure 7.1: The device geometry showing LPCMO films fabricated on the STO single crystal substrates. $1 \mu\text{A}$ current I is applied in the x direction. Magnetic field H is applied in the xy plane of the film. Upper inset shows the image of the $2 \mu\text{m}$ wide bridge.

tolithography to pattern the LPCMO films, then using a suitable wet-etchant to remove the irrelevant parts of the manganite films.

After patterning the films, silver contacts were sputter deposited on LPCMO films. Resistance measurements were performed using a Keithley 6221 DC/AC current source and Keithley 2182A nanovoltmeter. GMW 3473-MRD (Motorized Rotating Drive) was used to rotate the electromagnet from 0 to 180 degrees with a 0.01 degree resolution. The system control and data collection was done using homebuilt LABVIEW drivers. All the resistance data presented in this paper were collected using four probe method and a constant current of 1 micro-ampere.

We report here for the first time remarkable changes of the AMR in LPCMO micro-bridges that are dramatically different from those observed in bulk thin films of the same material. We have discovered that a decrease of the size of an epitaxial LPCMO thin film to a micro-bridge of a width comparable to that of a mesoscopic phase separated domain in LPCMO leads to a giant resistive switching as one sweeps the magnetic field in the plane of the film. The magnitude of the observed oscillations has been found to be extremely sensitive to temperature. This emergent effect is driven by temperature sensitive electronic phase fluctuations involving FMM and COI phases.

The $2 \mu\text{m} \times 2 \mu\text{m}$ and $25 \mu\text{m} \times 25 \mu\text{m}$ micro-bridges were patterned (see Fig. 7.1) from the LPCMO film epitaxially grown on $\text{SrTiO}_3(001)$ substrates. (Using square geometry allows both micro-bridges to have very similar resistances at room temperature). The resistance R , and its dependence on

temperature, time and angle θ between the directions of the magnetic field H_{ex} and current I (see Fig. 7.2 (a)) were measured with the standard four point probe method over a temperature range between 10 K and 300 K, and in a magnetic field up to 1.1 Tesla. The AMR indicates the relative change in the resistance as the angle between the applied magnetic field H_{ex} and the direction of the current I changes. To quantify the resistance change, we calculated the percentage of a change of an in-plane AMR using the following expression

$$AMR = \frac{R_{\parallel} - R_{\perp}}{\frac{R_{\parallel}}{3} + \frac{2R_{\perp}}{3}} \times 100\% \quad (7.1)$$

Here R_{\perp} ($\theta=0^{\circ}$ or 180°) is the resistance measured in a field of 1.1 T perpendicular to the current direction and R_{\parallel} ($\theta=90^{\circ}$) is the resistance measured with 1.1 T parallel to the current direction.

7.2.2 Results and discussion

Temperature dependencies of the resistance $R(T)$ and anisotropic magnetoresistance, $AMR(T)$ for the $2 \mu\text{m}$ and $25 \mu\text{m}$ wide LPCMO micro-bridges are shown in Fig. 7.2 (a) and 7.2 (b). These curves were measured during cooling from 300 K to 10 K at 1.1 T. All bridges show the metal-insulator transition at around 142 K. In the insulating region, both bridges show a monotonic increase of resistance with a decreasing temperature down to T_{MIT} . However, in the metallic region at temperatures below T_{MIT} , the bridges exhibit dif-

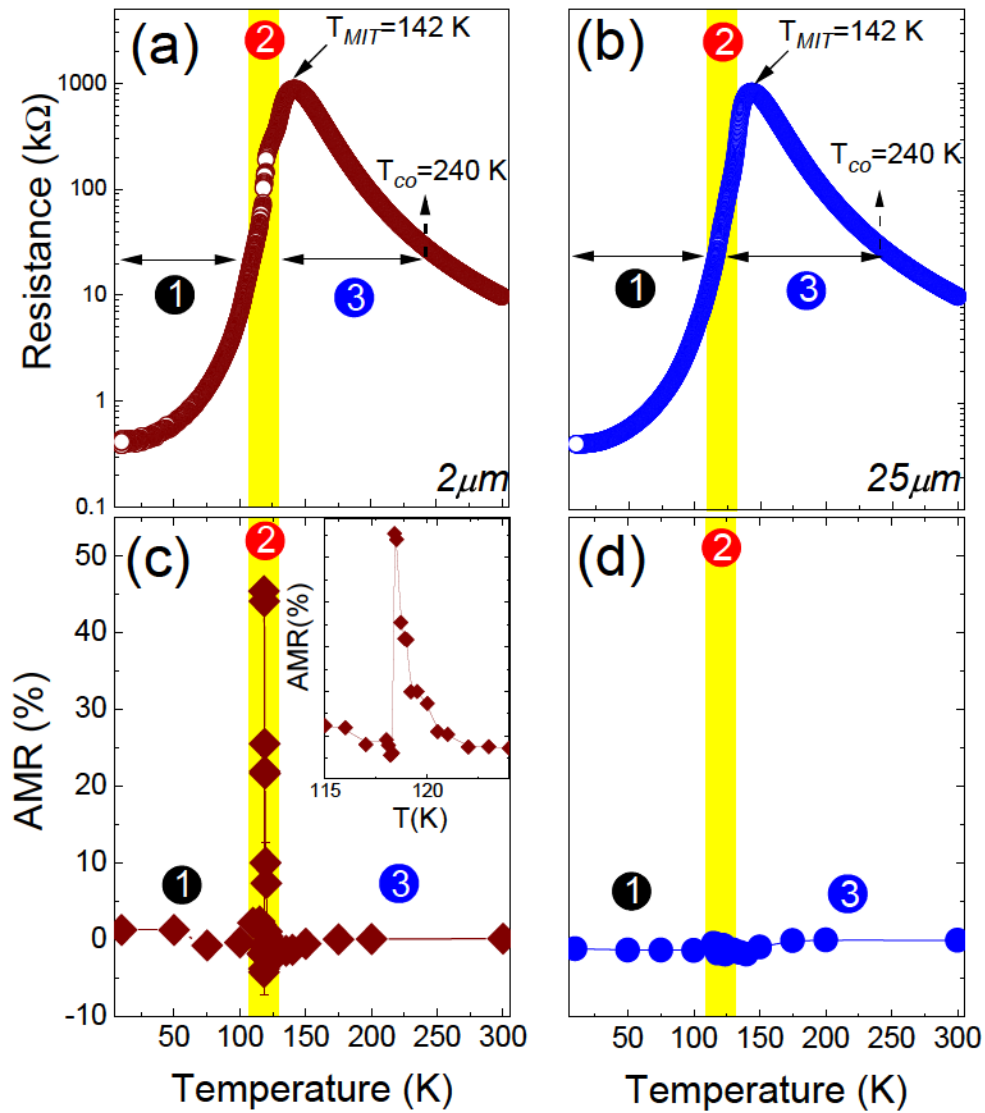


Figure 7.2: (a) R - T curve for the 2 μm bridge, which shows several discrete jumps in the vicinity of the T_{MIT} , as a consequence of the reduction of conducting channels down to a single pathway.[11] (b) The R - T curve for the 25 μm wide bridge showing no discrete steps. (c), 2 μm bridge shows large and sharp (see the inset) in-plane AMR at the same temperature range where these step-like features are observed. (d) AMR for wider, 25 μm bridge is negligible.

ferent $R(T)$. $R(T)$ of the 25 μm bridge decreases smoothly with a decreasing temperature. However, $R(T)$ of the 2 μm bridge shows discontinuities, i.e., sudden drops of the resistance over a narrow temperature range. These measurements were repeated several times in order to verify the reproducibility of these curves. It was observed that the jumps in $R(T)$ of the 2 μm bridge occur at slightly different temperatures (with differences of about 0.1-0.5 K) or an applied fields when the measurements are repeated. No noticeable changes have been observed in $R(T)$ for the 25 μm bridge.

These observations are consistent with other work on small scale LPCMO films,[11, 96, 117] confirming that the stepped transitions in the resistance of the 2 μm bridge originate from the spatial confinement effect when the size of the bridge is comparable to the length scale of the FMM and COI domain, which ranges from a few to several hundred micrometers. It is known that the FMM metallic domain grows in size at the expense of the insulating phase during cooling to temperatures below T_{MIT} . The sudden drop in the resistance occurs when the localized FMM regions in the bridge become electrically connected. The drops continue until the system reaches predominantly metallic FMM phase in the bridge. This happens at temperatures below 115 K (see Figure 7.2 (a)). In electronically phase separated systems, the formation of the FMM and the COI domains is random.[36] This means that the transport channel in the bridge changes whenever the system goes through a new temperature cycle, resulting in the resistivity jumps taking place with slightly different magnitudes at slightly different temperatures.

Figures 7.2 (c) and 7.2 (d) show the temperature dependence of the magneto-

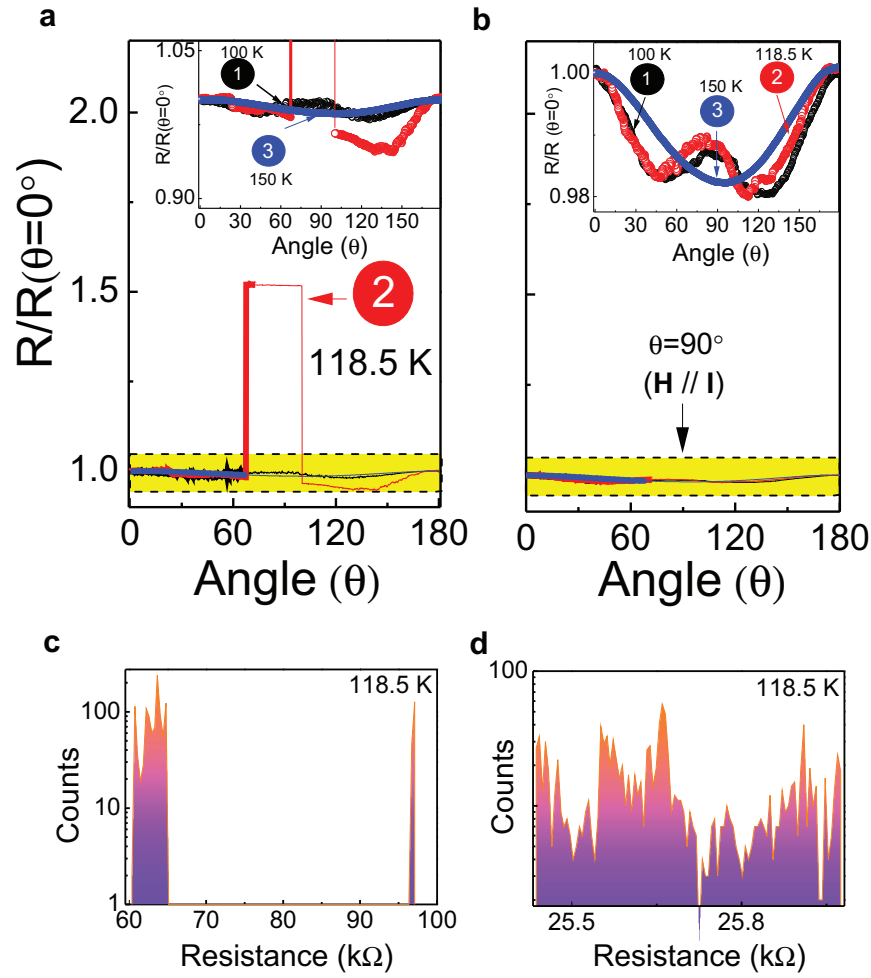


Figure 7.3: (a) Angular dependence of resistance $R(\theta)$ for the $2\ \mu\text{m}$ wire reveals dramatic rectangular-like feature at the AMR peak temperature of $118.5\ \text{K}$. The inset shows the expanded view of the normalized $R(\theta)$ at $118.5\ \text{K}$ compared with those at $100\ \text{K}$ and $150\ \text{K}$. (b) $R(\theta)$ for the $25\ \mu\text{m}$ bridge shows regular oscillatory behavior at all selected temperatures (see the inset). (c) and (d) The histogram of the resistance collected at $118.5\ \text{K}$ for the $2\ \mu\text{m}$ and $25\ \mu\text{m}$ bridges during the measurement of $R(\theta)$ in the plane of the films. The angle θ between the \mathbf{H} and \mathbf{I} directions is 0° for \mathbf{H} perpendicular to \mathbf{I} , and 90° for \mathbf{H} parallel to \mathbf{I} .

resistive anisotropy $\text{AMR}(T)$ for the $2\ \mu\text{m}$ and $25\ \mu\text{m}$ micro-bridges. Numbers 1, and 3 represent temperatures where the films contain predominantly FMM and COI phases at 100 K and 150 K, respectively. Number 2 marks temperature region around 118.5 K where mixed FMM and COI phases coexist. For the $25\ \mu\text{m}$ wide film, the AMR is negligibly small (see Fig. 7.1 (d)). In this film, $R(\theta)$ is similar to an angular dependence frequently observed at all temperatures in many bulk manganite films.[98, 104] However, the temperature dependence of the AMR in the $2\ \mu\text{m}$ micro-bridge shows a very sharp peak at 118.5 K (see Fig. 7.1 (e)). Its magnitude is about 48%. Note that this value is much higher than that of the in-plane AMR values of approx. 2.5% reported in millimeter wide manganite films.[118] Furthermore, the AMR observed in the $2\ \mu\text{m}$ micro-bridge is extremely sensitive to temperature, i.e. a temperature change of only 0.5 K causes the AMR to change from 1% to 48% (see inset in Fig. 7.1 (e)).

In Figures 7.3 (a) and 7.3 (b), we show $R(\theta)$ for both bridges at selected temperatures. In the $2\ \mu\text{m}$ bridge at the AMR peak temperature of 118.5 K, the angular dependence of the resistance reveals ultra-sharp jumps (resistive-switching) with a rectangular-like features (see Fig. 7.3 (a)). These jumps are responsible for the large AMR value discussed earlier. Such sharp jumps are not seen in the $25\ \mu\text{m}$ bridge (see Fig. 7.3 (b)). Values of all resistances collected during the measurements of $R(\theta)$ at 118.5 K are presented in histograms shown in Figures 7.3 (c) and 7.3 (d) for both bridges. It is interesting that the $2\ \mu\text{m}$ bridge produces “unique” two-state resistance states, while this behavior is not seen for a wider $25\ \mu\text{m}$ bridge.

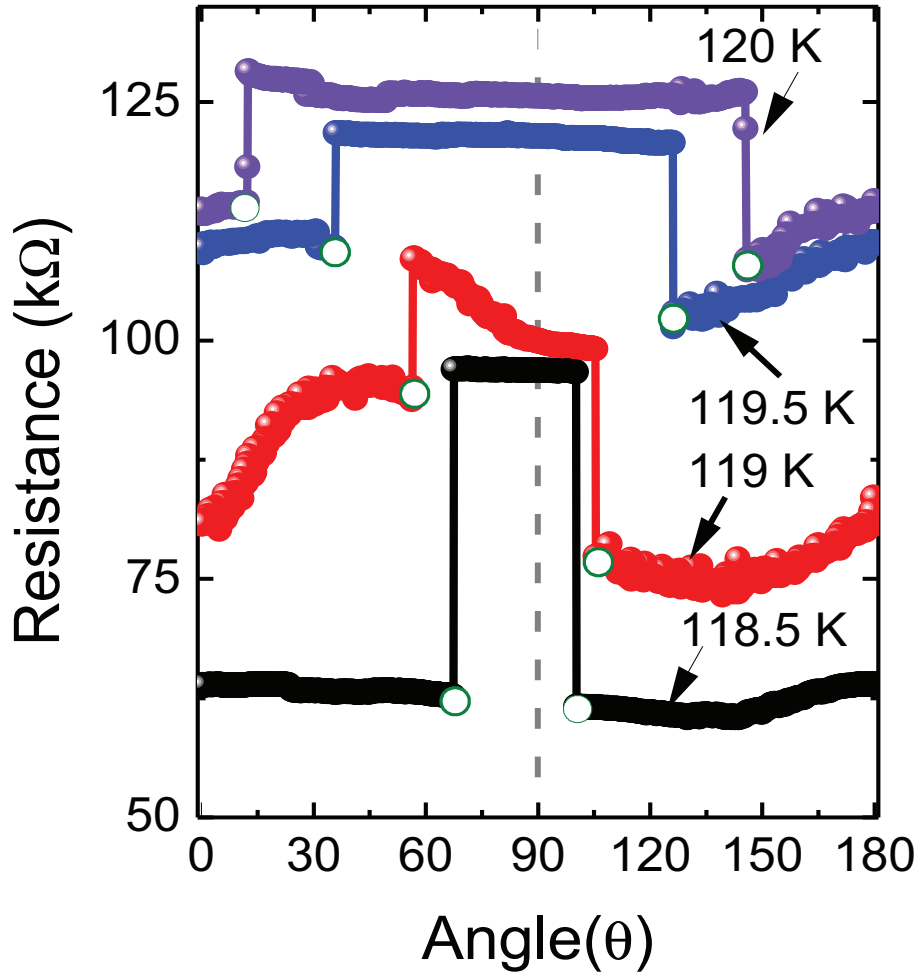


Figure 7.4: Temperature evolution of the angular dependence of resistance around the AMR peak for the 2- μm wide bridge shows ultra-sharp resistance jumps of a various height and width. The difference between the switching angles, indicated as white dots increases with an increase of temperature from 118.5 K to 120 K with a 0.5 K steps.

It is known that at temperatures near the T_{MIT} , the shape and size of the FMM and insulating domains evolve with changing temperature.[119] FMM domain phase grows in size with a decreasing temperature. In order to gain clearer insight into the mechanism responsible for the dramatic changes in the resistance, we have investigated the effects of the temperature dependent domain size on the $R(\theta)$ in the 2 μm bridge (see Figure 7.4). Before each measurement the temperature of the sample was increased to 300 K (the paramagnetic insulating region) to reset the electronic inhomogeneity between the competing FMM and COI phases, and subsequently cooled down in a zero field to the temperature of the measurement. At temperatures between 118 K and 120 K sharp changes in the resistivity occur at the critical angles with a rectangular-shaped θ dependence. The angle where these changes take place are indicated by white-colored dots. In this temperature region the difference between the switching angles increases with an increasing temperature. It is also noticeable that the resistance change between 0° and 90° , i.e. the AMR, decreases as the difference between the switching angles increases.

We observed however, that the resistive switching does not occur at the same angle if the measurement is repeated (always following the same procedure of cooling the bridge from 300 K before each measurement). This observation rules out the possibility that the sharp changes at some switching angles are associated with the structural defects in the LPCMO bridge. In such a case reproducible jumps would be produced at the same switching angles for each temperature cycle.

What is the origin of these sharp jumps? Previous time-resolved resistance

measurements for 10 μm wide $\text{La}_{5/16}\text{Pr}_{5/16}\text{Ca}_{3/8}\text{MnO}_3$ bridge has shown fluctuations between two states in the resistance within a narrow temperature regime near T_{MIT} .^[102] These fluctuations are believed to be due to individual domains fluctuating between metallic FMM and insulating COI phases and were explained in the context of a percolating network. For example, the up and down jumps are consequences of the fluctuation between the COI and FMM phases present in the bridge.

Our experiments imply however, that sharp jumps between “low resistance” and “high resistance” states in $R(\theta)$ cannot be explained by the percolation model. This conclusion is based on the measurements of the time relaxation of the resistance for the 2 μm LPCMO bridge at 118.5 K (see Figure 4). During the first 1000 - 3000 seconds (see Figures 7.5 (a), (b), (c)), θ was fixed at 0° and time dependent resistance, $R(t, \theta = 0^\circ)$ was measured in a field of 1.1 T. Immediately after, (as indicated by dashed lines in these figures) the dependence of the resistance on time $R(t, \theta=0^\circ \leftrightarrow 180^\circ)$ was measured during the back-and-forth angular sweeping of the field direction relative to the current direction between 0° and 180° (see the inset of Fig. 7.5 (b)). Note that $R(t, \theta = 0^\circ)$ show sharp resistance drops that occur at different times. In a widely accepted percolative transport model, this implies that the transport channel in the bridge changes during each decay measurement indicating that the formation of electronic domains is different. On the other hand, the AMR measured during the back-and-forth angular sweeping have been found to be surprisingly robust, showing the up-and-down sharp resistive switchings between the low and high resistance states without change in their magnitude

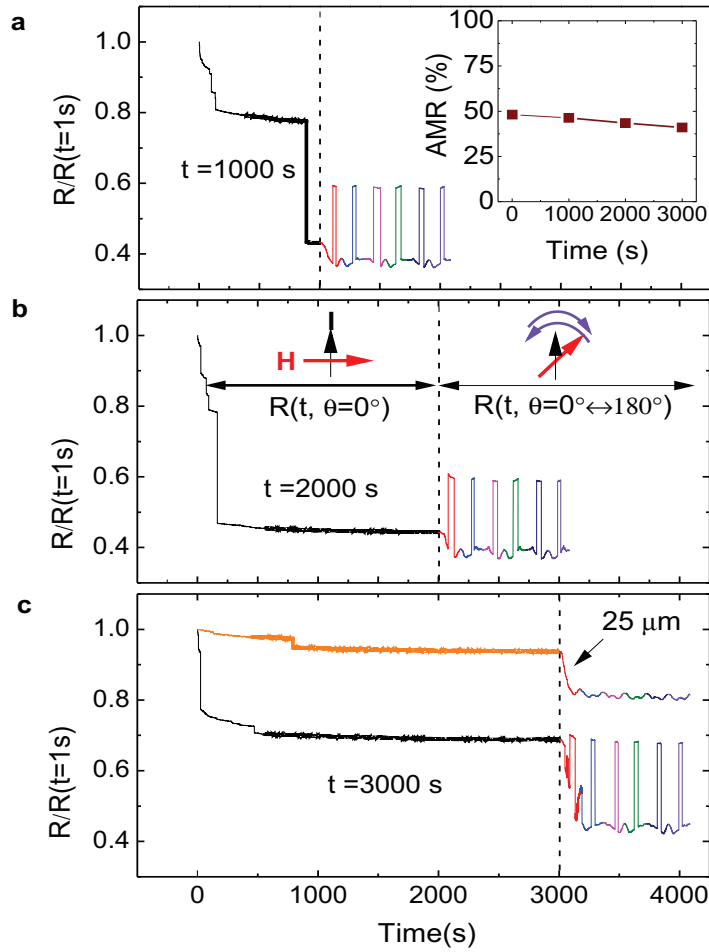


Figure 7.5: The dependence of the resistance on time in a field of 1.1 T perpendicular to current direction ($\theta=0^\circ$) at 118.5 K for the 2- μm wide bridge. The measurements of the resistance for waiting times larger than (a), ($t=1000$ s) (b), ($t=2000$ s) and (c), ($t=3000$ s) (i.e., after dashed lines) were performed during the angular repetitive sweeps of θ between 0° and 180° (see the inset of Fig. 7.4 (b)) The amplitude of the resistive switching was only slightly affected after various decay-time measurements (shown in the inset of Fig. 7.4 (a)). Black arrows in (b) show the direction of the current I .

(see the inset of Fig. 7.5 (a)). We rule out percolation as a possible source of this switching effect, since any variations within the percolating network in the bridge would affect the difference between the “low resistance” and “high resistance” states in $R(\theta)$. $R(t)$ and $R(\theta)$ measured for the 2 μm and 25 μm LPCMO bridges are dramatically different (see Fig. 7.5 (c)). The 25 μm bridge shows regular AMR oscillations similar to those reported for 0.5 mm wide LPCMO bridges.[120]

Recently, measurements of the angular dependence of the conductance in Co nano-contacts at room temperature and in 1 T field were reported by Sokolov *et al.*[121] They found abrupt steps in the conductance at particular angles, of magnitudes of the order of e^2/h ($=1/25,813 \Omega^{-1}$) conductance quantum per electron spin. They associated this effect (called ballistic AMR (BAMR)) with the ballistic transport and the opening and closing of discrete quantum channels at the nano-contact. The ballistic transport happens in quantum point contacts where there is no contribution from electron scattering to the conduction. The BAMR effect is unlikely to occur in our case where micron-sized manganite bridges are used.

We are therefore convinced that the resistive switching in the 2 μm LPCMO bridge is caused by a different mechanism, namely the formation of a spin-valve-like intrinsic FMM-COI-FMM tunnel structure at the critical temperatures (see Fig. 7.6 (a) where this mechanism is schematically depicted). The arrangement of FMM-COI-FMM domains is similar to that of the conventional magnetic tunnel junction (MTJs) which consists of a free and pinned ferromagnetic electrodes separated by a thin (MgO or Al_2O_3) spacer.[122, 123]

In conventional spin valves, the switching of the resistance is caused by the magnetization reversal of free and pinned ferromagnetic layers which create the anti-parallel (high-resistance) or parallel (low-resistance) states in these devices. The magnetization reversal in each layer is determined by the magnitude of their coercive fields during the application of magnetic field.

The existence of tunnel barriers in our 2 μm bridge has been confirmed from the measurement of the I - V characteristics at temperatures where the giant resistive-switching occurs. Our results have shown that the differential conductance (dI/dV) versus V fits well to the Simmons' low voltage approximation equation [124] of the form $dI/dV = \alpha + 3\gamma V^2$, (where α and γ are the fitting parameters representing the average tunnel barrier height and the barrier thickness).

The details of the proposed mechanism of resistive switching in the 2 μm bridge is depicted in Fig. 7.6 (b). For this arrangement it is reasonable to assume that the pinning of one of the two FMM domains in the bridge is stronger than the other. The pinning and its strength could be the consequence of the exchange bias at the interface between the anti-ferromagnetic COI barriers and FMM regions as previously studied for bulk phase separated manganites, see for example.[10, 125, 126] When the field is applied the magnetizations in both domains are parallel to the field direction. As the field rotates starting at small angles, the magnetization in the weakly pinned FMM domain (for example, FMM-1) follows the applied field direction first. At a certain angle (i.e., the switching angle) the magnetization of the FMM-1 domain suddenly flips and its direction is completely anti-parallel to the strongly pinned FMM-2

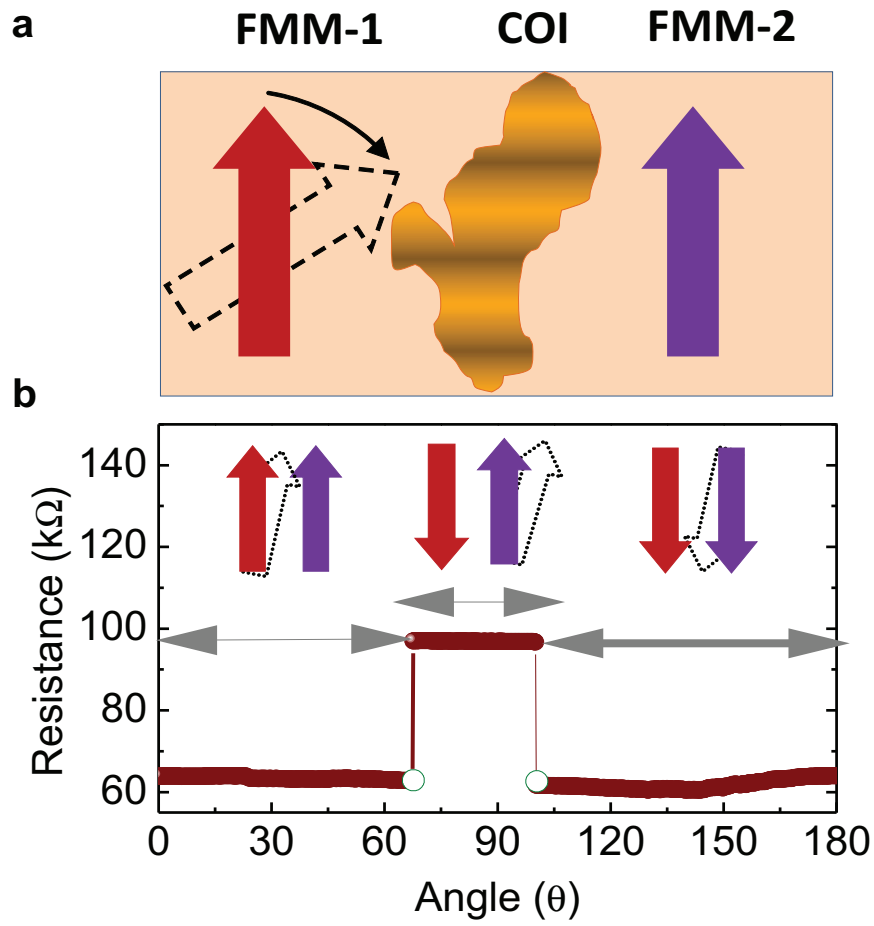


Figure 7.6: (a) Schematic of the switching phenomena for intrinsic FMM-COI-FMM domains in $2 \mu\text{m}$ bridge. Magnetization of FMM-1 domain rotates freely with the rotation of applied magnetic field. (b) Switching results in a completely anti-parallel or parallel state whereas intermediate states represent the small change of the resistance on the angle (represented by the orange colored double sided arrows).

domain (represented by a white dot in Fig. 7.6 (b)). Due to the flipping of the magnetization at this angle, the spin-dependent scattering of conduction electrons across a thin COI barrier is enhanced resulting in a sharp increase of the resistance. At higher angles, the magnetization of the FMM-2 domain follows the field until at a certain angle it flips sharply and its direction is now parallel to the magnetization of the FMM-1 domain and the external field. This results in a sharp drop of the resistance.

As suggested earlier, the size and spatial distribution of the FMM and COI domains are temperature dependent producing different FMM-COI-FMM configurations at different temperatures around the AMR peak, and different switching angles (shown as white dots in Fig. 7.4).

7.2.3 Conclusions

We have observed giant resistive switching in the in-plane AMR of spatially confined LPCMO thin film. We attribute this switching to the intrinsic magnetization reversal of the ferromagnetic metallic domains separated by tunneling COI barrier. Sharp switching of the resistance of electronically separated spatially confined single manganite bridge is potentially promising for certain device application. These findings also shed new light on the nature and dynamics of the formation of the AMR in strongly correlated systems.

7.3 Anisotropic magneto-resistance of spatially confined LPCMO/LaAlO₃ epitaxial films

7.3.1 Introduction

As mentioned in section 7.2, a decrease of the width of an tensile strained LPCMO/STO thin film bridge to that of a mesoscopic phase separated domain leads to a giant resistive switching as one sweeps the magnetic field in the plane of the film, and the sharp rectangular wave-like AMR instead of a regular oscillatory $\cos^2(\theta)$ -like AMR.

The question is what happens to the spatially confined manganite thin film is under a compressive strain. As revealed in Chapter 5, the AMR in millimeter-wide LPCMO/LAO film exhibits a sign transformation (cross-over) at a certain temperature T^* . How is this change in sign affected by the spatial confinement, especially over the temperature range where the size of the metallic and insulating domains are extremely sensitive to the small changes in the temperature? In this section, we study the confinement effect in $\text{La}_{0.3}\text{Pr}_{0.4}\text{Ca}_{0.3}\text{MnO}_3$ /LAO micron-size film bridges to address such questions. The results are compared to those obtained for LPCMO/STO microbridges.

7.3.2 Experimental procedure

$\text{La}_{0.3}\text{Pr}_{0.4}\text{Ca}_{0.3}\text{MnO}_3$ (LPCMO) thin films (thickness ~ 45 nm) were deposited on a (100)-oriented LaAlO_3 substrates at a temperature of 750°C by off-axis magnetron sputtering in an oxygen-argon mixture, with O_2 and Ar pressures of 100 mTorr and 20 mTorr, respectively. After the deposition, the chamber was filled with pure oxygen at the atmospheric pressure, then the films were cooled down to 650°C at a rate of $\sim 3^\circ\text{C}/\text{min}$. and annealed for 3 hour at this temperature followed by cooling the films down to room temperature at a rate of $20^\circ\text{C}/\text{min}$. Wires of different widths (i.e., $50\ \mu\text{m}$, $25\ \mu\text{m}$ and $5\ \mu\text{m}$) have been fabricated from a single LPCMO film using optical lithography. Four silver pads have been deposited on LPCMO films to serve as current and voltage contacts. Electrical transport measurements were performed using a Keithley 6221 DC/AC current source and Keithley 2182A nanovoltmeter. GMW 3473-MRD (Motorized Rotating Drive) was used to rotate the electromagnet from 0 to 180 degrees with a 0.01 degree resolution. The system control and data collection were done using homebuilt LABVIEW drivers. The resistance R , and its dependence on the temperature, time and angle θ between the directions of the magnetic field \mathbf{H} and current \mathbf{I} (see Figure 7.7 (a)) were measured with the standard four point probe method over a temperature range between 10 K and 300 K, in magnetic fields up to 1.1 Tesla.

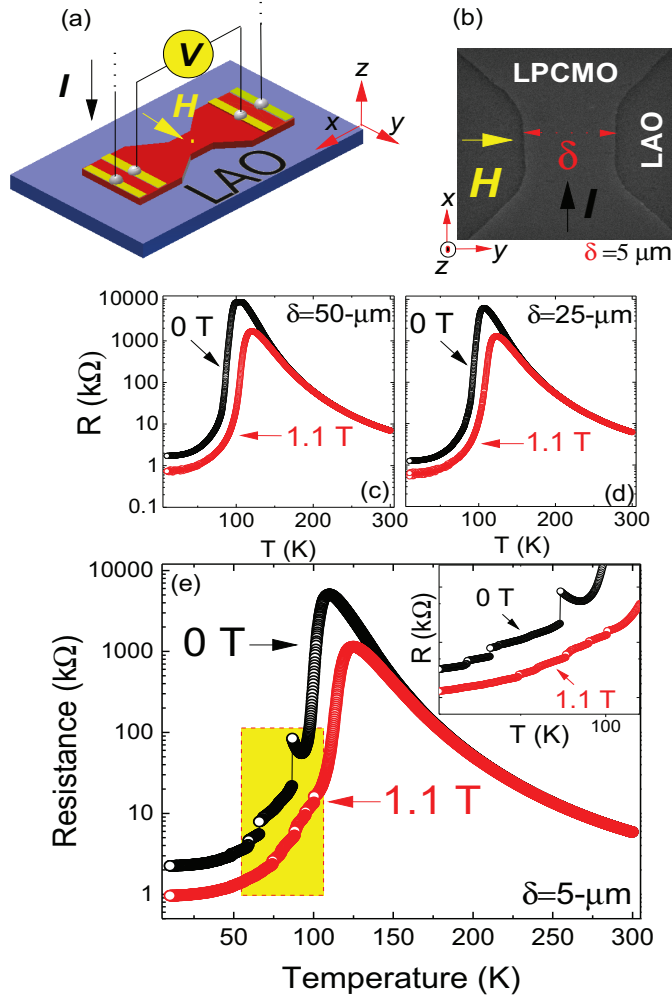


Figure 7.7: (a) The device geometry of LPCMO film fabricated on the (001) oriented LaAlO₃ substrates. A constant 1 μA current I , flows in the x direction while the magnetic field H is applied in the xy plane of the film. (b) The scanning electron micrograph (SEM) of the $5 \mu\text{m} \times 5 \mu\text{m}$ bridge (δ indicates the width of the bridge). (c)-(e) Resistance versus temperature for the $50 \mu\text{m}$, $25 \mu\text{m}$ and $5 \mu\text{m}$ wide La_{0.3}Pr_{0.4}Ca_{0.3}MnO₃ bridges in a zero-field and a magnetic field of 1.1 T, measured during cooling cycle. The inset in (e) shows the expanded view of sharp jumps detected on the $R(T)$ curve of the $5 \mu\text{m}$ -bridge.

7.3.3 Experimental Results

Figures 7.7 (c)-(e) show the temperature dependence of the resistance of 50 μm , 25 μm and 5 μm wide LPCMO wires measured in 0 T and 1.1 T magnetic fields. For bridges of 50 μm and 25 μm in width, the $R(T)$ curves are smooth as typically observed for wide thin films and bulk manganites. In the case of 5 μm bridge, during cooling, the metal to insulator transition temperature (T_{MIT}) occurs at roughly the same temperature (~ 115 K) as in the wider films. However, sharp resistance drop are present at ~ 90 K. Multiple jumps are visible at temperatures down to 59 K (see shaded region in the figure).

Application of 1.1 T reduces the size of the jumps dramatically and shifts them toward higher temperatures.[34] These observations are consistent with other work on small scale LPCMO films,[117, 127] confirming that the effects observed on the 5 μm bridge originate from the spatial confinement, where the size of the bridge is comparable to the length scale of the ferromagnetic metallic (FMM) or charge-ordered insulating (COI) electronic domains. As mentioned earlier, the sudden drop in the resistance occurs when the localized FMM regions in the bridge are electrically connected.[11, 37, 102] The drop continues until the bridge becomes predominantly metallic. FMM domains grow in size at the expense of the insulating phase where a magnetic field is applied. This produces magnetically more homogeneous electronic domains in the LPCMO bridge which consequently reduces the possibility of the resistance drop.[101, 119]

Confining electronic phases in the 5 μm LPCMO bridge allows us to ex-

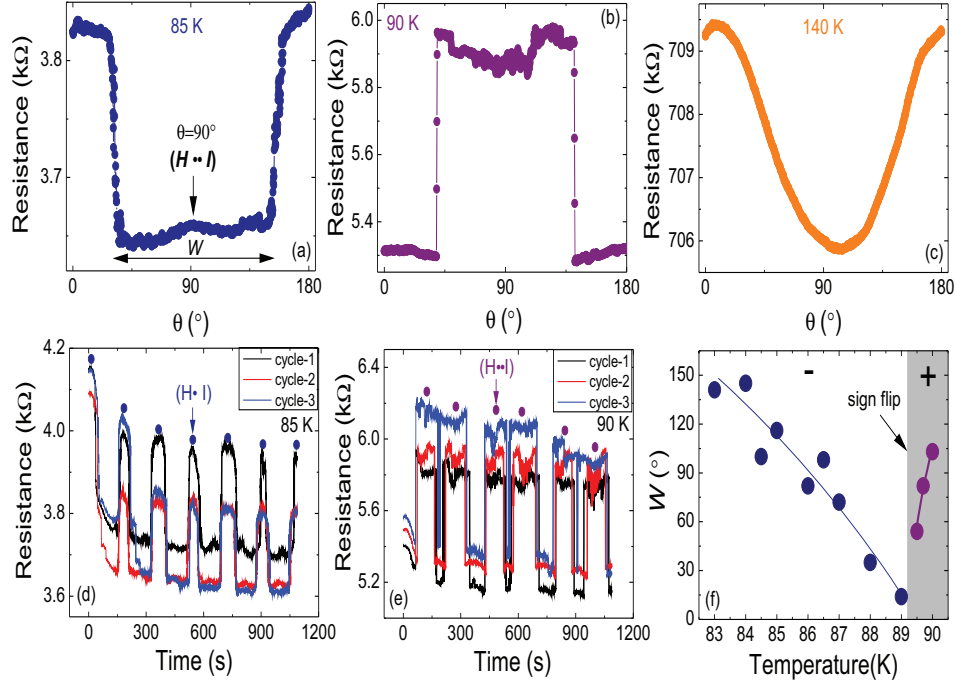


Figure 7.8: The dependence of the resistance on the angle θ between the transport current \mathbf{I} and magnetic field \mathbf{H} for 5 μm wide LPCMO bridge. $R(\theta)$ was collected at 85 K (a), 90 K (b) and 140 K (c). Note that $\theta = 0^\circ$ for \mathbf{H} perpendicular to \mathbf{I} , and 90° for \mathbf{H} parallel to \mathbf{I} . The width, W of the rectangle in $R(\theta)$ is indicated by a double-sided arrow. (d) and (e) show the dependence of the resistance on time obtained during the in-plane rotation of the magnetic field at 85 K and 90 K. Each cycle of measurements was obtained after the same warming and cooling procedures (see text). The blue and violet dots in (d) and (e) indicate the maximum resistance obtained for $\mathbf{H} \perp \mathbf{I}$ and $\mathbf{H} \parallel \mathbf{I}$, respectively. (f) W as a function of temperature. The sign of the AMR suddenly changes at 89 K.

amine the dependence of the resistance $R(\theta)$ on the angle θ between current and the field directions for this bridge. This is mainly due to the strong phase separation in LPCMO manganites [128] where the electronic domains are micron in size and can be reached by patterning the LPCMO film using optical lithography. Figures 7.8 (a)-(c) show variety of $R(\theta)$ curves observed in 5 μm bridge. At 85 K (see Fig. 7.8 (a)), the resistance of the bridge has rectangular-like angular dependence with a width of curve W , ranging from 30° to 150° . However, at 90 K (see Fig. 7.8 (b)), the sign of the AMR flips from negative to positive very sharply (a $\theta=90^\circ$ shift in $R(\theta)$). The regular oscillatory behavior of $R(\theta)$ is seen at 140 K. In order to verify the reproducibility of sharp jumps in $R(\theta)$ at temperatures between 85 K and 90 K, we measured time dependence of the resistance (see Fig. 7.8 (d) and 7.8 (e)) which was collected during the back and forth angular sweeps of magnetic field between 0° and 180° . Before each cycle, temperature was raised to 300 K and subsequently reduced to the set temperatures (i.e., 85 K, 90 K) in a zero magnetic field.

Blue and violet dots in Figures 7.8 (d) and (e) which indicate high resistance states of the curves, were obtained at $\mathbf{H}\perp\mathbf{I}$ and $\mathbf{H}\parallel\mathbf{I}$, respectively. Repetitive measurements revealed that sharp changes in the resistance do not occur exactly at the same angle/time.

In order to achieve deeper understanding of the ultra-sharp features in the AMR for the 5 μm bridge, we investigated temperature evolution of the width of the rectangular $R(\theta)$ curves (see Fig. 7.8 (f)). The width, W of the square-wave AMR is reduced significantly from 150° to 15° as the temperature increases from 83 K to 89 K. Surprisingly, at higher temperatures, the sign of

the AMR suddenly changes and W increases. At temperatures higher than 90 K, no more square wave-like behavior in the AMR is observed. Compared to the results obtained for millimeter-wide LPCMO films (see Chapter 5), the crossover in sign becomes more sensitive to temperature as the width of the LPCMO bridge approaches the size of the intrinsic domains.

Dependence of AMR on magnetic field at 85 K and 90 K is plotted in Figs. 7.9 (a) and (b). Interestingly, when a magnetic field increases, the sign of the AMR gradually changes from positive to negative at 85 K (see Fig. 7.8 (a)), while at 90 K (see Fig. 7.9 (b)), the AMR shows positive ultra-sharp behavior at 0.6 T only.

The “confinement” effect on the temperature dependence of the AMR is shown for LPCMO films in Figure 7.10. The AMR is defined as $AMR = (\rho_{\parallel}^{in} - \rho_{\perp}^{in}) / \rho_{av}$, where ρ_{\parallel}^{in} is the resistivity of the film in a magnetic field of \mathbf{H} that is applied in plane of the film and oriented parallel to the current \mathbf{J} , and ρ_{\perp}^{in} is the resistivity measured when \mathbf{H} is applied perpendicular to the direction of the current in the plane of the film. The average resistivity ρ_{av} is defined as $\rho_{av} = (1/3)\rho_{\parallel}^{in} + (2/3)\rho_{\perp}^{in}$. Wider bridges (i.e., of 25 μm and 50 μm in width) (see the inset of Fig. 7.10) show a peak in the AMR(T) in the vicinity of the metal-insulator transition temperature, which is usually observed in bulk LPCMO and millimeter wide LPCMO films. However, the AMR is quite different for the 5 μ wide LPCMO bridge, where it shows a small broad minimum around 125 K as well as maximum and minimum located in the negative and positive regions of the $R(\theta)$ curve at 85 K and 90 K temperatures, respectively. Since the size and shape distribution of the metallic and

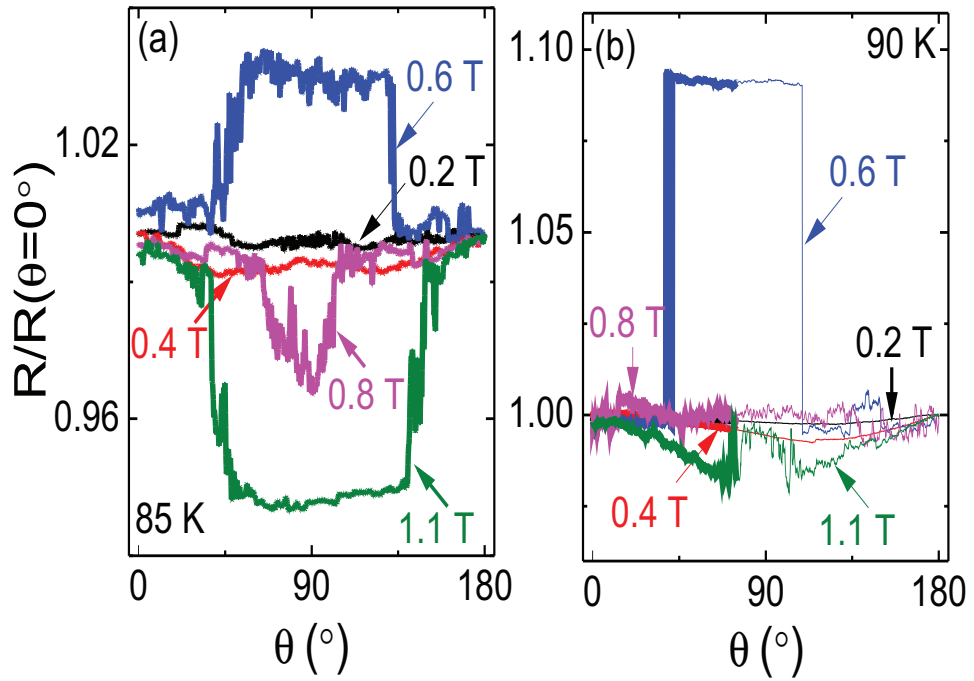


Figure 7.9: Dependence of the normalized resistance ($R/R(\theta=0^\circ)$) on the applied magnetic fields between 0.2 T and 1.1 T measured at (a) 85 K and (b) 90 K temperatures for the $5 \mu\text{m}$ -wide LPCMO/LAO bridge.

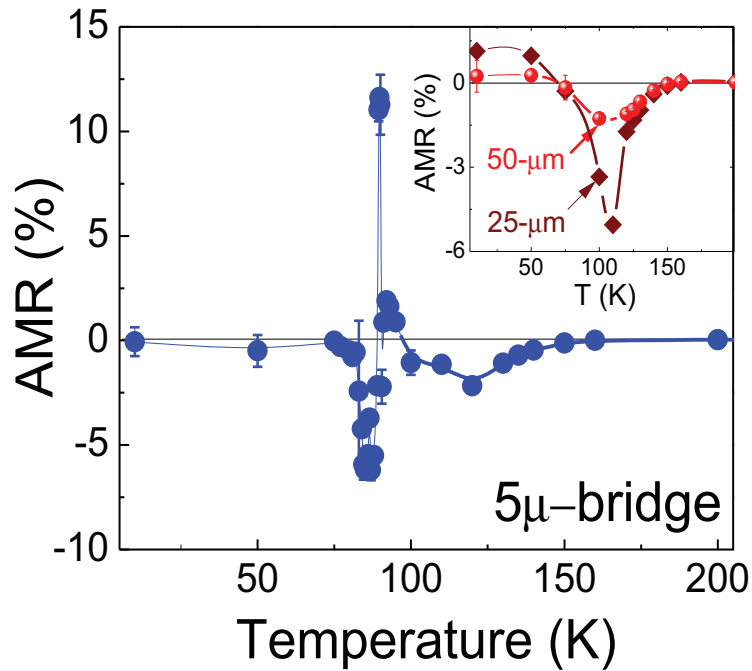


Figure 7.10: Dependence of the anisotropic magneto-resistance (AMR) on temperature in 1.1 T, recorded during cooling cycle for the 5 μm -wide LPCMO bridge. The inset shows temperature dependence of the AMR obtained for the 25 μm and 50 μm -wide LPCMO bridges.

insulating electronic phases in LPCMO films depends on thermal cycling (i.e., whether the measurements are taken during warming or cooling). one should expect different AMR(T) for these two cases. The AMR(T) measurements (see Fig. 7.11) taken during warming cycle show sharp peaks located almost at the same temperature but the magnitude is small. All these observations indicate that the spatial confinement has a profound effect both on the shape and the amplitude of the AMR effect in the EPS manganite systems.

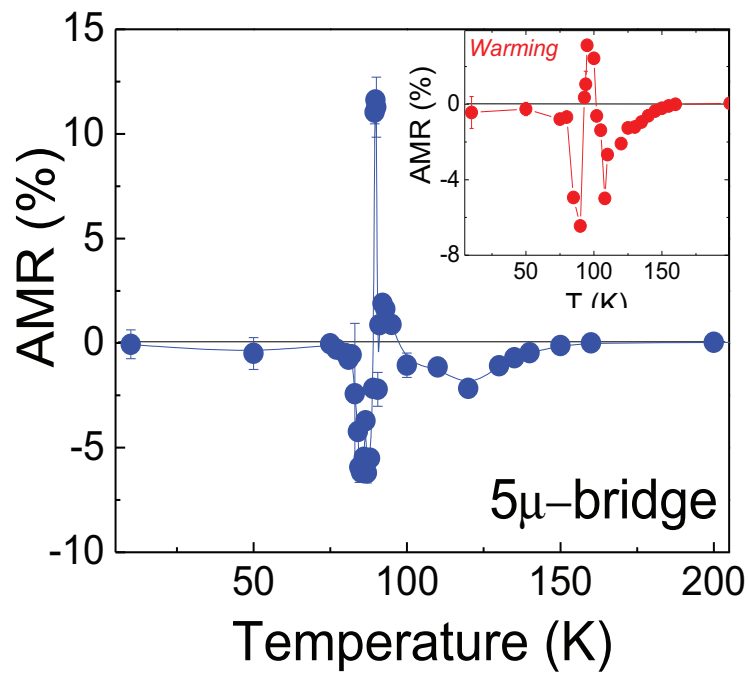


Figure 7.11: Dependence of the anisotropic magneto-resistance (AMR) on temperature in 1.1 T, recorded during cooling cycle for the $5\ \mu\text{m}$ -wide LPCMO bridge. The inset shows temperature dependence of the AMR obtained during warming cycle for the same LPCMO bridge.

7.3.4 Discussion

The observation of reproducible sharp jumps in $R(\theta)$ for the 5 μm LPCMO/LAO bridge rules out the possibility of structural defects that might have been produced during the lithography process. If the structural defects were created during this process, the same switching angles in $R(\theta)$ would have been produced at each temperature cycle.

Regarding the mechanism of unusual jumps in the AMR for LPCMO/LAO microbridges, we revisit discussion of similar phenomena in LPCMO/STO micro-bridge. Temperatures at which the spatial confinement effects are taking place, and special arrangement of FMM and COI domains (FMM domains separated by a thin COI tunnel domain) might be responsible for the ultra-sharp jumps in $R(\theta)$ for 5 μm LPCMO/LAO bridge. The formation of FMM-COI-FMM tunnel junction like intrinsic domains resembles to other tunnel junctions observed in bi-layered orthorhombic ruthenates such as $\text{Ca}_3\text{Ru}_2\text{O}_7$.^[129] Depending on the magnetic field and temperature, the layers could act as tunneling junctions consisting of a ferromagnetic metallic and anti-ferromagnetic insulating layers. At low temperatures, samples show abrupt drop (rise) in the magnetization at $\Theta = 20^\circ$ and 160° which consequently leads to a sudden rise (drop) in the resistivity during the rotation of the magnetic field.

As mentioned in Chapter 5, strain-driven magnetic anisotropy has a profound effect on the sign of the AMR for the millimeter-wide LPCMO films at low temperatures. Does the magnetic anisotropy influences the AMR sign change?

The low and high resistance states observed in the sharp $R(\theta)$ of $2\ \mu\text{m}$ LPCMO bridge were suggested to be the consequence of the parallel and anti-parallel magnetization alignments of the FMM domains in FMM-COI-FMM structure. As compared to positive AMR in LPCMO/STO microbridge, the $\theta = 90^\circ$ shift in $R(\theta)$ (i.e., negative AMR) for $5\ \mu\text{m}$ -wide LPCMO/LAO bridge (see Figure 7.8 (a)) could be due to the strain-driven magnetic anisotropy which might produce anti-parallel coupling between the magnetizations of FMM domains resulting in a high resistance state at $\theta = 0^\circ$. Here we should remark that the changes of magnetic domain distributions in the LPCMO bridge should to be investigated carefully by magnetic force microscopy (MFM) and magneto-optic Kerr effect (MOKE) in order to obtain a clearer picture of the dynamics of AMR in these systems.

The change in the sign of AMR with an increasing the magnetic field at 85 K (see Figure 7.9) indicate that the relative orientation of the magnetization directions in FMM domains depends on the strength of the magnetic field. Magnetization in one of the FMM layers could rotate due to spin-torque effect (a force that changes the magnetization alignment with a magnetic field) [130] and hence causes a gradual sign change in the AMR for LPCMO/LAO wire with an increasing field.

7.3.5 Conclusions

We have shown that the spatial confinement produces interesting new features in the temperature dependence of AMR in LPCMO/LAO micro-bridges. Be-

sides the broad peak at T_{MIT} , two sharp peaks have been seen in the AMR(T) for this bridge. AMR crossover becomes more sensitive to the temperatures as the width of the bridge is reduced to match the size of the intrinsic FMM or COI domain.

Below we present main conclusions by comparing and contrasting the results between LPCMO/LAO and LPCMO/STO micro-bridges.

- The angular dependent magneto-resistance becomes very sensitive to the small changes in temperature when the width of the LPCMO bridge approaches the size of the intrinsic electronic domains in films deposited on LAO and STO substrates.
- The AMR sign difference observed between millimeter and micrometer wide LPCMO/LAO and LPCMO/STO films could originate from the strain-driven magnetic anisotropy.
- The spatial confinement could be used to enhance the anisotropic magneto-resistance in manganite-film-based devices.

CHAPTER 8

Summary and Conclusions

8.1 Overview

In this dissertation, we presented studies of the anisotropic magneto-resistance, fundamental spintronics property in phase separated $\text{La}_{0.7-x}\text{Pr}_x\text{Ca}_{0.3}\text{MnO}_3$ (LPCMO) ($0.00 \leq x \leq 0.40$) films. As compared to ferromagnetic metals, the AMR in manganites (ferromagnetic oxides) is governed by complex interactions between spin, charge, orbital and lattice degrees of freedom, which simultaneously affect material's transport properties. Therefore, LPCMO, well known phase separated manganite systems could be used to study the origins of AMR. We focused on four major problems relevant to AMR in phase separated LPCMO manganites. Those include: charge localization, cross-over phenomena, metastability and spatial-confinement effects, which have been studied systematically in order to gain deeper insight into the AMR in such highly correlated systems.

For instance, A-site doping driven enhancement of the activation energy, E_a and the exponential-like dependence of the AMR on E_a had been previously reported for NSSMO/LAO manganite systems. However, it has not been clear whether this dependence is universal, in films subjected to different signs and magnitudes of the epitaxial strain. This is important since activation energy might be used to control the magnitude of the AMR in manganites. Therefore, in order to address these problems we decided to perform a systematic study of AMR in LPCMO thin films with different thickness, doping and sign of epitaxial strain.

The underlying mechanism responsible for the sign change of the AMR at the cross over temperature in manganite films has not been fully understood. What causes the AMR sign crossover in these films? How does it depend on the lattice strain? In order to address these questions, we studied the magneto-transport and magnetic anisotropy of compressive LPCMO/LAO and tensile LPCMO/STO strained thin films.

Finally, we investigated the response of the AMR at the electronic domain level. A photo-lithography technique was used to pattern LPCMO micro-bridges, which allowed us to examine the magneto-transport properties on fine length scales. Details of each project are presented below in four separate sections.

8.2 Relationship between the charge localization and anisotropic magneto-resistance in $\text{La}_{1-x}\text{Pr}_x\text{Ca}_{0.3}\text{MnO}_3$ manganites

The correlation between the charge carrier localization and the anisotropic magneto-resistance (AMR) has been investigated for $\text{La}_{0.7-x}\text{Pr}_x\text{Ca}_{0.3}\text{MnO}_3$ ($0.00 \leq x \leq 0.35$) epitaxial thin films deposited on SrTiO_3 and LaAlO_3 substrates. An increase in the carrier localization, as evidenced by the rise of the small polaron activation energy E_a in the paramagnetic state, has been achieved either by increasing the dopant concentration x on the A-site or by decreasing the thickness (increasing the epitaxial lattice strain) in the film. The relationship between the AMR_{max} (the magnitude of AMR at the maximum near the metal-insulator temperature) and E_a exhibits a trend that is independent of the thickness of the film, the substrate and the doping concentration x . This implies that knowledge of the value of E_a measured in a film could be sufficient to accurately predict its AMR_{max} (the magnitude of the AMR at the maximum near T_{MI}) values in these films.

8.3 Crossover of anisotropic magneto-resistance in phase separated $\text{La}_{1-x}\text{Pr}_x\text{Ca}_{0.3}\text{MnO}_3$ thin films

Temperature dependence of the anisotropic magnetoresistance (AMR) has been studied in phase separated $\text{La}_{0.7-x}\text{Pr}_x\text{Ca}_{0.3}\text{MnO}_3$ (LPCMO) (of compositions $0.00 \leq x \leq 0.40$) epitaxial thin films deposited on LaAlO_3 (LAO) and SrTiO_3 (STO) substrates. Films deposited on LAO and STO substrates were subjected to compressive and tensile strain, respectively. Substituting smaller Pr^{+3} cations for larger La^{+3} was shown to enhance Jahn-Teller (JT) distortions, which consequently increase the AMR_{max} for LPCMO/STO strained films. In LPCMO/LAO films, the enhancement in the JT distortions leads to an increase of the AMR_{max} but only for dopings above $x=0.35$. Above this composition, the AMR_{max} decreases. Interestingly, at lower temperatures, well below the T_{MI} , the compressively strained films show a cross-over (i.e., transformation from $\sin^2(\theta)$ to $\cos^2(\theta)$ dependence in $R(\theta)$). Magnetization vs temperature dependence at 1.1 Tesla applied in-plane ($H \parallel (100)$) and out-of-plane ($H \perp (100)$) had been measured in LPCMO/LAO and LPCMO/STO films ($x=0.40$). Results clearly indicate that compressively strained films favor out-of-plane magnetization below cross over temperature while magnetization for tensile strained films favors in-plane over a wide range of temperature. This indicates that AMR sign difference for compressive and tensile strained LPCMO films at low temperature are due to strain-driven magnetic anisotropy.

8.4 Recovery of oscillatory magneto-resistance in $\text{La}_{0.3}\text{Pr}_{0.4}\text{Ca}_{0.3}\text{MnO}_3$ epitaxial thin films

In-plane AMR was studied for $\text{La}_{0.3}\text{Pr}_{0.4}\text{Ca}_{0.3}\text{MnO}_3$ films deposited on the (100) oriented NdGaO_3 , and (001) oriented SrTiO_3 and LaAlO_3 substrates. At temperatures where electronic phase separation is the strongest, a metastable irreversible state exists in the films whose resistivity ρ attains a large time dependent value. The ρ decreases sharply with an increasing angle θ between the magnetic field and the current, and does not display an expected oscillatory $\cos^2\theta$ dependence for all films. Regular $\cos^2\theta$ oscillations are recovered during repetitive sweeping of θ between 0° to 180° . Possible factors that might produce these unusual changes in the resistivity of samples include preferential expansion of the ferromagnetic metallic domains which strongly depends on the thermal cycling (cooling/warming) effects.

8.5 Anisotropic magneto-resistance in spatially-confined phase separated manganite structures

Many of the fundamental properties of electronically phase separated ferromagnetic oxides/manganites such as the anisotropic magneto-resistance (AMR) and colossal magneto-resistance (CMR), and their unusual dependence on tem-

perature and magnetic field, have been linked to the competing interactions between phase separated ferromagnetic metallic (FMM) and charge-ordered insulating (COI) domains. This results from the complex couplings between spin, charge, lattice, and/or orbital degrees of freedom. Interestingly, these interactions and the resulting properties are strongly influenced by the effects of spatial confinement, which modifies a subtle equilibrium between phase separated domains that are different shapes and sizes. Our investigation of the AMR in phase-separated ferromagnetic oxides showed a dramatic effect on the spatial confinement of this fundamental property. If the dimensions of a manganite thin film are reduced to match those of phase separated domains, tunneling effects are observed at temperatures near the metal-insulator transition. These tunneling effects enhance the magnitude of the AMR and replace the oscillatory AMR with rectangular-shaped tunneling AMR (TAMR). The results obtained for compressive and tensile strained LPCMO micro-bridges are as follows:

I-LPCMO/STO micro-bridges:

- (a)** Giant increases in AMR from 2.5 % to 50 % were detected during the in-plane rotation of the magnetic field.
- (b)** Angular dependence of the resistance $R(\theta)$ showed square wave-like behavior at temperatures where the size of the intrinsic FMM or COI domains were comparable to the size of the bridge.
- (c)** Magnitude of these sharp square wave-like $R(\theta)$ curves decreased, and the difference between the switching angles (where sharp changes in the resistance

occurs) increased with an increasing temperature.

II-LPCMO/LAO micro-bridges:

(a) Temperature dependence of the AMR showed a peak near the T_{MI} and another peak near the spatially confined temperature, with a magnitude much higher than the one near T_{MI} .

(b) In both millimeter-wide and micron-sized LPCMO/LAO films, the sign of the AMR changes at the crossover temperature. However, in micron-sized films, the smooth oscillatory $\cos^2\theta$ or $\sin^2\theta$ dependence of the resistance on θ had been observed in the mm-wide films is replaced by a sharp square wave-like $R(\theta)$.

8.6 Future Research

The results presented in this dissertation may lead to many interesting studies designed to manipulate or control the AMR effect in strongly correlated manganese thin films. Below, I outline these potential future projects and briefly discuss the reasons for studying them.

(a) Studies of AMR in spatially confined LPCMO systems could be further extended to include the role of the “geometry” of LPCMO micro-bridges on the AMR effect. For example, various patterns with different dimensions and shapes (i.e., zig-zag, anti-dots) (see Fig. 8.1 (a)) might be used to produce different percolation path in the bridges. This would be useful in understanding the role of the percolative transport on the AMR effect.

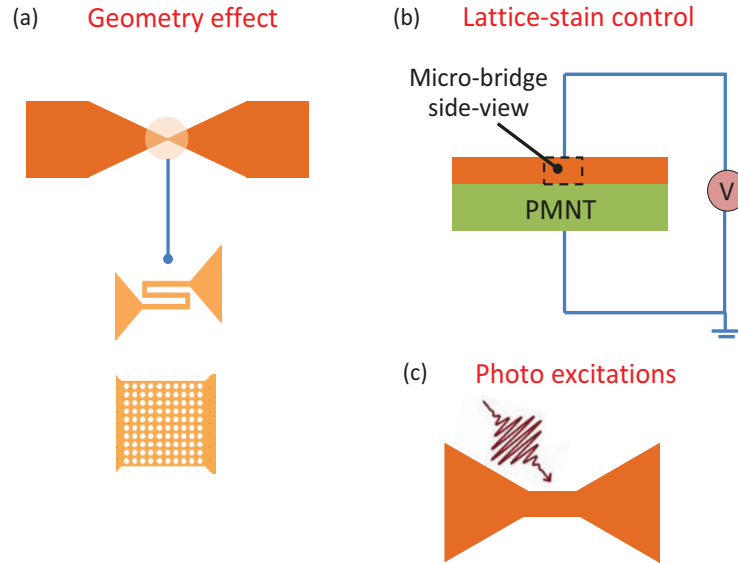


Figure 8.1: Studying AMR under various spatially confined structures and excitations: (a) geometry effects (i.e., zig-zag and anti-dots), (b) lattice-strain control under biasing PMNT-film and (c) photo-excitations of a micro-bridge.

(b) Introducing local lattice strain and controlling its value for LPCMO micro-bridges might be an effective way to modify the giant-resistive switching in the AMR observed in spatially confined systems. LPCMO micro-bridges could be patterned on piezocrystal substrates (i.e., Lead Magnesium Niobate-Lead Titanate (PMNT)) (see Fig. 8.1 (b)). The lattice parameters of this substrate change with the application of voltage across the substrate. This will affect the strain of film, which may modify the electronic phase separation in LPCMO bridge and hence AMR.

(c) Photo-excitation could be an interesting technique to modify the electronic and magnetic properties in LPCMO bridges (see Fig. 8.1 (c)). With this technique, one can study AMR when the percolation paths are disturbed by the interaction between the photon and magnetization in the bridge.

Bibliography

- [1] T. Jungwirth, J. Sinova, J. Masek, J. Kuera, and A. H. MacDonald, Rev. Mod. Phys. **78**, 809 (2006).
- [2] S. M. Thompson, J. Phys. D **41**, 0933001 (2008).
- [3] I. A. Campbell, and A. Fert, *In Ferromagnetic Materials* edited by E. P. Wohlfarth (North-Holland Pub. Co., Amsterdam), Vol. **3** (1982).
- [4] *Spintronics: from GMR to Quantum information*, Forschungszentrum Jülich GmbH, Institut für Festkörperforschung, Vol. **10** (2009).
- [5] T. R. McGuire, and I. Potter, IEEE Trans. Magn. **11**, 1018-1038 (1975).
- [6] M. Egilmez, M. M. Saber, A. I. Mansour, Rongchao Ma, K. H. Chow, and J. Jung, Appl. Phys. Lett. **93**, 182505 (2008).
- [7] M. K. Srivastava, A. Kaur, and H. K. Singh, J. Mater. Appl. Phys. Lett. **100**, 222408 (2012).
- [8] Y. Q. Zhang, H. Meng, X. W. Wang, J. J. Liu, J. Du, and Z. D. Zhang, Appl. Phys. Lett. **99**, 252502 (2011).

- [9] L. F. Wang, Z. Huang, X. L. Tan, P. F. Chen, B. W. Zhi, G. M. Li, and W. B. Wu, *Appl. Phys. Lett.* **97**, 242507 (2010).
- [10] Y. Murakami, H. Kasai, J. J. Kim, S. Mamishin, D. Shindo, S. Mori, and A. Tonomura, *Nature Nanotech.* **5**, 37-41 (2010).
- [11] H. -Y. Zhai, J. X. Ma, D. T. Gillaspie, X. G. Zhang, T. Z. Ward. E.W. Plummer, and J. Shen, *Phys. Rev. Lett.* **97**, 167201 (2006).
- [12] E. Dagotto, and Y. Tokura, *MRS Bulletin.* **33**, 1037-1045 (2008).
- [13] M. B. Salamon, and M. Jaime, *Rev. Mod. Phys.* **73**, 583 (2001).
- [14] Y. Tomioka and Y. Tokura, *Phys. Rev. B*, **70**, 014432 (2004).
- [15] A. N. Bloch, and G. C. Schatteman, *In Structure and Bonding in Crystals*, edited by M. O'Keeffe and A. Navrotsky. (Academic, New York), Vol. **1** (1981).
- [16] P. G. Radaelli, M. Mareizo, H. Y. Hwang, S. -W. Cheong, and B. Batlogg, *Phys. Rev. B* **54**, 8992 (1996).
- [17] J. Fontcuberta, B. Martínez, A. Seffar, S. Piñol, J. L. García-Muñoz, and X. Obradors, *Phys. Rev. B* **76**, 7 (1996).
- [18] Y. Tokura, *Fundamental Features of Colossal Magnetoresistive Manganise oxides*, Gordon & Breach, London (1999).
- [19] N. Tsuda, K. Nasu, A. Fujimori, and K. Siratori, *Electronic Conduction in Oxides*, Springer (2000).

- [20] H. A. Jahn, and E. Teller, Proc. R. Soc. London Ser. A **161**, 220 (1937).
- [21] G. H. Jonker, and J. H. Van Santen, Physica, **16**, 337 (1950).
- [22] J. H. Van Santen, and G. H. Jonker Physica, **16**, 599 (1950).
- [23] C. Zener, Phys. Rev., **82**, 403 (1951).
- [24] P. Anderson, and H. Hasegawa, Phys. Rev., **100**, 675 (1955).
- [25] B. Bechlars, D. M. D'Alessandro, D. M. Jenkins, A. T. Lavarone, S. D. Glover, C. P. Kubiak, and J. R. Long, Nat. Chem. **2**, 362-368 (2010).
- [26] N. Mathur, and P. Littlewood, Phys. Today **56**, 25 (2003).
- [27] M. Uehara, Nature **399**, 560 (1999).
- [28] J. Q. He, V. V. Volkov, T. Asaka, S. Chaudhuri, R. C. Budhani, and Y. Zhu, Phys. Rev. B **82**, 224404 (2010).
- [29] W. Wu, C. Israel, N. Hur, S. Park, S. -W Cheong, and A. DeLozanne, Nat. Mater. **5**, 881 (2006).
- [30] M. H. Phan, M. B. Morales, N. S. Bingham, H. Srikanth, C. L. Zhang, and S. W. Cheong, Phys. Rev. B **81**, 094413 (2010).
- [31] J. Jeon, H. S. Alagoz, J. Jung, and K. H. Chow, J. Appl. Phys. **115**, 233907 (2014).
- [32] L. Zhang, C. Israel, A. Biswas, R. L. Greene, and A. D. Lozanne, Science. **298**, 805 (2002).

- [33] A. Moreo, J. Electron Spectrosc. Relat. Phenom. **251**, 117-118 (2001).
- [34] J. Jeon, H. S. Alagoz, R. Boos, J. Jung, and K. H. Chow, Appl. Phys. Lett. **104**, 122405 (2014).
- [35] H. Guo, J. H. Noh, S. Dong, P. D. Rack, Z. Gai, X. Xu, E. Dagotto, J. Shen, and T. Z. Ward, Nano Lett. **13**, 3749 (2013).
- [36] D. Khomskii, and L. Khomskii, Phys. Rev. B **67**, 052406 (2003).
- [37] T. Z. Ward, Z. Gai, H. W. Guo, L. F. Yin, and J. Shen, Phys. Rev. B **83**, 125125 (2011).
- [38] W. Thomson, Proc. Roy. Soc. **8**, 546-550 (1857).
- [39] Denny D. Tang and Yuan-Jen Lee, *Magnetic Memory, Fundamentals and Technology*, Cambridge University Press (2010).
- [40] M. Ziese, and S. P. Sena, J. Phys.: Condens. Matter **10**, 2727 (1998).
- [41] I. A. Campbell, A. Fert, and O. Jaoul, J. Phys. C: Solid State Phys. **3**, S95 (1970).
- [42] N. F. Mott, Proc. R. Soc. Lond. A **153**, 699 (1936).
- [43] J. Smith, Physica **17**, 612 (1951).
- [44] A. P. Malozemoff, Phys. Rev. B **34**, 1853 (1986).
- [45] Von V. Döring, Ann. Phys. (Leipzig) **32**, 259 (1938).

- [46] J. D. Fuhr, M. Granada, L. B. Steren, and B. Alascio, *J. Phys: Condens. Matter B* **22**, 146001 (2010).
- [47] J. M. Ziman, *Electrons and Phonons*, Oxford University Press (1962).
- [48] Patrice E. A. Turchi, Antonios Gonis, Luciano Colombo, *Tight-Binding Approach to Computational Material Science*, Material Research Society (1998).
- [49] M. M. Saber, M. Egilmez, A. I. Mansour, I. Fan, K. H. Chow and J. Jung, *Phys. Rev. B* **82**, 172401 (2010).
- [50] M. Egilmez, I. Isaac, D. D. Lawrie, K. H. Chow and J. Jung, *J. Mater. Chem.*, **18**, 5796-5801 (2008).
- [51] P. J. Kelly and R. D. Arnell, *Vacuum*. **56**, 159-172 (2000).
- [52] S. Swan, *Physics in Technology* **19**, 67 (1988).
- [53] N. Yao, and L. Z. Wang, *Handbook of Microscopy for Nanotechnology*, Springer (2005).
- [54] R. C. Jeager, *Introduction to Microelectronics Fabrication Volume Volume V of Modular Series on Solid State Devices*, Prentice Hall, New Jersey (2002).
- [55] H. S. Alagoz, M. Khan, M. M. Saber, S. T. Mahmud, K. H. Chow, and J. Jung, *Appl. Phys. Lett.* **102**, 242406 (2013).
- [56] L. J. Swartzendruber, *Solid-State Electron* **7**, 413 (1964).

- [57] H. Yang, Y. Liu, and R. -W. Li, *Progress on Anisotropic Magnetoresistance Effect in Perovskite Manganites* **2**, 4 (2012).
- [58] M. Egilmez, R. Patterson, K. H. Chow, and J. Jung, *Appl. Phys. Lett.* **90**, 242506 (2007).
- [59] Mehmet Egilmez, *Magnetotransport and Magnetoresistive Anisotropy in Perovskite Manganites*, University of Alberta Thesis (2009).
- [60] C. Goldberg and R. E. Davis, *Phys. Rev.* **94**, 1121 (1954).
- [61] M. Egilmez, K. H. Chow, and J. Jung, *Mod. Phys. Lett. B* **25**, 697 (2011).
- [62] Th. G. S. M. Rijks, R. Coehoorn, and M. J. M. de Jong, *Phys. Rev. B* **51**, 283 (1995).
- [63] Y. Han, W. Wu, G. Jiang, and C. Zhu, *J. Appl. Phys.* **111**, 066104 (2012).
- [64] X. Hong, J. -B. Yau, J. D. Hoffman, C. H. Ahn, Y. Bason, and L. Klein, *Phys. Rev. B* **74**, 174406 (2006).
- [65] R. Gunnarsson, Z. G. Ivanov, C. Dubourdieu, and H. Roussel, *Phys. Rev. B* **69**, 054413 (2004).
- [66] R. -W. Li, H. Wang, X. Wang, X. Z. Yu, Y. Matsui, Z. -H. Cheng, B. -G. Shen, E. W. Plummer, and J. Zhang, *Proc. Natl. Acad. Sci. U.S.A.* **106**, 14224-14229 (2009).
- [67] D. Emin and T. Holstein, *Ann. Phys.* **53**, 439 (1969).

- [68] A. S. Alexandrov, A. M. Bratkovsky, and V.V. Kabanov, *Phys. Rev. Lett.* **96**, 117003 (2006).
- [69] X. J. Chen, S. Soltan, H. Zhang, and H.-U. Habermeier, *Phys. Rev. B* **65**, 174402 (2002).
- [70] X. J. Chen, H.-U. Habermeier, H. Zhang, G. Gu, M. Varela, J. Santamaria, and C. C. Almasan, *Phys. Rev. B* **72**, 104403 (2005).
- [71] L. Abad, V. Laukhin, S. Valencia, A. Gaup, W. Gudat, L. Balcells, and B. Martinez, *Adv. Funct. Mater.* **17**, 3918 (2007).
- [72] R. Prasad, H. K. Singh, M. P. Singh, W. Prellier, P. K. Siwach, and A. Kaur, *J. Appl. Phys.* **103**, 083906 (2008).
- [73] S. Seiro, E. Koller, Y. Fasano, and Ø. Fischer, *Appl. Phys. Lett.* **91**, 091913 (2007).
- [74] Y. M. Xiong, G. Y. Wang, X. G. Luo, C. H. Wang, X. H. Chen, X. Chen, and C. L. Chen, *J. Appl. Phys.* **97**, 083909 (2005).
- [75] X. Hong, A. Posadas, A. Lin, and C. H. Ahn, *Phys. Rev. B* **68**, 134415 (2003).
- [76] P. Dey, T. K. Nath, and A. Taraphder, *Appl. Phys. Lett.* **91**, 012511 (2007).
- [77] J. -B. Yau, X. Hong, A. Posadas, C. H. Ahn, W. Gao, E. Altman, Y. Bason, L. Klein, M. Sidorov, and Z. Krivokapic, *J. Appl. Phys.* **102**, 103901 (2007).

- [78] D. Pesquera, G. Herranz, A. Barla, E. Pellegrin, F. Bondino, E. Magnano, F. Sánchez, and J. Fontcuberta, *Nat. Commun.* **3**, 1189 (2012).
- [79] M. C. Smoak, P. A. Ryan, F. Tsui, T. K. Nath, R. A. Rao, D. Lavric, and C. B. Eom, *J. Appl. Phys.* **87**, 9 (2000).
- [80] R. Desfeux, S. Bailleul, A. Da. Costa, W. Prellier, and A. M. Haghiri-Gosnet, *Appl. Phys. Lett.* **78**, 23 (2001).
- [81] Q. Li, H. S. Wang, Y. F. Hu, and E. Wertz, *J. Appl. Phys.* **87**, 5573-5575 (2000).
- [82] T. Wu, S. B. Ogale, S. R. Shinde, A. Biswas, T. Polletto, R. L. Greene, T. Venkatesan, and A. J. Millis, *J. Appl. Phys.* **93**, 9 (2003).
- [83] N. L. Guo, J. Li, Y. F. Wei, Y. Zhang, L. M. Cui, L. Zhao, Y. R. Jin, H. Y. Tian, H. Deng, G. P. Zhao, and D. N. Zheng, *J. Appl. Phys.* **112**, 013907 (2012).
- [84] D. Gillaspie, J. X. Ma, H. -Y. Zhai, T. Z. Ward, H. M. Christen, E. W. Plummer, and J. Shen, *J. Appl. Phys.* **99**, 08S901 (2006).
- [85] J. O'Donnell, M. Onellion, M. S. Rzchowski, J. N. Eckstein, and I. Bozovic, *Phys. Rev. B* **55**, 5873 (1997).
- [86] M. Egilmez, Rongchao Ma, K. H. Chow, and J. Jung, *J. Appl. Phys.* **105**, 07D706 (2009).
- [87] Y. Suzuki, H. Y. Wang, S. -W. Cheong, and R. B. van Dover, *Appl. Phys. Lett.* **71**, 1 (1997).

- [88] L. M. Berndt, V. Balbarin, and Y. Suzuki, *Appl. Phys. Lett.* **77**, 18 (2000).
- [89] J. -P. Renard, and M. Velázquez, *Eur. Phys. J. B* **34**, 41-46 (2003).
- [90] J. Dvorak, Y. U. Idzerda, S. B. Ogale, S. Shinde, T. Wu, T. Venkatesan, R. Godfrey, and R. Ramesh, *J. Appl. Phys.* **97**, 10C102 (2005).
- [91] J. Li, S. G. Wang, Y. Zhang, L. M. Cui, Y. R. Jin, H. Deng, D. N. Zheng, A. Zimmers, H. Aubin, and P. L. Lang, *J. Appl. Phys.* **113**, 053901 (2013).
- [92] M. Egilmez, A. I. Mansour, M.M. Saber, K. H. Chow, and J. Jung, *Appl. Phys. Lett.* **92**, 022501 (2008).
- [93] F. Tsui, M. C. Smoak, T. K. Nath, and C. B. Eom, *Appl. Phys. Lett.* **76**, 17 (2000).
- [94] Y. Wakabayashi, D. Bizen, Y. Kubo, H. Nakao, Y. Murakami, M. Nakamura, Y. Ogimoto, K. MIYANO, and H. Sawa, *J. Phys. Soc. Jpn.* **77**, 014712 (2008).
- [95] J. Wolfman, W. Prellier, B. Mercey, and Ch. Simon, *J. Appl. Phys.* **87**, 9 (2000).
- [96] T. Z. Ward, J. D. Budai, Z. Gai, J. Z. Tischler, L. Yin, and J. Shen, *Nat. Phys.* **5**, 885 (2009).
- [97] I. C. Infante, V. Laukhin, F. Sánchez, J. Fontcuberta, O. Melnikov, O. Yu Gorbenko, and A. R. Kaul, *J. Appl. Phys.* **99**, 08C502 (2006).

- [98] I. N. Krivorotov, K. R. Nikolaev, A. Yu. Dobin, A. M. Goldman, and E. D. Dahlberg, *Phys. Rev. Lett.* **86**, 5779 (2001).
- [99] K. H. Ahn, T. Lookman, and A. R. Bishop, *Nature (London)* **428**, 401 (2004).
- [100] T. Wu, and J. F. Mitchell, *Phys. Rev. B* **74**, 214423 (2006).
- [101] G. Singh-Bhalla, A. Biswas, and A. F. Hebard, *Phys. Rev. B* **80**, 144410 (2009).
- [102] T. Z. Ward, X. G. Zhang, L. F. Yin, X. Q. Zhang, M. Liu, P. C. Snijders, S. Jesse, E. W. Plummer, Z. H. Cheng, E. Dagotto, and J. Shen, *Phys. Rev. Lett.* **102**, 087201 (2009).
- [103] Y. Xie, H. Yang, Y. Liu, Z. Yang, B. Chen, Z. Zuo, S. Katlakunta, Q. Zhan, and R. W. Li, *J. Appl. Phys.* **113**, 17C716 (2013).
- [104] Y. Liu, Z. Yang, H. Yang, Y. Xie, S. Katlakunta, B. Chen, Q. Zhan, and R. W. Li, *J. Appl. Phys.* **113**, 17C722 (2013).
- [105] L. Ghivelder, and F. Parisi, *Phys. Rev. B* **71**, 184425 (2005).
- [106] F. H. Zhang, Z. Huang, G. Y. Gao, P. F. Chen, L. F. Wang, X. L. Tan, and W. B. Wu, *Appl. Phys. Lett.* **96**, 062507 (2010).
- [107] T. Dhakal, J. Tosado, and A. Biswas, *Phys. Rev. B* **75**, 092404 (2007).
- [108] E. Dagotto, *Science* **309**, 257 (2005).

- [109] S. Wall, D. Brida, S. R. Clark, H. P. Ehrke, D. Jaksch, A. Ardavan, S. Bonora, H. Uemura, Y. Takahashi, T. Hasegawa, H. Okamoto, G. Cerullo, and A. Cavalleri, *Nature Phys.* **7**, 114 (2011).
- [110] N. Hur, S. Park, P. A. Sharma, J. S. Ahn, S. Guha, and S.-W. Cheong *Nature* **429**, 392 (2004).
- [111] J. M. Tranquada, H. Woo, T. G. Perring, H. Goka, G. D. Gu, G. Xu, M. Fujita, and K. Yamada, *Nature* **459**, 534 (2004).
- [112] S. Cox, J. Singleton, R. D. McDonald, A. Migliori, and P. B. Littlewood, *Nature Mater.* **7**, 25-30 (2008).
- [113] C. H. Ahn, A. Bhattacharya, M. Di Ventura, J. N. Eckstein, C. D. Frisbie, M. E. Gershenson, A. M. Goldman, I. H. Inoue, J. Mannhart, A. J. Millis, A. F. Morpurgo, D. Natelson, and J.-M. Triscone, *Rev. Mod. Phys.* **78**, 1185-1212 (2006).
- [114] W. J. Gallagher and S. S. P. Parkin, *IBM J. Res. Dev.* **50**, 5-23 (2006).
- [115] Th. G. S. M. Rijcks, R. Coehoorn, M. J. M. de Jonge, and W. J. M. de Jonge, *Phys. Rev. B* **51**, 283-291 (1995).
- [116] P. Padhan, and W. Prellier, *Phys. Rev. B* **76**, 024427 (2007).
- [117] T. Z. Ward, S. Liang, K. Fuchigami, L. F. Yin, E. Dagotto, E. W. Plummer, and J. Shen *Phys. Rev. Lett.* **100**, 247204 (2008).
- [118] B. Wang, L. You, P. Ren, X. Yin, Y. Peng, B. Xia, L. Wang, X. Yu, S. M.

- Poh, P. Yang, G. Yuan, L. Chen, A. Rusydi, and J. Wang, *Nat. Commun.* **4**, 2778 (2013).
- [119] G. S. -Bhalla, S. Selcuk, T. Dhakal, A. Biswas, and A. F. Hebard, *Phys. Rev. Lett.* **102**, 077205 (2009).
- [120] H. S. Alagoz, J. Jeon, S. T. Mahmud, M. M. Saber, B. Prasad, M. Egilmez, K. H. Chow, and J. Jung, *Appl. Phys. Lett.* **103**, 232402 (2013).
- [121] A. Sokolov, C. Zhang, E. Y. Tsymbal, J. Redepenning, and B. Doudin, *Nature Nanotech.* **2**, 171-175 (2007).
- [122] Y. W. Yin, J. D. Burton, Y. -M. Kim, A. Y. Borisevich, S. J. Pennycook, S. M. Yang, T. W. Noh, A. Gruverman, X. G. Li, E. Y. Tsymbal, and Q. Li, *Nature Mater.* **12**, 397-402 (2013).
- [123] W. -G. Wang, M. Li, S. Hegeman, and C. L. Chien, *Nature Mater.* **11**, 64-68 (2012).
- [124] J. G. Simmons, *J. Appl. Phys.* **34**, 238 (1963).
- [125] D. Niebieskikwiat, and M. B. Salamon, *Phys. Rev. B* **72**, 174422 (2005).
- [126] T. Nachtrab, S. Heim, M. Mößle, R. Kleiner, O. Waldmann, R. Koch, P. Müller, T. Kimura, and Y. Tokura *Phys. Rev. B* **65**, 012410 (2001).
- [127] G. S. -Bhalla, A. Biswas, and A. F. Hebard, *Phys. Rev. B* **80**, 144410 (2009).
- [128] M. Uehara, S. Mori, C. H. Chen and S. -W. Cheong, *Nature (London)* **399**, 560 (1999).

- [129] G. Cao, L. Balicas, Y. Xin, J. E. Crow, and C. S. Nelson, Phys. Rev. B **67**, 184405 (2003).
- [130] D. C. Ralph, and M. D. Stiles, J. Magn. Mater. **320**, 1190 (2008).
- [131] Y. Tokura, Rep. Prog. Phys. **69**, 797 (2006).
- [132] S. T. Mahmud, M. M. Saber, H. S. Alagoz, K. Biggart, R. Bouveyron, Mahmud Khan, J. Jung, and K. H. Chow, Appl. Phys. Lett. **100**, 2320406 (2012).
- [133] S. T. Mahmud, M. M. Saber, H. S. Alagoz, R. Bouveyron, J. Jung, and K. H. Chow, Appl. Phys. Lett. **100**, 072404 (2012).
- [134] R. K. Sahu, S. S. Manoharan, Q. Mohammad, M. L. Rao and A. K. Nigam, J. Appl. Phys. **91**, 7724 (2002).
- [135] C. Martin, A. Maignan, M. Hervieu, C. Autret, B. Raveau, D. I. Khomskii, Phys. Rev. B **63**, 174402 (2001).
- [136] Y. Ying, J. Fan, L. Pi, Z. Qu, W. Wang, B. Hong, S. Tan and Y. Zhang, Phys. Rev. B **74**, 144433 (2006).
- [137] R. D. Shannon, Acta Crystallogr., **32**, 751 (1976).
- [138] V. Y. Ivanov, A. A. Mukhin, A. S. Prokhorov, and A. M. Balbashov, Phys. Status Solidi B, **236**,445 (2003).
- [139] M. Egilmez, K. H. Chow, and J. Jung, Appl. Phys. Lett., **89**, 062511 (2006).

- [140] Y. Tomioka, Y. Okimoto, J. H. Jung, R. Kumai, and Y. Tokura, Phys. Rev. B, **68**,094417 (2003).
- [141] H. Sakai, K. Ito, T. Nishiyama, X. Yu, Y. Matsui, S. Miyasaka, and Y. Tokura, J. Phys. Soc. Jpn., **77**, 124712 (2008).
- [142] C. Martin, A. Maignan, M. Hervieu, B. Raveau, and J. Hejtmanek, Eur. Phys.J., **16**, 469 (2000).
- [143] I. Dhiman, A. Das, A. K. Nigam, and U. Gasser, J. Phys. Condens. Matter, **23**, 246006 (2011).
- [144] C. Krishnamoorthi, S. K. Barik, and R. Mahendiran, Solid State Commun., **151**,107-111 (2011).
- [145] C. L. Lu, X. Chen, S. Dong, K. F. Wang, H. L. Cai, J. -M. Liu, D. Li, and Z. D. Zhang, Phys. Rev. B, **79**, 245105 (2009).
- [146] Y. Tomioka, H. Hiraka, Y. Endoh, and Y. Tokura, Phys. Rev. B, **74**,104420 (2006).
- [147] A. Maignan, C. Martin, M. Hervieu, B. Raveau, and J. Hejtmanek, J. Appl. Phys., **89**, 4 (2001).
- [148] Y. Onose, J. P. He, Y. Kaneko, T. Arima, and T. Tokura, Appl. Phys. Lett., **86**, 242502 (2005).
- [149] J. S. Zhou and J. B. Goodenough, Phys. Rev. Lett., **96**, 247202 (2006).

- [150] J. S. Kim, D. C. Kim, G. C. McIntosh, S. W. Chu, Y. W. Park, B. J. Kim, Y. C. Kim, A. Maignan, and B. Raveau, Phys. Rev. B **66**, 224427 (2002).
- [151] R. K. Sahu, and S. S. Manoharan, Appl. Phys. Lett. **77**, 2382 (2000).
- [152] R. K. Sahu, Q. Mohammad, M. L. Rao, S. S. Manoharan and A. K. Nigam, Appl. Phys. Lett. **80**, 88 (2002).
- [153] R. K. Sahu, M. L. Rao, S. S. Manoharan, K. Dörr, and K. -H. Müller, Solid State Commun. **123**, 217-222 (2002).
- [154] R. Ganguly, C. Martin, A. Maignan, M. Hervieu, B. Raveau, Solid State Commun. **120**, 363-368 (2001).
- [155] H. S. Alagoz, I. Živković, S. T. Mahmud, M. M. Saber, G. Perrin, J. Shandro, M. Khan, Y. Zhang, M. Egilmez, J. Jung, and K. H. Chow, Phys. Stat. Sol. B. **250**, 2158-2162 (2013).
- [156] H. Y. Hwang, S.-W. Cheong, N. P. Ong, and B. Batlogg, Phys. Rev. Lett. **77**, 2041 (1996).
- [157] A. Gupta, G. Q. Gong, G. Xiao, P. R. Duncombe, P. Lecoeur, P. Trouiloud, Y. V. Wang, V. P. Dravid, and J. Z. Sun, Phys. Rev. B, **54**, 22 (1996).
- [158] Y. Sun, X. Xu, and Y. Zhang, Phys. Rev. B **63**, 054404 (2000).
- [159] Y. Sun, W. Tong, X. Xu, and Y. Zhang, Phys. Rev. B **78**, 5 (2001).

APPENDIX A

Competing doping effects in manganites

A.1 Introduction

The observation of colossal magneto resistance (CMR) in hole doped perovskite manganites ABO_3 have important scientific and technological ramifications. It has motivated many studies aimed at understanding and manipulating their magneto-transport properties.[6, 131, 132, 133] Strong correlations between spin, charge and orbital degrees of freedom play important roles in the manganites, and phase competition/separation is particularly prominent for manganites with the composition $RE_{1-x}AE_xMnO_3$ (where RE and AE are the rare earth and alkaline elements, respectively) with $x \sim 0.5$. In this regard, one interesting system is $RE_{0.55}Sr_{0.45}MnO_3$. It is found[14]that by changing the RE from Gd to Sm, which therefore increases the averaged ionic radius of the A-site cations $\langle r_A \rangle$ (electronic bandwidth) and simultaneously decreases the amount of quenched disorder, the system evolves from a spin glass insulator

(SGI) to a ferromagnetic metal (FMM).

In manganites, it is well-established that substitution of Mn ions with another dopant, i.e. “B-site doping”, can produce dramatic effects on the host’s transport and magnetic properties. Among the many possible B-site dopants, Ru has been found to be particularly efficient at enhancing the ferromagnetic interactions and the metallicity of a number of manganites, resulting in significant enhancements of the material’s Curie and metal-insulator temperatures T_C and T_{MIT} respectively (see e.g. Ref.[49, 134, 135, 136]). The interactions between Ru^{4+} ($t^4_{2g}e^0_g$), Ru^{5+} ($t^3_{2g}e^0_g$), Mn^{3+} ($t^3_{2g}e^1_g$) and Mn^{4+} ($t^3_{2g}e^0_g$) can include FMM, FMI (ferromagnetic insulator) and AFMI (anti-ferromagnetic insulator), which have different effects on the magnetic and transport properties of the material. Hence the relative importance of these interactions governs the sample’s metallicity and ferromagnetism at any particular Ru doping level. It is therefore worthwhile to systematically investigate and contrast the effects of Ru on manganites that are in the vicinity of the SGI and FMM border.[14] In particular, issues of interest include: *How does Ru enhance/suppress the T_C and T_{MIT} of the $\text{RE}_{0.55}\text{Sr}_{0.45}\text{MnO}_3$ systems as one tunes the RE composition across this border? Which properties are governed entirely by the B-site (Ru) doping, and which ones are affected only by the A-site (RE) substitutions? As the Ru doping level within a series increases, how will the competing interactions due to its substitution manifest themselves in the metallicity and ferromagnetism of the system, e.g. are there any obvious regimes where one type of interaction dominates?*

We have addressed these issues by synthesizing and analyzing the bulk

samples of $\text{RE}_{0.55}\text{Sr}_{0.45}\text{Mn}_{1-x}\text{Ru}_x\text{O}_3$ with $\text{RE} = \text{Gd}_y\text{Sm}_{1-y}$ ($0 \leq y \leq 1$) and Ru doping level x between 0 and 0.25. They have been chosen because of the properties of their undoped (no Ru) counterparts which depend on the average cation radius $\langle r_A \rangle$ (from 1.2121 Å for $y = 0$ to 1.1984 Å for $y = 1$). In particular, $\text{Gd}_{0.55}\text{Sr}_{0.45}\text{MnO}_3$ (i.e. $y = 1$) is a SGI; $(\text{Gd}_y\text{Sm}_{1-y})_{0.55}\text{Sr}_{0.45}\text{MnO}_3$ with $y = 0.95, 0.85, 0.75, 0.70,$ and 0.65 are near the border between SGI and FMM; and $(\text{Gd}_y\text{Sm}_{1-y})_{0.55}\text{Sr}_{0.45}\text{MnO}_3$ with $y = 0.50, 0.35$ and 0 are further into the FMM regime.

A.2 Experimental details

The bulk samples were prepared via a standard solid state reaction method. [49, 50] The temperature dependence of the resistivity measurements were carried out for rectangular bar-shaped samples in the absence of an applied field in the temperature range between 10 K and 300 K in 2 K steps using a standard four point probe technique. The crystal structure and phase purity of the samples were studied by using powder x-ray diffraction performed on a Rigaku x-ray diffractometer with a rotating anode and Cu $K\alpha$ radiation. In the resistivity measurements, the samples were first cooled down to ~ 10 K and then the resistance was measured during warming using a current of 1 μA . For samples where there is a clear metal-insulator transition, the T_{MIT} is defined as the temperature of the peak resistivity. Furthermore, T_{MIT} is assigned a value of zero if the sample is insulating.

The temperature dependence of the ac magnetic susceptibility was mea-

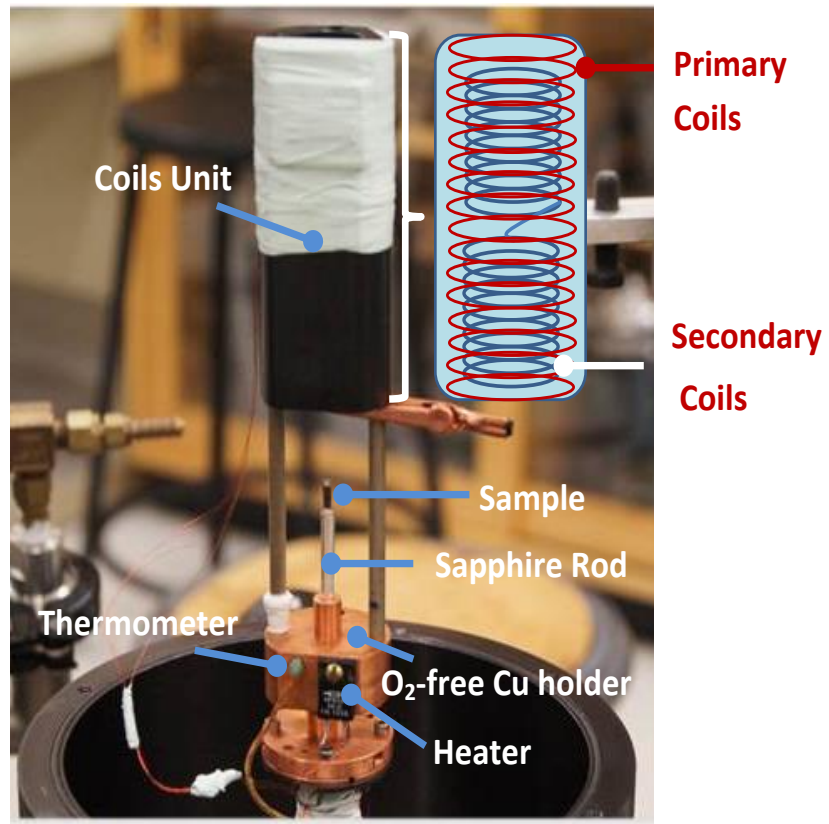


Figure A.1: Home built alternating current (AC) susceptibility system with a sample attached to a sapphire rod.

sured either in a home-built (see Figure A.1) or a CryoBIND susceptometer. The samples were zero-field cooled and the measurements taken upon warming in an ac field of ~ 5 Oe at 2 kHz. The values of the Curie temperature T_C were estimated using the gradient method, i.e., defined by the most negative slope of the in-phase component (χ') of the ac magnetic susceptibility. In samples with a spin-glass transition, the transition temperature T_{SG} is defined to be the temperature of the peak in χ' . As indicated in the previous section, it is useful to have a parameter that provides a quantitative measure of the amount of the quenched disorder due to the different elements occupying the A-site. For this purpose, we use the average ionic radius of the A-site cations $\langle r_A \rangle = (1-x)r_{RE}^{+3} + xr_{AE}^{+2}$ where x and r are the fractional occupancies and nine-coordinate ionic radii[137] of the RE and AE cations respectively. The relevant values of r are $r_{Gd}^{+3} = 1.107 \text{ \AA}$, $r_{Sm}^{+3} = 1.132 \text{ \AA}$, and $r_{Sr}^{+2} = 1.32 \text{ \AA}$.

A.3 Experimental results and discussion

In Figures A.2 (a) to (i), we show the temperature dependence of the resistivity $\rho(T)$ and the in-phase component of the ac susceptibility $\chi'(T)$ of 0%, 10% and 25% Ru doped RE = Gd_ySm_{1-y} ($y = 0.00, 0.75$ and 1.00) compositions. Consider first the Ru doped series for $y = 0.00$ in Figures A.2 (a), (d) and (g). SSMO ($y = 0.00$) with 0% Ru shows a metal to insulator transition at $T_{MIT} = 136$ K, and a transition from a ferromagnetic to a paramagnetic state at $T_C = 135$ K. The sharp peak in $\chi'(T)$ around 40 K has been interpreted as the onset

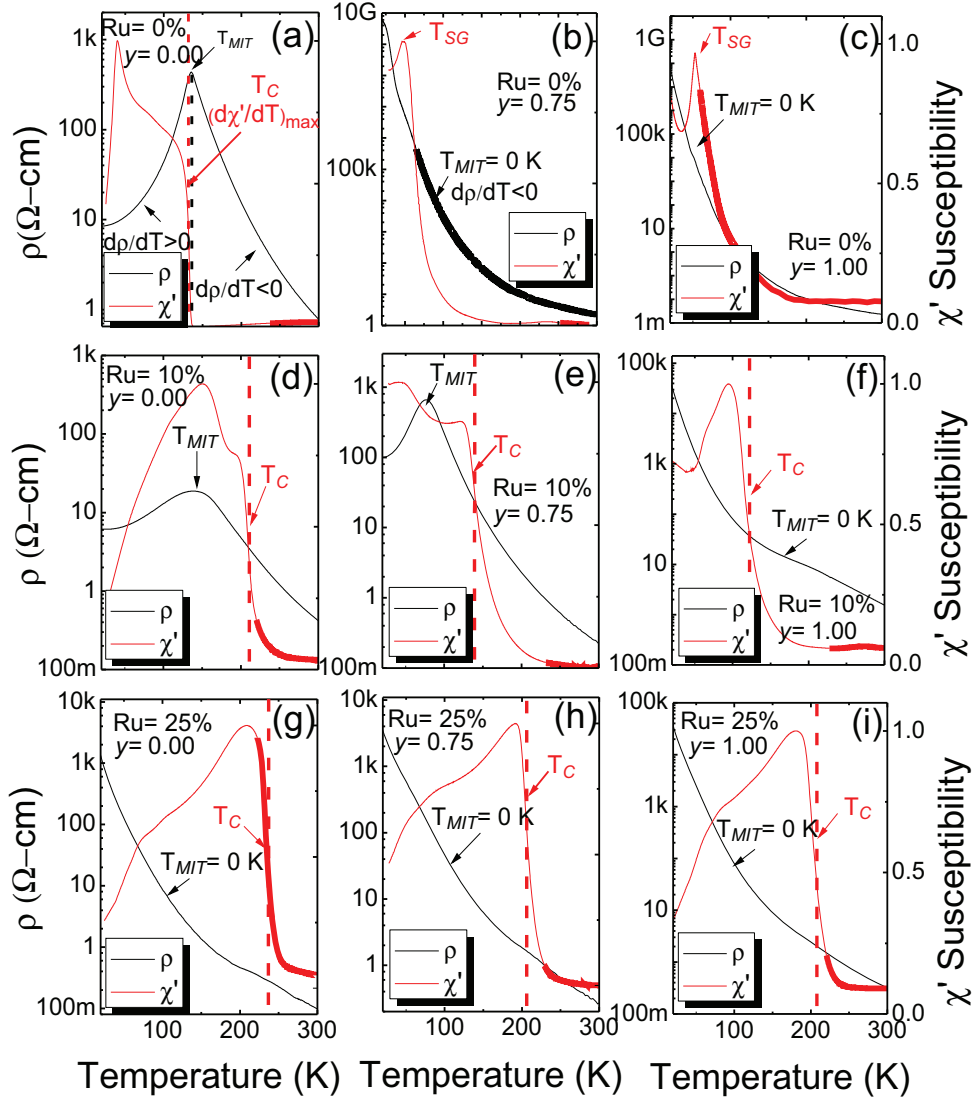


Figure A.2: Temperature dependence of resistivity (ρ) and normalized ac susceptibility (χ') of $x = 0\%$, 10% and 25% Ru doped $y = 0.00$, 0.75 and 1.00 compositions.

of the antiferromagnetic ordering and/or spin reorientation of the spontaneous magnetization.[138] However, this peak has significantly diminished by 10% Ru doping (see Fig. A.2 (d)), where the sample shows a T_C of 204 K above the T_{MIT} of 140 K. At 25% Ru, the sample becomes fully insulating ($T_{MIT} = 0$ K); however, it also shows a ferromagnetic transition at $T_C = 230$ K (see Fig. A.2 (g)).

In the case of Ru-free $y = 0.75$ composition (see Fig. A.2 (b)), the cusp at ~ 48 K in the ac susceptibility is indicative of the spin-glass transition temperature (T_{SG}). Furthermore, this sample is also insulating throughout the entire temperature range studied. This is in contrast to the behavior of the $y=0.75$, 10%, Ru sample (see Fig. A.2 (e)), which exhibits the FMM state with $T_C = 137$ K and $T_{MIT} = 77$ K. The presence of two phases with different chemical compositions could result in the double humps observed in the ac spectrum. For the 25% Ru doped $y = 0.75$ sample (see Fig. A.2 (h)) the $\chi'(T)$ shows that the ferromagnetism persists at temperatures up to $T_C = 204$ K, while the $\rho(T)$ shows that the sample is insulating at all temperatures.

Figures A.2 (c), (f) and (i) present $\rho(T)$ and $\chi'(T)$ dependences of Ru doped GSMO ($y = 1.00$) samples. The Ru-free sample shows a T_{SG} at 45 K with an insulating-like $\rho(T)$ behavior, indicating a spin glass insulating phase. (This is in a good agreement with previous ac magnetic measurements obtained for this composition[139, 140]) At Ru 10%, where the sample is at the verge of the percolation onset, the $\chi'(T)$ shows a downturn towards the lowest temperature which is discernible at around 50 K. This could be related to the T_{SG} transition. Moreover, the compound undergoes a ferromagnetic

transition with T_C at around 110 K. Finally, at 25% Ru doping level, the sample shows a ferromagnetic insulating phase with $T_{MIT} = 0$ K and $T_C = 210$ K.

Here, the clear downturn of $\chi'(T)$ as a function of decreasing temperature is observed in all 25% Ru doped compositions (see Fig. A.2 (g), (h) and (i)). A similar decrease of the magnetization and/or in-phase ac susceptibility has been observed in B-site doped single crystal of $\text{Gd}_{0.6}\text{Sr}_{0.4}\text{MnO}_3$ manganites.[141] These transitions may be caused by the formation of the spin glass phase. However, the nature of these transitions has not been studied in detail.

In the remainder of this chapter, we focus on the “primary”, i.e., the highest temperature, magnetic and transport transitions in each sample. The dependence of T_C , T_{SG} , and T_{MIT} on Ru content for the nine different values of y are shown in Fig. A.3. There are a number of notable features that can be inferred from these “phase diagrams”, as detailed below: (i) Consider the Ru-free samples, i.e. $x = 0$. The undoped RE = Sm ($y = 0$) sample has the largest average ionic radius $\langle r_A \rangle = 1.2121 \text{ \AA}$ among all the samples studied and T_{MIT} of 135 K. T_{MIT} drops as $\langle r_A \rangle$ decreases, i.e. increasing y , and in RE = $\text{Gd}_{0.50}\text{Sm}_{0.50}$ ($y = 0.50$) its value has been reduced to 65 K. For $y > 0.5$, the undoped systems enter the SGI regime (no T_{MIT}) with T_{SG} of ~ 50 K. These results are similar to those observed in single crystal $(\text{Gd}_y\text{Sm}_{1-y})_{0.55}\text{Sr}_{0.45}\text{MnO}_3$ manganites.[140] (ii) For the $y \leq 0.5$ series, the undoped samples are ferromagnetic materials. Doping these compounds with Ru up to 10% gradually increases T_{MIT} . However, T_{MIT} decreases as the Ru doping level is increased

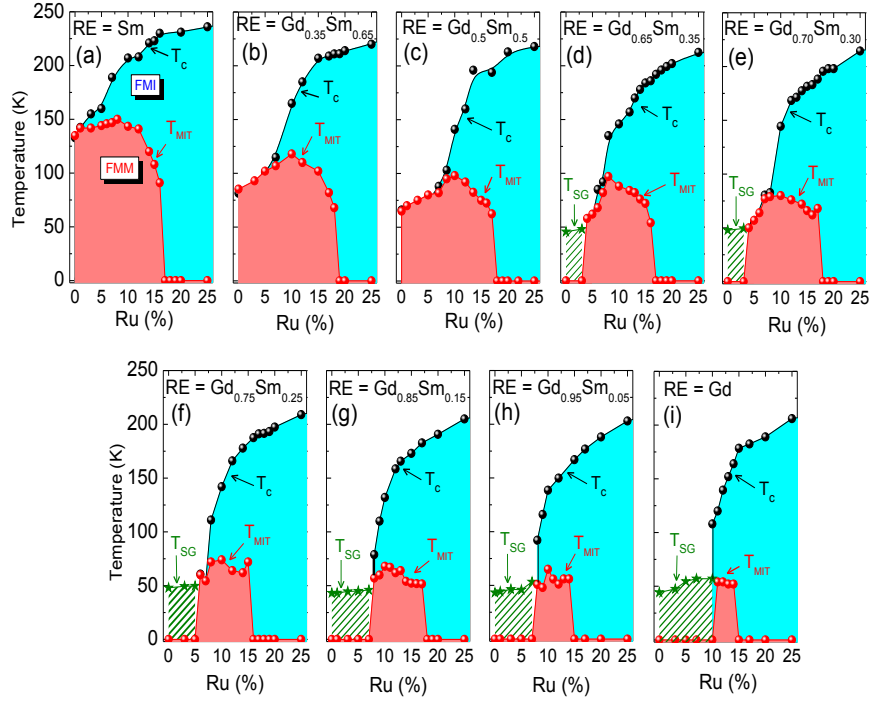


Figure A.3: Magnetic phase diagram of $\text{RE}_{0.55}\text{Sr}_{0.45}\text{Mn}_{1-x}\text{Ru}_x\text{O}_3$ with $\text{RE} = \text{Gd}_y\text{Sm}_{1-y}$ ($0 \leq y \leq 1$) and Ru doping level x between 0 and 25%. Red and blue areas are used as visual aids for identifying ferromagnetic metallic (FMM) and ferromagnetic insulating (FMI) regimes, respectively. Green dashed areas indicate the presence of spin glass insulators (SGI).

further; (iii) For the $y > 0.5$ series, the undoped samples are spin glass insulators. However, doping these samples with Ru always induces a transition from a SGI to a FMM phase at a certain doping level x_{po} . The value of x_{po} increases (from 3 to 10%) with an increasing y ; (iv) In every series ($0 \leq y \leq 1$), T_{MIT} drops sharply to zero above a value of $x_{pl} = 16-18\%$, i.e. there is a transition from FMM to FMI at this doping level. (v) Consider the samples within a series that are in a FMM state, i.e., they show both a T_C and a T_{MIT} . In general, T_C increases with the Ru doping level. At low Ru concentrations, the T_C and T_{MIT} values are similar. However, there is a significant divergence between T_C and T_{MIT} at larger Ru doping levels, as is also seen in some other manganite systems.[49, 136]

We now discuss possible explanations for the observations discussed above. Within each series, ferromagnetism eventually occurs as the Ru doping level increases even if the undoped samples are SGI. Furthermore, there is an overall increase in T_C with an increasing Ru concentration. These observations imply that increasing the Ru level produces enhancement of the ferromagnetic interactions in all members of the series. In fact, it is well accepted that substitution of Ru for Mn in manganites has the tendency to form ferromagnetic clusters around the Ru.[142, 143]

At low Ru concentrations, the proposed mechanisms for the formation of the FM clusters rely most effectively on the Ru^{5+} which lead to an increase of the DE interactions for Mn-Mn and Ru-Mn ions. The Ru^{5+} not only reduces the Mn^{4+} but also generates the equivalent number of Mn^{3+} due to the $2Mn^{4+} \rightarrow Ru^{5+} + Mn^{3+}$ substitution reaction.[136] In a number of manganites near

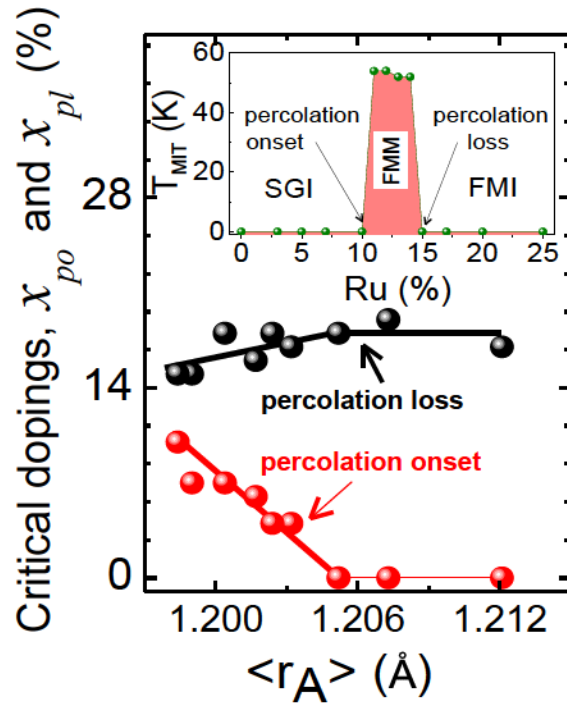


Figure A.4: Dependence of x_{po} and x_{pl} , the Ru doping level at which the percolation onset and loss occur, on $\langle r_A \rangle$. Inset: An example of the dependence of T_{MIT} on x in $\text{Gd}_{0.55}\text{Sr}_{0.45}\text{Mn}_{1-x}\text{Ru}_x\text{O}_3$ ($y = 1$) system ($\langle r_A \rangle = 1.1984$ Å), showing both the percolation onset and loss. SGI, FMM and FMI mark spin-glass insulator, ferromagnetic metal, and ferromagnetic insulator, respectively.

or at half-doping, an increase in the e_g electron density (i.e. Mn^{3+} content) via Ru doping has been suggested to increase the ferromagnetic interaction between Mn^{3+} and Mn^{4+} ions.[135, 144, 145] It is not clear if such a mechanism is valid for our systems since it is known that in $\text{Sm}_{0.55}\text{Sr}_{0.45}\text{MnO}_3$, T_C actually decreases with an increasing Mn^{3+} content, i.e. as the Sr content decreases in the vicinity of $\text{Sr} = 0.45$. [138, 146, 147] This would suggest that the effective change in the $\text{Mn}^{3+}/\text{Mn}^{4+}$ ratio caused by Ru substitution should suppress the ferromagnetic interaction and lead to a decrease in T_C , in contrast to our observations. However, caution should be exercised with regards to making a direct comparison between our Ru systems and that of Ru-undoped $\text{Sm}_{0.55}\text{Sr}_{0.45}\text{MnO}_3$ because changing the Sr content in the latter not only changes the e_g density but also other parameters such as $\langle r_A \rangle$ and the A-site quenched disorder (σ^2), which we are not directly doing as we substitute Ru for Mn within a particular series. Furthermore, in our systems, the existence of other magnetic interactions, such as those between $\text{Mn}^{3+}(t^3_{2g}e^1_g)$ and $\text{Ru}^{5+}(t^3_{2g}e^0_g)$ ions may also contribute to an increase in the DE interaction[23, 134] and hence the ferromagnetic transition temperature.

For $y \leq 0.5$, Ru increases metallicity (increases T_{MIT}) for x up to 10%. However, for $y > 0.5$, Ru does not generate any metallicity up to the critical concentration x_{po} at which the percolation takes place. This is summarized in Fig. A.4 which shows the dependence of that the “percolation onset” value x_{po} on the average ionic radius for all the series. This figure also highlights the fact that as $\langle r_A \rangle$ decreases (y increases), x_{po} must increase to induce the percolation onset. One possible explanation of these results is that at low Ru

doping levels and large y , the Ru-induced FMM clusters are too small in size and do not percolate. x_{po} shows a strong ionic size dependence, i.e., it increases with an increasing y (or decreasing $\langle r_A \rangle$). The Ru-free system ($x = 0$) becomes more disordered with an increasing y . In this case, ferromagnetism is gradually suppressed due to a weakening of DE and subsequent reduction of the hopping ability of itinerant e_g electrons.[145] Consequently, the FMM clusters become more progressively disconnected from each other and the amount of insulating phase increases. In order to recover the metallicity in the system, doping with more Ru is required to increase the size of FMM clusters and hence induce the percolation/metallicity.

While one consequence of increasing Ru is to increase the ferromagnetism and metallicity within a series, as discussed above, other interactions involving Ru are also important and their relative importance determine the rich behavior observed in Fig. A.3 and Fig. A.4. At high doping levels, Ru predominantly exists in the 4+ oxidation state which depletes the hole concentrations (i.e., Mn^{4+} content) and also a significant number of hopping sites.[134] The Ru^{4+} ions are in a low spin state (i.e., $t^4_{2g}e^0_g$), making it difficult to form the DE interaction between Mn^{3+} and Ru^{4+} ions.[136] However, the ferromagnetic superexchange (SE) interaction is possible between the Mn^{3+} and Ru^{4+} ions. DE and SE interactions favor different transport properties: DE enhances metallicity while SE favors insulating behavior, leading to the possible coexistence of FMM and FMI phases/clusters in the sample.[136] This may explain the gradual decrease in T_{MIT} , associated with an increase of T_C , for Ru doping levels $x > 10\%$, i.e., although FM interactions continue to be

important, the DE interaction becomes progressively “less dominant” than the SE interactions. Note, however, a previous study of the bilayered manganese oxide $\text{La}_{1.2}\text{Sr}_{1.8}(\text{Mn}_{1-y}\text{Ru}_y)_2\text{O}_7$ [148] has suggested that their observed increase of T_C with Ru doping is due to another mechanism: namely, the antiferromagnetic superexchange interaction between Ru and Mn moments. Hence, the nature of the exchange interactions between Ru and Mn is still a subject of controversy.

An intriguing feature is seen in Fig. A.3 for x above approximately 16-18% in each series: a transition from FMM to FMI phase occurs, represented by a sharp suppression of the metallicity by Ru doping, i.e. T_{MIT} drops to zero. At this doping level x_{pl} , the percolation is lost. Interestingly, x_{pl} is insensitive to the A-site substitution level y , and hence $\langle r_A \rangle$, as shown in Fig. A.4. Therefore, the relevant mechanism that is responsible for the suppression of metallicity at a fixed x_{pl} should be independent of $\langle r_A \rangle$. SE interactions have previously been attributed to the suppression of metallicity in Ru doped manganites above $x = 0.20$. [136] However, since x_{pl} is very insensitive to y and hence the ionic radius $\langle r_A \rangle$, and SE depends strongly on $\langle r_A \rangle$, [149] SE interactions alone cannot account for this sharp suppression in our samples. It is important to note that the change of the $\langle r_A \rangle$ of A-site does not affect the number of Mn^{3+} and Mn^{4+} ions because we keep the oxidation states for A site ions (RE^{+3} and AE^{+2}) same. This fact alone may explain the indirect effect of the $\langle r_A \rangle$ (A-site doping) on suppression of the metallicity.

A.4 Conclusions

We investigated the effects of Ru substitution of the Mn-site (B-site doping) on the metallicity and ferromagnetism in $\text{RE}_{0.55}\text{Sr}_{0.45}\text{MnO}_3$ by choosing $\text{RE}(\text{A-site}) = \text{Gd}_y\text{Sm}_{1-y}$ ($0 \leq y \leq 1$) such that the samples without Ru evolve from a spin glass insulator to a ferromagnetic metal. We have constructed “Temperature vs x ” phase diagrams of these $\text{Gd}_y\text{Sm}_{1-y}\text{Sr}_{0.45}\text{Mn}_{1-x}\text{Ru}_x\text{O}_3$ manganites for $0 \leq x \leq 0.25$. They allowed us to distinguish the effects of the A-site (RE) doping from those due entirely to the B-site (Ru) doping.

For $y \leq 0.5$, which are already ferromagnetic even in the absence of any Ru, increasing the Ru concentration enhances both the ferromagnetism and initially, the metallicity of each member of the series. On the other hand, for $y > 0.5$, the systems are SGI at low Ru doping level. However, they exhibit a transition to FMM at higher doping above a percolation threshold x_{po} whose value increases with an increasing y . Irrespective of the value of y , there is a transition from a FMM to a FMI phase at a critical doping x_{pl} of approximately 16-18%.

A.5 Unusual double-peak magneto-resistance in ruthenium doped ferromagnetic oxides

A.6 Introduction

As shown in previous section of this Appendix, manganites can exhibit sharp transformation from ferromagnetic metallic (FMM) phase to ferromagnetic insulating (FMI) phase at certain critical Ru concentration. In this section, we report detailed studies of this phase changes.

Ruthenium (Ru) doping on the Mn-site (i.e., B-site doping) of many perovskite manganites (ABO_3) has been the focus of intensive research for several decades, because of its ability to enhance the material's metallicity (metal-insulator transition; T_{MIT}) and ferromagnetism (Curie temperature; T_C).[\[49, 134, 135, 136\]](#) It has been suggested [\[150\]](#) that this property stems from the Ru-Mn magnetic exchange interactions as well as the ruthenium's itinerant $4d$ electrons and their extended $4d$ orbitals which produce an overlap and hybridization with oxygen's $2p$ orbitals in the $(Mn-Ru)O_6$ octahedra, resulting in a wider carrier bandwidth.[\[151\]](#)

However, several reports revealed that ruthenium B-site doping of manganites at a doping level above 15-30% results in a suppression of the system's metallicity.[\[136, 152\]](#) Unfortunately, the microscopic mechanism responsible

for the suppression of the metallicity is still under debate. Several different interpretations of this behavior have been proposed. It has been suggested that the suppression of the metallicity could be caused by the depletion of holes and hopping sites due to the ruthenium's valency which predominantly exist in the +4 oxidation state at high Ru-doping.[153] It has been also argued that the competition between the double exchange (DE) and the super-exchange (SE) interactions that exists between the Ru and Mn ions results in the insulating phase at high doping levels.[136] Another report suggests that in Sr-based manganites the suppression of metallicity is caused by the clustering of SrRuO₃ at these doping levels.[154]

Our recent studies of RE_{0.55}Sr_{0.45}Mn_{1-x}Ru_xO₃ with RE= Gd_ySm_{1-y} (0 ≤ y ≤ 1) and Ru doping level x between 0 and 0.25 manganites revealed the transition from a partly metallic ferromagnetic state to a fully insulating ferromagnetic state. This transition is very sharp and occurs at the percolation loss concentration, x_o around 0.16-0.18 for all compositions.[155] Ru doping increases T_C. Nonetheless, above x_o the rate at which T_C increases with x is reduced. There are several questions however, about the insulating state. What is the property of the ferromagnetic insulating state at a doping above x_o? How is this state formed? What is the microscopic mechanism responsible for the transition at x_o?

In order to answer these questions, the suppression of the metallicity at high levels of Ru doping level was investigated systematically in manganites of composition RE_{0.55}Sr_{0.45}Mn_{1-x}Ru_xO₃ (0 ≤ x ≤ 0.25) (RESRMO) with RE(A-site)= Sm, Eu and Gd. They have been chosen because of the magneto-

transport properties of their RESRMO ($x=0$) counterparts; $\text{Sm}_{0.55}\text{Sr}_{0.45}\text{MnO}_3$ is a pure ferromagnetic metal (FMM), $\text{Eu}_{0.55}\text{Sr}_{0.45}\text{MnO}_3$ is near the border between FMM and a spin-glass insulator (SGI), and $\text{Gd}_{0.55}\text{Sr}_{0.45}\text{MnO}_3$ is further at the pure SGI regime[14]. We measured and analyzed the dependence of the temperature derivative of the resistivity and the magneto-resistance over a high temperature range as a function of x . These data allowed us to conclude that the suppression of metallicity is associated with the formation of a phase with spatial spin disorder at high values of x .

A.7 Experimental details

Experiments were performed on polycrystalline samples prepared by using solid state reaction method.[50] Room temperature x-ray diffraction (XRD) measurement was collected using Rigaku diffractometer with a rotating anode. The Rietveld refinement ($Pbnm$ space group) indicated that all samples are single phase with an orthorhombic structure. Temperature dependence of resistivity have been measured between 10 K and 300 K in 2 K steps using standard four probe technique and 1 μA current pulses. The magneto-resistivity $MR = -[\rho(H) - \rho(0)] / \rho(0)$ [where the $\rho(H)$ and the $\rho(0)$ are the resistivities in an applied field and a zero field, respectively] was measured for each Ru doping as a function of temperature in a field up to 1.1 T.

A.8 Experimental results and discussion

Fig. A.5 (a) and (b) illustrate temperature dependence of resistivity ρ , for several Ru doping levels in ESMO manganite. Clear evidence of the enhancement of the metallicity with Ru doping is seen in Fig. A.5 (a). A small addition of Ru ($x= 0.005$), causes transformation of an insulating ESMO into one with a metal-insulating transition temperature. Moreover, Ru doping gradually suppresses the residual resistivity, and increases T_{MIT} . However, this trend is opposite at higher loping levels; an increase of the doping level enhances the residual resistance gradually an insulating-like $\rho(T)$ behaviour in these samples.

In order to explore the mechanism of the observed suppression of metallicity at higher Ru doping, we measured and analyzed the dependence of the temperature derivative of the resistivity ($d\ln(\rho)/dT^{-1}$) and the magneto-resistance (MR) for all ESMRO samples. Fig. A.6 display temperature dependence of ρ , $d\ln(\rho)/dT^{-1}$ and MR for low doping $x= 0.005$ and a high ($x= 0.25$) one. The $x= 0.005$ sample shows T_{MIT} at 64 K. (see Fig. A.6 (a)). In the insulating region, at higher temperature, the resistivity decreases smoothly with an increasing temperature. However, the resistivity for $x= 0.25$ sample shows very small hump around 200 K indicated by a dashed rectangle. Fig. A.6(b) shows the corresponding temperature dependence of $d\ln(\rho)/dT^{-1}$. The samples show a minimum in $d\ln(\rho)/dT^{-1}$ (T) at different temperatures; namely sample with $x= 0.005$ shows a dip at 55 K and that with $x= 0.25$ at 197 K. The first minimum at 55 K is near the metal-insulator transition, but the

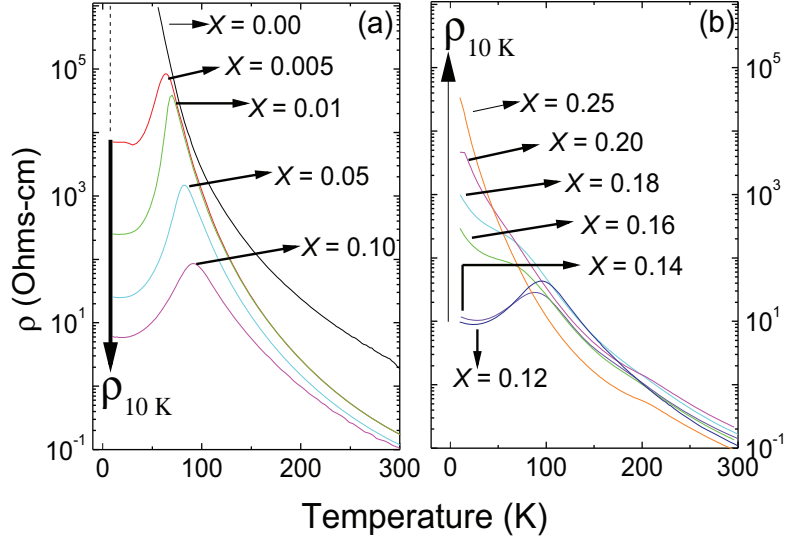


Figure A.5: (a) Temperature dependence of resistivity $\rho(T)$ in Ru doped $\text{Eu}_{0.55}\text{Sr}_{0.45}\text{Mn}_{1-x}\text{Ru}_x\text{O}_3$ (ESMRO) obtained during warming in zero magnetic field for doping ranges (a) ($0 \leq x \leq 0.10$) and (b) ($0.12 \leq x \leq 0.25$). The arrows indicate a decreasing trend of residual resistivity at (ρ_{10K}) with an increasing Ru doping level.

other minimum has different origin. The measurements of MR as a function of temperature in 1.1 T field (see Fig. A.6 (c)) for the $x= 0.005$ sample revealed a prominent MR at very low temperatures, which is usually observed in polycrystalline samples and originate from the tunnel magneto-resistance through grain boundaries.[156] However, the MR for $x= 0.25$ sample exhibits two peaks: one at low temperatures and the other secondary peak at 197 K. The secondary peak occurs at the same temperature as the minimum in $\text{dln}(\rho)/\text{d}T^{-1}$ vs T.

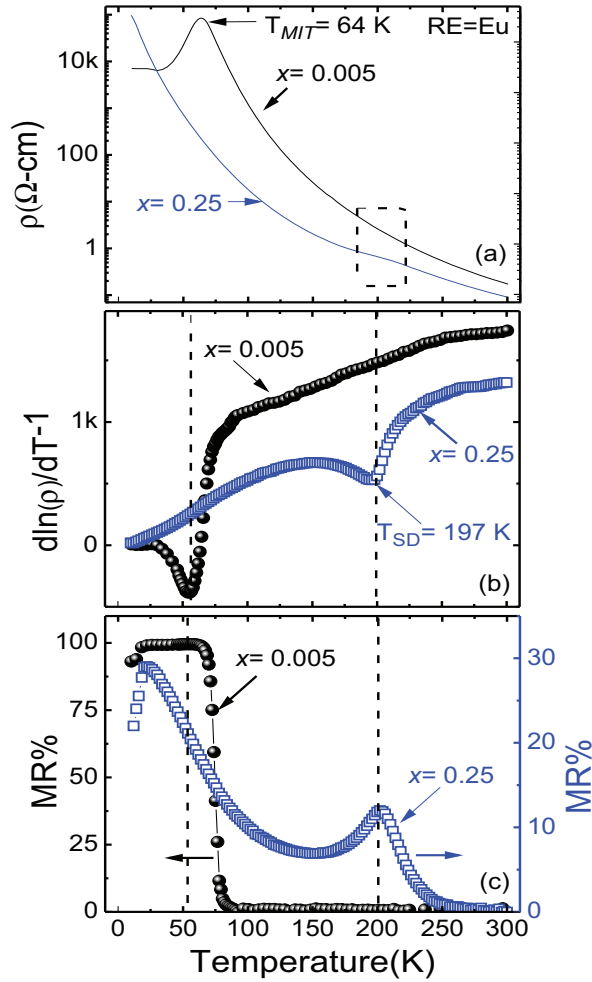


Figure A.6: (a) Typical temperature dependence of resistivity for low ($x = 0.005$) and high ($x = 0.25$) Ru doping levels in ESMO manganites. Dashed rectangle indicates the anomaly in the resistance. (b) Signature of a spin-disorder temperature (T_{SD}) extracted by plotting $d \ln(\rho)/dT^{-1}$ vs temperature. (c) Magneto-resistance as a function of temperature for $x = 0.005$ and 0.25 . The solid lines are guides to the eye.

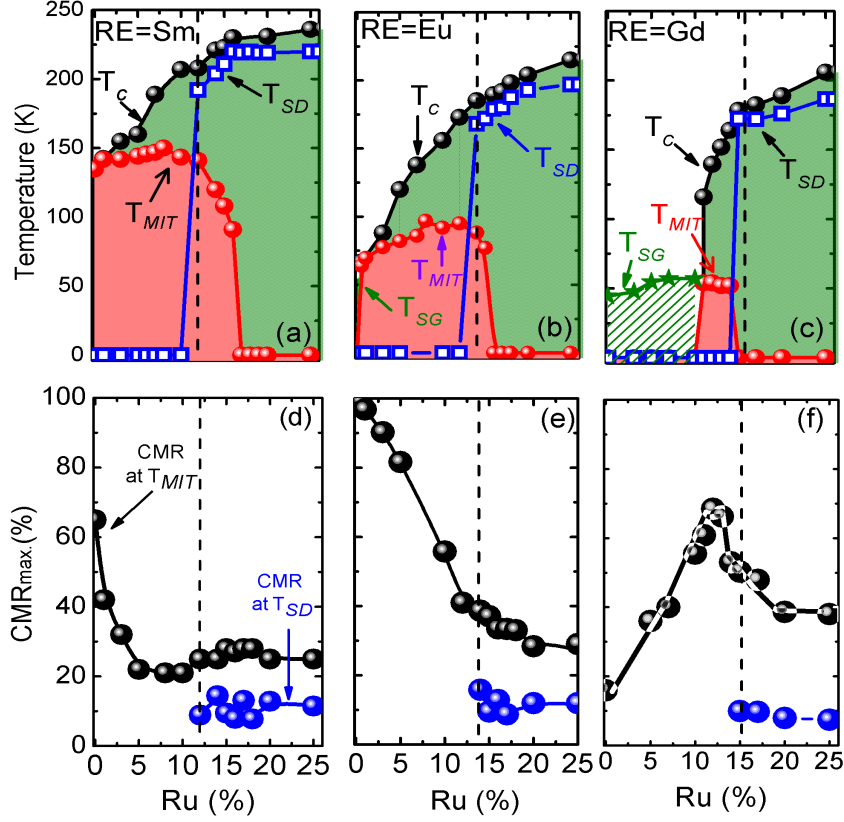


Figure A.7: Figures; (a) to (c) show magnetic phase diagrams of Ru doped $\text{RE}_{0.55}\text{Sr}_{0.45}\text{Mn}_{1-x}\text{Ru}_x\text{O}_3$ with RE = Sm, Eu and Gd plotted as a function of Ru doping level x between 0 and 25%. Red and light blue areas mark ferromagnetic metallic (FMM) and ferromagnetic insulating (FMI) regimes, respectively. Green dashed areas mark spin glass insulating (SGI) regimes. Figures; (d) to (f) shows corresponding magneto-resistance values obtained at low temperatures (black points) and high temperatures (blue points) plotted as a function of Ru doping.

What is the origin of the secondary peak in MR? First, it is important to point out that an increase of residual resistivity with an increasing Ru doping implies that magnetic and structural disorder increase with doping.[157] Presence of an increased magnetic disorder can also be seen in Figure A.7 (a)-(c) where the values of Curie temperature are reduced above a certain Ru doping level (indicated as a dashed line in the graphs). Notice that above this doping level, metallic behavior of the samples is reduced and sharp phase transformation from FMM to FMI takes place. It is quite interesting that a decrease in the metallicity or FMM to FMI phase transition takes place above critical doping levels at which samples show a secondary peak in their magneto-resistance (see the blue data points in Fig. A.7 (d)-(e)).

To understand secondary peak in the MR and its relation to sharp phase transitions at high Ru dopings, we propose a phenomenological model as schematically shown in Fig. A.8. We believe that presence of Ru produces spatially spin disordered regions in our samples. This mechanism is similar to that reported Cr doped $\text{La}_{0.67}\text{Ca}_{0.33}\text{MnO}_3$ manganites.[158, 159] These regions separate ferromagnetic metallic clusters and decreases percolation. When under an applied magnetic field, orientation of disordered spins are forced to order/align which favors electron delocalization and consequently results in a drop of the resistivity or magneto-resistance. Spin disorder may originate from Ru-Ru anti-ferromagnetic interactions which was observed earlier for highly Ru doped $\text{La}_{0.45}\text{Sr}_{0.55}\text{Mn}_{1-y}\text{Ru}_y\text{O}_3$ with $y = 0.4$ and 0.5 . Detailed studies such as electron spin resonance and neutron diffraction experiments may clarify possible anti-ferromagnetic interactions at higher Ru doped samples.

Near Curie Temperatures

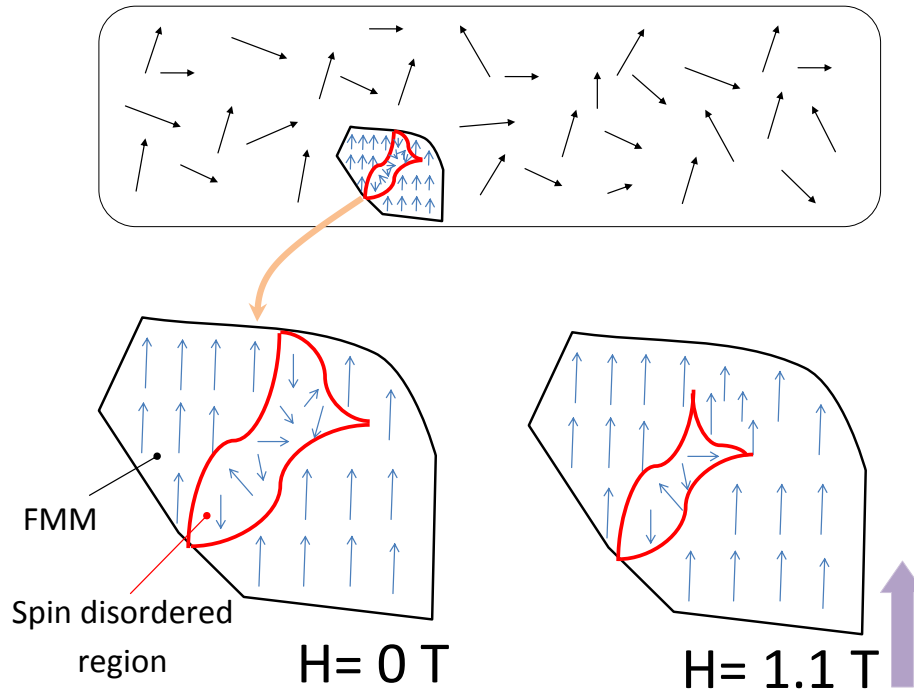


Figure A.8: Schematic of spin disorder effect near the Curie temperature for highly Ru doped manganite samples. Ru inclusion create spatially spin disordered regions (shown by red area) in the domain. Some randomly oriented spins in this domain tend to align with the application of magnetic field increasing the volume fraction of ferromagnetic metallic (FMM) region. This results in an increase of magnetoresistance in the sample.

A.9 Conclusions

We studied the magneto-transport properties of $\text{RE}_{0.55}\text{Sr}_{0.45}\text{Mn}_{1-x}\text{Ru}_x\text{O}_3$ ($0 \leq x \leq 0.25$) (RESRMO) with RE = Sm, Eu and Gd. At higher doping levels these samples show a secondary peak in the MR spectrum. Careful analysis shows that there exist strong correlations between the spatial spin disorder and the suppression of metallicity for Ru doped SSMRO, ESMRO and GSMRO manganite systems. These results suggest a universal mechanism leading to sharp transformation between the FMM and FMI phases in Ru doped ferromagnetic oxides systems.